2003

Nuclear spin lattice relaxation and conductivity studies of the non-Arrhenius conductivity behavior in lithium fast ion conducting sulfide glasses

Benjamin Michael Meyer
Iowa State University

Nuclear spin lattice relaxation and conductivity studies of the non-Arrhenius conductivity behavior in lithium fast ion conducting sulfide glasses.

by

Benjamin Michael Meyer

A dissertation submitted to the graduate faculty

in partial fulfillment of the requirements for the degree of

DOCTOR OF PHILOSOPHY

Major: Materials Science and Engineering

Program of Study Committee:
Steve W. Martin, Major Professor
Ferdinando Borsa
David Cann
Marshall Luban
Xiaoli Tan

Iowa State University

Ames, Iowa

2003

ProQuest Information and Learning Company
300 North Zeeb Road
P.O. Box 1346
Ann Arbor, MI 48106-1346

Graduate College
Iowa State University

This is to certify that the doctoral dissertation of

Benjamin Michael Meyer

has met the dissertation requirements of Iowa State University

Signature was redacted for privacy.

Major Professor

Signature was redacted for privacy.

For the Major Program

TABLE OF CONTENTS

LIST OF FIGURES

LIST OF TABLES

CHAPTER 1 GENERAL INTRODUCTION

1.1 Thesis Introduction

As time progresses, the world is using up more of the planet's natural resources. Without technological advances, the day will eventually arrive when these natural resources will no longer be sufficient to supply all of the energy needs. As a result, society is seeing a push for the development of alternative fuel sources such as wind power, solar power, fuel cells, and etc. These pursuits are even occurring in the state of Iowa with increasing social pressure to incorporate larger percentages of ethanol in gasoline. Consumers are increasingly demanding that energy sources to be more powerful, more durable, and, ultimately, more cost efficient. Fast Ionic Conducting (FIC) glasses are a material that offers great potential for the development of new batteries and/or fuel cells to help inspire the energy density of battery power supplies.[1]

This dissertation probes the mechanisms by which ions conduct in these glasses. A variety of different experimental techniques give a better understanding of the interesting materials science taking place within these systems.[2,3]

This dissertation discusses Nuclear Magnetic Resonance (NMR) techniques performed on FIC glasses over the past few years. These NMR results have been complimented with other measurement techniques, primarily impedance spectroscopy, to develop models that describe the mechanisms by which ionic conduction takes place and the dependence of the ion dynamics on the local structure of the glass. The aim of these measurements was to probe the cause of a

non-Arrhenius behavior of the conductivity which has been seen at high temperatures in the silver thio-borosilicate glasses.[4] One aspect that will be addressed is if this behavior is unique to silver containing fast ion conducting glasses. More specifically, this study will determine if a non-Arrhenius correlation time, τ, can be observed in the Nuclear Spin Lattice Relaxation (NSLR) measurements. If so, then can this behavior be modeled with a new single distribution of activation energies (DAE) to calculate the corresponding conductivity and relaxation rates as a function of temperature and frequency?

1.2 Thesis Organization

The dissertation is divided into four main areas. The first chapter covers an extensive literature review and relevant background material. The topics discussed in this chapter range from the fundamentals of glass preparation to descriptions about the experimental techniques used in this study.

The second chapter reports the effect that oxygen contamination has upon boron trisulfide (B_2S_3) glasses. B_2S_3 glasses are very sensitive to water and oxygen and thus it is difficult to prepare ultra-pure samples without oxygen (O) and water (H_2O) contamination. As a result, one concern is whether or not oxide contamination of the sample during a conductivity measurement can give rise to measured non-Arrhenius behavior. This study reveals that the two networks of B_2S_3 and B_2O_3 react to form homogeneous glasses which are comprised of BO_2S_1 and BO_1S_2 units. The study also shows that the B_2S_3 network remains quite robust with

the incorporation of some B_2O_3. This chapter has also been modified to include more recent IR data which was not included in the original journal publication.

Chapter 3 reports the properties and structure of LiI doped and undoped lithium sulfide thio-boro-germanate glasses. In this paper, qualitative evidence from IR and Raman spectroscopy measurements show that the lithium ions prefer to associate with germanium sites in these ternary glasses. As a result, a large number of germanium sites with two and three non-bridging sulfur atoms are observed. However, it is also found that that there are ~80% of boron atoms in tetrahedral coordination even though the sharing of the lithium sulfide prefers to associate with germanium sites. Similar to other halide salt doped systems, added LiI does not significantly alter the structure of these systems.

With a better knowledge about the structure of these glasses, Chapter 4 reports Nuclear Spin-Lattice Relaxation (NSLR) measurements in conjunction with conductivity measurements to explore non-Arrhenius behavior seen in many fast ion conducting systems. NSLR fits also give quantitative estimates of 70 to 80% of the lithium ions are associated with germanium sites. This is in agreement with the Raman and IR spectra of these glasses as reported in the previous chapter. A very important aspect of this paper is that it confirms that the non-Arrhenius behavior does indeed occur in these lithium glass systems. However, no detectable corresponding deviation from BPP theory is seen in the NSLR curves. From the fits to the NSLR measurements, two models are used to fit the corresponding conductivity data, and the results of these fits are compared. It is shown that the DAE model fits the Arrhenius portions of the conductivity well for these samples, but

fails to fit the non-Arrhenius regions. The ion trapping model (ITM) is then used in conjunction with a DAE to fit the non-Arrhenius regions of the dc conductivity. In addition to providing excellent fits, the ITM suggests some physical origins to the cause of the non-Arrhenius conductivity.

The last chapter is a general conclusion summarizing the progress that this study has made in the knowledge about these systems. In Addition, suggestions of future work to perform on these systems are made. As is the case in science, as more is learned about systems, more is uncovered and hence more questions to be answered.

Appendices after the last chapter of this thesis have been included which cover some additional information that will be relevant to future students performing similar work. This additional information includes several plots of different sets of data for archival purposes for future reference.

1.3 Background

1.3.1 Glass Structure and Formation

Even today, giving a definition of "glass" is not a trivial task. It is common for glass to be referred to as a supercooled liquid or as a solid. According to Varshneya[5] "glass" was derived from the Latin word "glæsum" which stood for a lustrous and transparent material. Since more than 99% of commercial glass is made from oxide-based glasses, it is not surprising that oxide glasses are usually

implied when the word "glass" is used. However, many non-oxide glasses exist; for example, the material under study in this proposal is a non-oxide based glass.

Zachariasen[5] defined glass as a material that forms an extended three-dimensional network that lacks periodicity. However, a stable glass is still comparable energy, though slightly higher, than its corresponding crystalline analogue network. From this, Zachariasen formulated four rules for oxide glass formation in an A_mO_n system.

1. "An oxygen atom is linked to no more than two atoms of A."
2. "The oxygen coordination around A is small, say three or four."
3. "The cation polyhedra share corners, not edges, not faces."
4. "At least three corners are shared."

While these rules have been highly successful, many glass-forming systems do not adhere to Zachariasen's rules. P_2O, As_2O_3, and V_2O_5 are some examples. Since the development of Zachariasen's rules, many other criterion have been developed. Sun's Single Bond Strength Criterion[6] proposes that glass formation is a direct consequence of a material's inability to rearrange bonds in the liquid state before undergoing solidification. Hence, stronger bonds would lead to better glass formers. Other examples are Dietzel's Field Strength Criterion[7] and Phillips's Topological Constraints Hypothesis.[8] This shows that even though glass has been used extensively for thousands of years, we still lack a complete understanding of glass formation and structure.

Compounds have been categorized according to their glass forming ability. Compounds such as SiO_2 and B_2O_3 are referred to as network formers because of

they are strong glass formers. Ionic oxides, such as Na_2O and K_2O, are not stable glass formers themselves and are referred to as network modifiers since they degrade the network structures of glass formers such as SiO_2. Some compounds, such as Al_2O_3, Fe_2O_3, and PbO, are intermediate between these and are known as mixed formers. While they are not glass forming themselves, they do expand the glass forming character of other oxides.

1.3.1.1 Glass Formation

All materials can be classified as glassy, crystalline, or some combination of both. Whether a material is classified as glassy or not depends upon its critical cooling rate, R_c, the slowest rate needed to produce a glass by cooling the liquid from above its melting point. The crystallization of a homogeneous liquid or glass does not instantaneously occur throughout the whole volume of the sample.[9] Crystallization occurs first by the formation of nuclei distributed throughout the sample. This process can be broken down into two stages. The first is called the nucleation stage. The second is called the crystal growth stage. Both of these stages are required in order for crystallization to occur. Varshneya describes the procedure for calculating whether a system will form a glass.[5]

First, the nucleation rate, I (Eq. (1-1)), is calculated as a function of temperature. Second, the crystal growth rate, u (Eq. (1-2)), is also calculated as a function of temperature. Last, the volume fraction of crystallization is determined by combining the results of the first two steps for the sample being held at a specified temperature and specified amount of time using the Johnson-Mehl-Avrami[10,11] Eq. (1-3).

1.3.1.2 Nucleation Rate

Nucleation processes occur at temperatures where the mobility is high enough for considerable atomic rearrangement. In homogeneous nucleation, at random points through out the sample tiny crystallites will briefly form. Above the melting point these phases are thermodynamically unstable and will quickly melt. At temperatures below the melting point, they are stable if they are above a critical size, r_c. Permanent stability of these phases is a result of a competition between a negative free energy volume change tending to stabilize the crystallite and the surface energy tending to destabilize the crystallite. Formation of a crystal is dependent upon the presence of stable nucleation sites that can further grow in size.

Two main barriers must be overcome in order for nucleation to occur. The first barrier, ΔE_D, is the kinetic barrier and describes the activation energy required for an atom to cross the interface of the liquid to the crystallite. The activation energy arises from the bonds that must be broken in order for the atoms realign into the more ordered crystal structure. The second thermodynamic barrier, W*, is the net free-energy change that occurs in the system when a nucleus has formed. Both of these terms contribute to the nucleus formation based on Boltzmann's probability. Eq (1-1) gives nucleation rate as a function of the barrier and temperature in number of nuclei formed per unit volume. Here, N_0 is Avogadro's number, R is the gas constant, T is the temperature, n is the number of atoms per unit volume, and υ is the atomic vibration frequency.

$$I(T) = n\upsilon \exp\left(-\frac{N_0 W^*}{RT}\right)\exp\left(-\frac{\Delta E_D}{RT}\right) \quad (1\text{-}1)$$

A typical temperature dependence of the nucleation rate, I, is shown in Figure 1.2. As temperature increase, the nucleation rate increases and goes through a maximum. At higher temperatures, the net free energy change to form solid reduces and no nucleation sites form. This causes a reduction in the nucleation rate to the point where no nucleation sites can form.

1.3.1.3 Crystal Growth Rate

The crystal growth rate is dependent upon the speed at which atoms can diffuse through from the liquid to the crystallite interface. Again, there is an activation energy, ΔE^*, for motion of the atom from the liquid region to the interface. ΔG_x is the free energy of crystallization. The equation below gives the crystal growth rate, where "a" is the distance between the closest liquid site and the first solid site.

$$u(T) = a\upsilon \exp\left(-\frac{\Delta E^*}{RT}\right)\exp\left(-\frac{\Delta G_x}{RT}\right) \quad (1\text{-}2)$$

Again, R is the gas constant, T is the temperature, and υ is the atomic vibration frequency. The temperature dependence of the crystal growth rate is also shown in Figure 1.2. At the melting temperature, Tm, and higher, the crystal growth rate is not positive. As at these temperatures, any crystallites melt to form the equilibrium liquid.

1.3.1.4 Time – Temperature – Transformation Curve

Using the Johnson-Mehl-Avrami equation[10,11], it is possible to describe quantitatively the kinetics of crystallization using the nucleation rate and the crystal growth rate equations. The Johnson-Mehl-Avrami is:

$$\frac{V_x(t, T)}{V_0} = 1 - \exp\left(\frac{\pi I(T) u(T)^3 t^4}{3}\right) \qquad (1\text{-}3)$$

V_x/V_0 is the fraction of sample volume which will be crystallized as a function of time, t. Generally, it is accepted that any crystal formation under the volume fraction of 10^{-6} is not detectable. Figure 1.3 shows an example of a typical T-T-T curve. The curve represents the time required to form a certain volume fraction of crystallite. Additional curves could be drawn for higher volume fractions of crystallization and would shift to the right at longer times. In order to form a glass, the cooling rate must be equal to or greater than the slope of the tangent line drawn in Figure 1.3. If the cooling rate is slower than the critical cooling rate, R_c, there will be sufficient time for the sample to nucleate and grow crystals.

1.3.2 Ionic Conduction in Glass

Since alkali cations are weakly bound to the glass forming network, ionic conduction can occur. With the increase in temperature the cations, vibrating in these shallow potential energy wells, are thermally excited and gain enough energy to overcome the potential energy barrier to jump into a new neighboring site. This hopping from site to site occurs in random directions, unless an electric field is applied to bias the hopping. This biasing is needed to perform a conductivity

measurement. Performing these measurements as a function of temperature and frequency allow values for conductivity and activation energy to be obtained.

Figure 1.6 shows an Arrhenius plot of the conductivities of an oxide and a sulfide glass ionic conductor. In the past, Arrhenius behavior for ionic conducting glasses was typically observed. In the last decade however, some FIC glasses have exhibited non-Arrhenius behavior at higher temperatures.

1.3.2.1 Nernst-Einstein Equation

One model that describes ionic conduction in solids is the Nernst-Einstein equation.[12] This equation treats ionic conduction as a process of self-diffusion of ions which is biased by the presence of an electric field,

$$\frac{\sigma}{D} = \frac{n(Ze)^2}{k_b T} \tag{1-4}$$

where σ is the conductivity, D is the diffusivity, Z is the charge per carrier, n is the concentration of charge carriers, k_b is Boltzmann's constant, T is temperature, and e is the fundamental unit of charge. By applying a random walk model to describe the thermally activated hopping process, a value for the diffusivity, D, can be derived.

$$D = \alpha\lambda^2\upsilon_0 \exp\left(\frac{\Delta S_D}{k_b}\right)\exp\left(\frac{\Delta E_{act}}{k_b T}\right) \tag{1-5}$$

where υ_0 is the frequency of jump attempts the ion makes, λ is the distance the ion covers in a single jump, α is a constant based upon the number of directions that the ion has available to jump to, ΔS_D is the entropy associated with hopping, and ΔE_D is

the energy barrier that must be overcome in order for the jump process to take place.

Combining these equations allows the thermally activated ionic conduction to be written as a function of temperature and activation energy.

$$\sigma_{d.c.} = \frac{n(Ze)^2}{k_b T} \alpha\lambda^2 \upsilon_0 \exp\left(\frac{\Delta S_D}{k_b}\right) \exp\left(-\frac{\Delta E_{act}}{k_b T}\right) \quad (1\text{-}6)$$

By grouping everything in front of the exponential containing the activation energy as a constant, σ_0, over T, it is possible to rewrite the above equation as the following.

$$\sigma_{d.c.} = \frac{\sigma_0}{T} \exp\left(-\frac{\Delta E_{act}}{k_b T}\right) \quad (1\text{-}7)$$

Conductivity can be greatly increased by decreasing the activation energy, ΔE_{act}, through compositional changes.

1.3.2.2 Anderson Stuart Model

Now that is has been determined that the activation energy plays an enormous role in controlling the conductivity, it is important to discuss the structural and compensational origins of the activation energy. The Anderson Stuart Model, like other short range order (SRO) models, compose the activation energy, ΔE_{act}, as two terms.[13] These two terms are the binding energy, ΔE_b, and the strain energy, ΔE_s. The binding energy, Eq. (1-8), is simply the energy required to overcome the coulombic attraction between the cation and the anion.

$$\Delta E_b = \frac{Z_+ Z_- e^2}{\gamma}\left(\frac{1}{r + r_0} - \frac{2}{\lambda}\right) \quad (1\text{-}8)$$

Z_+ and Z_- are the charge of the cation and anion, respectively, r_0 is the radius of the conducting ion, r is the radius of the non-bridging ion (e.g. oxygen or sulfur), λ is the jump distance, and γ is the covalency parameter describing polarizability of the ions. The strain energy is directly associated to the mobility of the cation which is the energy required to dilate interstices in the glass network to enable conduction from one site to another. The Anderson-Stuart equation for ΔE_s gives a relationship of the strain energy that must be overcome to enlarge a spherical cavity from radius r_d to r.

$$\Delta E_s = 8\pi G r_d (r - r_d)^2 \qquad (1\text{-}9)$$

In the above equation, G is the shear modulus. From this equation Anderson and Stuart derive a relationship of the activation enthalpy. As a result of the cubic relationship, it is worth noting that at a value where $r_d < r/3$, the activation decreases with decreasing doorway radius size, see Figure 1.4. It has been common for most researchers to ignore the smaller solutions for r_d.[14]

1.3.2.3 McElfresh and Howitt's Correction

This unphysical result, the strain energy decreasing with a decreasing doorway radius when $r_d < r/3$ of the Anderson Stuart Model led McElfresh and Howitt to develop a correction for it.[14] Instead of associating the strain energy with enlarging a spherical cavity upon which the ion can diffuse through, McElfresh and Howitt suggested that the activation energy can be better approximated by associating the strain energy to enlarging a cylinder. This implies that there is little or no strain in the immediate vacant region it leaves behind and also the immediate

vacant region upon which it is migrating into. The corrected equation for the strain energy, ΔE_s, is given below and the plot is shown in Figure 1.5.

$$\Delta E_s = \frac{1}{2}\pi G(r - r_d)^2 \qquad (1\text{-}10)$$

1.3.3 Nuclear Magnetic Resonance

This section is a built upon topics covered in detail by Slichter[15], Fukushima[16], and Abragam[22].

Nuclear Magnetic Resonance (NMR) is a technique in which a sample is placed inside a homogenous magnetic field and then irradiated with electromagnetic energy in the form of radio waves. Valuable information can be gained from the response of the nuclei with the magnetic interactions that take place. All nuclei which contain an odd number of protons and/or an odd number of neutrons have spin, I. This spin results in the nuclei carrying a magnetic moment, μ.

Each magnetic moment, μ, is proportional to the spin angular momentum, P.

$$\mu = \gamma P \qquad (1\text{-}11)$$

The gyromagnetic ratio, γ, is a constant unique to each type of nuclei. In the presence of a magnetic field each magnetic moment will experience a torque.

$$\text{torque} = \mu \times B_0 = \frac{dp}{dt} \qquad (1\text{-}12)$$

Differentiating and solving for the above equation reveals that the magnetic moment will precess about B_0 with an angular frequency, ω_0. Dividing ω_0 by 2π yields the Larmor frequency, υ_0. The Larmor frequency is the fundamental frequency at which the NMR experiment irradiates and detects responses from the sample.

At 0 K in a perfect system all of the magnetic moments would be aligned with the magnetic field. However, the number of moments aligned anti-parallel to the magnetic field increases with increasing temperature. For example, consider 1 gram of water which contains approximately 10^{23} protons placed inside a homogeneous magnetic field. At room temperature the number of protons that are aligned with the field and the number aligned anti-parallel to the field differ by approximately 10^5. Therefore, most of the protons in the system are randomly distributed and their effects cancel each other. However, the 10^5 protons provide enough of a magnetization for measurement. The population ratio is given by a Boltzmann factor which depends upon temperature and the strength of the magnetic field.

1.3.3.1 NMR Hamiltonians

The Hamiltonian of the system is a sum of all the different interactions of the system. In general, the Hamiltonian of interest to NMR could be given as:

$$H = H_{\text{nuclear spin coupling}} + H_{\text{nuclear quadrupole}} + H_{\text{Zeeman nuclear}} + H_0 + H_1 \qquad (1\text{-}13)$$

There are Hamiltonians of higher energy for a system, but these require other techniques such as optical spectroscopy or electron spin resonance (ESR) to probe. H_0 and H_1 are the applied static field and the field induced by the radio frequency pulse, respectively. The following sections cover the different interactions that are of great importance to NMR for the glasses studied in this thesis.

1.3.3.1.1 Nuclear Zeeman Splitting

Each NMR nucleus has a net magnetic moment. In the absence of a magnetic field, these moments are randomly oriented throughout the sample. The energy level associated to the magnetic moments are degenerate. However, in the presence of an external magnetic field, in a classical treatment, the components of the magnetic moments align parallel and anti-parallel to the magnetic field. The energy levels split and are no longer degenerate. These levels are quantized and have values of $m\hbar$ where $m = 2I + 1$ over the range $-I$ to $+I$. This is called Zeeman splitting. The Zeeman Hamiltonian is given by Eq. (1-14) where **H** is the applied magnetic field and m is the magnetic moment of the nucleus.

$$H_{Zeeman} = -\mu \cdot \mathbf{H} \tag{1-14}$$

For an applied static magnetic field H_0, the energy eigen values are given by Eq. (1-15)

$$Em = -\gamma h H_0 m \quad \text{where } m = I, I-1, \ldots, -I. \tag{1-15}$$

These energy levels are separated by

$$\Delta E = h\omega_0 \tag{1-16}$$

where h is Planck's constant, and ω_0 is the Larmor frequency. The Larmor frequency is the rate at which a nucleus precesses around a magnetic field and given by Eq.(1-17).

$$\omega_0 = \gamma H_0 \tag{1-17}$$

The common approach is to introduce the rotating coordinate frame at the Larmor frequency for the application of a radio frequency pulse.

$$H_1 = 2H_1 \cos(\omega t)i = H_R + H_L \tag{1-18}$$

H_1 is now the radio frequency applied field perpendicular to H_0. H_R and H_L are counter rotating components of the aligned magnetic moments and are given in .

$$H_R = H_1(\cos(\omega t)i + \sin(\omega t)j) \quad (1\text{-}19)$$

$$H_L = H_1(\cos(-\omega t)i + \sin(-\omega t)j) \quad (1\text{-}20)$$

When a radio frequency pulse is applied with a frequency of ω_0, resonance occurs and $H_1 = H_R$. By setting the rotating frame to rotate in the direction H_R, H_L can be ignored near resonance.[15] changing the frame of reference to the rotating frame makes H_{eff} appear as a static field.

The effective field generated by the radio pulse is given by:

$$H_{eff} = k'\left(H_0 + \frac{\omega}{\gamma}\right) + iH_1 \quad (1\text{-}21)$$

At ω_0, the H_{eff} then has only an x' component in the rotating frame. This allows for NMR experiments to manipulate the nuclear spin system through varying strength and time of H_1.

1.3.3.1.2 Dipolar Interaction

The Zeeman Hamiltonian by itself shows that the spin system absorbs energy at the Larmor frequency. However the NMR spectrum would be a delta function, which is not the case in practice. Other interactions in the system take place which broaden the line shape. Dipolar interactions among the different nuclei alter the magnitude of the split between energy levels of individual nuclei, see Figure 1.8. This interaction serves to broaden the line shape of the NMR spectra. The dipolar Hamiltonian is given in Eq. (1-22).

$$H_D = \sum_{j<k} \left[\frac{\mu_j \cdot \mu_k}{r_{jk}^3} + \frac{3(\mu_j \cdot r_{jk})(\mu j_k \cdot r_k)}{r_{jk}^3} \right] \quad (1\text{-}22)$$

In the above equation, μ_j and μ_k are the individual magnetic moments of interacting nuclei. r_{jk} is the distance between the two nuclei. The interactions are summed over all of the nuclear moments within the sample.

1.3.3.1.3 Quadrupole Interaction

The quadrupole interaction can also lead to significant spectral broadening for nuclei with spin greater than ½. Spins greater than ½ result in nuclei having non-spherical charge distribution which interacts with the electric field gradients (EFG). The quadrupole Hamiltonian is given by

$$H_Q = \sum_{m=-2}^{2} Q_2^m E_2^{-m} \quad (1\text{-}23)$$

wher E_2^{-m} is dependent upon certain electric field gradient terms.

$$E_2^0 = \frac{1}{2} V_{zz} \quad (1\text{-}24)$$

$$E_2^{\pm 1} = -\frac{1}{\sqrt{6}} \left(V_{xz} \pm V_{yz} \right) \quad (1\text{-}25)$$

$$E_2^{\pm 2} = -\frac{1}{2\sqrt{6}} \left(V_{xx} - V_{yy} \pm V_{xy} \right) \quad (1\text{-}26)$$

The electric field gradient terms are calculated by

$$V_{ij} = \frac{\partial^2 V}{\partial x_i \partial x_j} = \frac{\partial^2}{\partial x_i \partial x_j} \left(\int \frac{\rho(r')dr'}{|\vec{r} - \vec{r}'|} + \sum_i \frac{Z_i}{\vec{r} - \vec{r}_i'} \right) \quad (1\text{-}27)$$

Q_m describes the charge distribution in terms of the nuclear quadrupole moment summed over all protons in the nucleus.

$$Q = \left\langle I, m = I \left| \sum_p \left(3Z_p^2 - r_p^2\right) \right| I, m = I \right\rangle \tag{1-28}$$

$$Q_2^0 = \frac{eQ}{2I(2I-1)}\left(3I_z^2 - I^2\right) \tag{1-29}$$

$$Q_2^{\pm 1} = \frac{eQ}{2I(2I-1)}\frac{\sqrt{6}}{2}\left[I_z\left(I_x \pm iI_y\right) + \left(I_x \pm iI_y\right)I_z\right] \tag{1-30}$$

$$Q_2^{\pm 2} = \frac{eQ}{2I(2I-1)}\left(I \pm iI\right)^2 \tag{1-31}$$

Given that in the principle axis frame of reference $V_{ij} = V_{ij}\delta_{ij}$ and $|V_{zz}| \geq |V_{xx}| \geq |V_{yy}|$, then:

$$H_Q = \frac{h\upsilon_Q}{6}\left[3I_z^2 - I(I+1) + \frac{1}{2}\eta\left(I_+^2 + I_-^2\right)\right] \tag{1-32}$$

where η is the asymmetry parameter. η gives a measure of the deviation of the electric field gradient from axial symmetry at the nucleus center.

$$\eta = \frac{V_{xx} - V_{yy}}{V_{zz}}. \tag{1-33}$$

υ_Q gives a measure of the strength of the quadrupolar interaction.

$$\upsilon_Q = \frac{3eqeQ}{2I(2I-1)} \tag{1-34}$$

The effect of the quadrupolar interactions is shown in Figure 1.9.

1.3.4 NMR Spin-Lattice Relaxation and Conductivity Measurements

Before going into detail about the theories describing the spin-lattice relaxation and the mechanisms that allow ionic conduction to occur, attention needs to be given to the relaxation processes and its time dependence. Re-examining a simple case of a nuclei with spin I = 1/2, the spin that is aligned anti-parallel to the magnetic field will take time to give up its potential energy. This process takes time because the transfer of energy requires both an entity to accept it and a mechanism for the transfer to take place. Typically, this transfer of energy occurs through the acceptance of thermal energy causing translations, rotations, or vibrations in the lattice. Fukushima states that a spin in a high energy state can give up its energy via spontaneous or stimulated emission.[16] However, since the probability of spontaneous emission depends on the third power of the frequency, the probability for spontaneous is too low to be significant at radio frequencies. As a result, all transitions are therefore stimulated. This stimulation depends upon the presence of the nucleus experiencing fluctuating magnetic fields at its Larmor frequency. More importantly, since the nuclear spin-lattice relaxation process requires randomly varying magnetic fields usually generated through molecular motion, the relaxation rates give great information about the molecular motions.

As defined by the Bloch equation, two processes are involved in the excited nucleus attempt to return to equilibrium. These processes following an rf excitation are a spin-spin relaxation time, T_2, and a spin-lattice relaxation time, T_1. The T_2 process involves a dephasing of the spins that results from the interactions of the nuclei with slightly varying different internal fields. These internal fields also

determine the width of the NMR line, and therefore a relationship between T_2 and line width can be obtained.

1.3.4.1 Bloembergen-Purcell-Pound Theory

In many systems, researchers have used Bloembergen-Purcell-Pound theory[17] to obtain time-correlation functions (CF). Typically using the BPP theory, the NMR relaxation rate was plotted as $\log_{10}(R_l)$ versus 1/T. One of the main assumptions of the theory is that only a single activation energy is present. When applying this theory to ionic motion in FIC glasses, Martin[25] found that non-exponential decays in the correlation functions were required to account for the asymmetric maximum in the relaxation rate in which the frequency dependence at low temperatures deviates from the predicted ω^{-2} dependence by the BPP theory.

1.3.5 Kohlrausch-Williams-Watts Function

A common technique to accommodate the observed asymmetry was to use a stretched exponential function known as the Kohlrausch-Williams-Watts function.[18]

$$\Phi(t) = \exp\left[-(t/\tau^*)^{\beta}\right] \text{ where } 0 < \beta \leq 1 \qquad (1\text{-}35)$$

In this equation, For $\beta = 1$, the relaxation function is exponential with a single relaxation time. For $\beta < 1$, the relaxation function becomes faster at shorter time and slower at long time. The "stretching of the relaxation function is a simple, if not exactly accurate, method to account for the non-exponential relaxation. When using this function, it is not uncommon to find not only that the correlation time has a temperature dependence, but that the values for activation energy, correlation time,

and β extracted from the NMR data differ from the values for the conductivity measurements.

$$\tau^* = \tau_0 * \exp(\Delta E_a^* / k_b T) \tag{1-36}$$

Figure 1.10 shows a comparison of the correlation times obtained by NMR and conductivity measurements for the x = 0.45 and 0.55 of the $xLi_2s + GeS_2$ binary glass system studied by Kim. As you can see, if the NMR correclation times are extrapolated to similar temperatures as the conductivity, the NMR correlation times are an order of magnitude larger. A previous study of 0.56 Li_2S + 0.44 SiS_2 FIC glass was performed and yielded differing results between the conductivity and NMR correlation times.[19]

1.3.5.1 Application of the KWW Function to Conductivity Data

Applying the KWW function to the conductivity data including the stretched exponential allows for the extraction of an activation energy, correlation time, and a value for β. An expression for the real part of the conductivity with an applied stretched exponential can be derived using the electric modulus formalism as has been shown by Provenzano.[20]

$$\frac{1}{\varepsilon^*(\omega)} = \left(\frac{1}{\varepsilon_\infty}\right)\left[1 - \int_0^\infty dt \exp(-i\omega t)(-d\Phi(t)/dt\right] \tag{1-37}$$

Using Eq. (1-37), the real part of the conductivity can be written as

$$\sigma'(\omega, T) = \frac{\varepsilon_0\varepsilon_\infty \int_0^\infty \cos(\omega t)\Phi(t)dt}{\left[\int_0^\infty \sin(\omega t)\Phi(t)dt\right]^2 + \left[\int_0^\infty \cos(\omega t)\Phi(t)dt\right]^2} \tag{1-38}$$

An approximation was made for the conductivity using Dishon's formulas.[21]

$$Q_\beta(X) = \frac{1}{\pi}\int_0^\infty \exp(-u^\beta)\cos(Xu)du = \frac{1}{\pi}\sum_{n=1}^{\infty}(-1)^{n+1}\frac{\Gamma(1+n\beta)}{n!\,X^{1+n\beta}}\sin(\frac{n\pi\beta}{2}) \quad (1\text{-}39)$$

$$V_\beta(X) = \frac{1}{\pi}\int_0^\infty \exp(-u^\beta)\sin(Xu)du = \frac{1}{\pi}\sum_{n=1}^{\infty}(-1)^{n+1}\frac{\Gamma(1+n\beta)}{n!\,X^{1+n\beta}}\cos(\frac{n\pi\beta}{2}) \quad (1\text{-}40)$$

Now Equation (1-38) can be written in the following manner.

$$\sigma'(\omega, T) = \varepsilon_0\varepsilon_\infty \frac{\omega}{\pi X}\frac{Q_\beta(X)}{(Q_\beta(X))^2 + (V_\beta(x))^2} \quad (1\text{-}41)$$

1.3.5.2 Application of the KWW Function to NSLR Measurements

As in the previous section, the KWW stretched exponential function can also be applied to the ^{7}Li NSLR measurement data. According to Abragam[22], the average nuclear spin lattice relaxation rate is given by the following equation.

$$R_L = C(J(\omega_L) + 4J(2\omega_L)) \quad (1\text{-}42)$$

$J(\omega_L)$ is the spectral density of fluctuations seen by each spin at the Larmor frequency. These fluctuations are a result of hyperfine magnetic and electrical fields. C is a coupling constant which is proportional to the of the square of the amplitude of the fluctuations. Using the KWW stretched exponential function, the spectral density becomes

$$J(\omega_L) = \mathrm{Re}\int_{-\infty}^{\infty} dt\,\exp\left[-(t/t^*)^\beta\right]\exp(-i\omega_L t) \quad (1\text{-}43)$$

Again Dishon's formulas are used to write an approximation for the relaxation rate, R_L.

$$R_L = 2\pi C \frac{X}{\omega_L}\left[Q_\beta(X) + 4Q_\beta(2X)\right] \qquad (1\text{-}44)$$

Kim[25] notes that $Q_\beta(X)$ above has the same form as the equation used for the conductivity in the previous section. However, the values for β_{NMR}, τ_{0NMR}, and $\Delta E_{a\,NMR}^{*}$ differ from the values obtained from the conductivity data. Table 1-1 shows values obtained by Kim[25] from both the conductivity measurements and NMR measurements using $\tau_{0NMR} = 3 \times 10^{-14}$ s.

1.3.6 Distribution of Activation Energies

As it was shown in a previous section, the correlation times obtained by the NMR data and the conductivity data differ by an order of magnitude. Other approaches, such as Ngai's coupling model, have been used to account for this discrepancy.[23] MacDonald also reports using a cutoff model.[24] Yet neither of these two approaches appears to start from a physical interpretation of the dynamics. By incorporating a DAE, it is possible to account for this discrepancy by deriving the interactions from physical principles.[25] It has been shown that the relaxation time in NMR and the conductivity can both be derived from DAE.[26] The assumption of this approach is that the ions are present in the glass have differing energy barriers. This assumption is valid considering the known structural disorder of glass. This local disorder gives rise to barriers seen by hopping ions that vary in height and depth.

This DAE is given by $Z_{NMR}(\Delta E_a)$, shown in Figure 1.11. As a result of $Z_{NMR}(\Delta E_a)$, the ions hop with different rates (r_a).

$$r_a = r_{0a} \exp(-\Delta E_a / k_b T) \quad (1\text{-}45)$$

ΔE_a is the activation energy that an individual ion experiences when attempting to hop. The pre-exponential factor r_{0a} is the attempt rate. An important key here is that the ion hopping attempt rates have been limited to numbers that are physically realistic. Kim[25] used the following relationship to obtain reasonable values for r_{0a}.

$$r_{0a} = (\Delta E_a / 2m)^{0.5} / d \quad (1\text{-}46)$$

For lithium containing FIC glasses, the mass, m, represents the mass of the lithium ion. For all the energy barriers, ΔE_a, a value of 4×10^{-10} m was used for the average jump distance, d. By assuming that each Li ion was neighbored by 6 empty wells, the pre-exponential factor for the correlation time could be calculated.

$$\tau_{0a} = 1 / 6r_{0a} \quad (1\text{-}47)$$

The average relaxation time, R_1, over the DAE could then be calculated provided that the dipolar spin-spin (T_2) relaxation is significantly faster than the individual R_i values for each ion.

$$R_1(\omega_L, T) = C\int_0^{\infty}\left[\frac{\tau_a}{1 + \omega_L^2\tau_a^2} + 4\frac{\tau_a}{1 + 4\omega_L^2\tau_a^2}\right]Z_{NMR}\,d\Delta E_a \quad (1\text{-}48)$$

As seen in Equation (1-48) the average relaxation rate for the system, R_1, has a dependence upon temperature (T) and the Larmor frequency (ω_L). Z_{NMR} is calculated by assuming a Gaussian DAE centered at an average ΔE_m with the standard deviation being equal to ΔE_b. In order to obtain a better fit to the a.c. conductivity at low temperatures and high frequencies, a Lorentzian component

(20%) was added to the Gaussian (80%) DAE. Table 1-2 shows values used for the parameters of the distribution of activation energies model.

1.3.6.1 Calculation of the DC Conductivity from the DAE

Once a DAE has been determined from the NSLR $1/T_1$ data, it is then possible to calculate the dc conductivity based on the percolation theory.[27] The basis of this theory is that dc conductivity occurs via ion motion over a continuous path of the lowest barriers in the glass structure. For this to occur, a percolation fraction of P ~ 0.30 of the low barriers for dc conductivity must be present in a cubic lattice, where there are six directions for the ion to hop, in order for the ion to successfully hop through the network along a connected pathway. Applying this to glasses the equation for the percolation fraction can be written as the following.

$$P = \int_0^{E_p} Z_{NMR}\, d\Delta E_a \qquad (1\text{-}49)$$

ΔE_p is defined as the percolation limit; it is assumed that the ions hopping over the larger barriers in the glass are infrequent and do not contribute to the conductivity. Eq. (1-50) was used to calculate the conductivity as a function of temperature.

$$\sigma_0 = NPe^{\,2}d^2 \,/\, 6k_bT\tau_{av} \qquad (1\text{-}50)$$

In the above equation, N is the concentration of mobile ions, and τ_{av} is the average time between hops using the random walk model[28] with the percolation fraction.

$$\tau_{av} = (1 / P) \int_0^{\Delta E_p} \tau_a(\Delta E_a / T) Z_{NMR}(\Delta E_a) d\Delta E_a \qquad (1\text{-}51)$$

1.4 Non-Arrhenius Behavior in Conductivity

It has been established that the DAE model is able to predict the Arrhenius conductivity of glassy samples.[25] In effort to create more conductive glasses, much work has been invested in compositionally improving the conductivity of sulfide glass systems.[29,30,31] With the optimized $Ag_2S + B_2S_3 + SiS_2$ glass system, for example, it was found that at higher temperatures, the conductivity is as much as two orders of magnitude less than the extrapolated conductivity from lower temperatures.[32] As more AgI was added, the deviation from Arrhenius behavior became more dramatic. That is, the deviation from straight line Arrhenius behavior starts at lower temperatures and becomes greater. Regardless of the amount of AgI added, it was found that all of the samples seem to maximize at the same level of conductivity at the higher temperatures. Suggestions of ion-ion interactions causing non-Arrhenius behavior has been fairly common.[33,34,35]

1.4.1 Ngai Coupling Model

Ngai has used a coupling[33] scheme where he has introduced two frequency time regimes. At short times where $t<t_c$, the correlation function is a result of independent hopping relaxation times of individual ions shown in the equation below.

$$C(t) = \exp[-(t / \tau_0(T))] \qquad (1\text{-}52)$$

Where as, τ_0 is determined by

$$\tau_0(T) = \tau_\infty \exp(E_a / kT) \qquad (1\text{-}53)$$

At longer times where $t>t_c$, interactions between ions become significant and the correlation function is then modified to a Kohlrausch's stretched exponential form where n is in the range of 0 to 1:

$$C(t) = \exp[-(t / \tau_\sigma)^{1-n}] \qquad (1\text{-}54)$$

Ngai has stated that measurements in a FIC and also in a molten salt have shown that t_c has a value of approximately 1 to 2 ps.[33] Using the electric modulus formulation[36,37] the correlation function can be formally written as

$$C(t) = \int_0^\infty g(\tau) \exp[-(t / \tau_\sigma)]d\tau \qquad (1\text{-}55)$$

Hence the d.c. conductivity can then be calculated using an average conductivity relaxation time $<\tau_\sigma>$. The equation for calculating the d.c. conductivity is given below.

$$\sigma_{dc} = e_0\varepsilon_\infty / < \tau_\sigma > = e_0\varepsilon_\infty / \int_0^\infty \tau g(\tau)d\tau \qquad (1\text{-}56)$$

Even though this model can fit the non-Arrhenius behavior, it still doesn't address the physical origins causing this behavior.

1.4.2 Ion – Ion Scattering Model

The work by Schrooten and Martin[34,35] used the Drude theory as an approach to ion-ion scattering. The conductivity can be calculated by Equation (1-57) where τ is the time between collisions. (Note the definition of τ in this section is different from the correlation time in the previous section.)

$$\sigma_{dc} \approx \frac{ne^2\tau}{m} \tag{1-57}$$

The time between collisions, τ, is calculated as the mean free path, l_{mpf}, divided by the mean square velocity, v. The mean free path has a value of the average ion-ion separation distance of just a few angstroms determined by neutron scattering data.

$$\tau \approx \frac{l_{mfp}}{v} \tag{1-58}$$

The mean velocity <v> is taken to be the average thermal velocity in the system.

$$\Delta E \approx 3 / 2RT \approx 1 / 2m\langle v\rangle^2 \tag{1-59}$$

Finally, combining Eqs. (1-57) through (1-59) the following equation for the d.c. conductivity is derived.

$$\sigma_{dc} \approx \frac{ne^2 l_{mfp}}{\sqrt{3RTm}} \tag{1-60}$$

This approach predicts the upper limit of the conductivity, approximately 1 $(\Omega\ cm)^{-1}$ at the highest temperatures. It is also able to predict an appropriate temperature at which the non-Arrhenius behavior starts to take an effect. However, at the low temperatures it over estimates the Arrhenius portions of the d.c. conductivity behavior.

At this point, with this model it has been shown that it is possible to fit the low temperature Arrhenius behavior with the DAE model and the high temperature non-Arrhenius behavior with the ion-ion scattering model separately. An extension is needed to coalesce the aspects of both models into one uniform approach. In this way, both the Arrhenius and non-Arrhenius portions of the conductivity could be fitted simultaneously with reasonable physical parameters.

This leads to the development of a new Ion Trapping Model (ITM) which will be derived and discussed in CHAPTER 4 which does accurately fit both the Arrhenius and non-Arrhenius regions of the conductivity data presented in this study.

1.5 Conclusion

A comprehensive review of glass preparation and structure has been given. Current theories of ionic conductivity have also been discussed. Though considerable progress has been made, the root cause of non-Arrhenius conductivity behavior at higher temperatures still remains unexplained. The next chapters will investigate this non-Arrhenius behavior in lithium fast ionic conducting systems. Results from IR, Raman, NMR, and a.c. impedance spectroscopy will be analyzed and discussed. In the end, an ion trapping model which has been developed will be introduced and the physical implications in presents will be explored.

Table 1-1 Parameters from KWW fits to experimental data[25].

	x = 0.35	x = 0.45	x = 0.55
β_σ	0.43	0.44	--
$\Delta E_{a\,\sigma}^{*}/k_B$ (K)	5230	4730	--
$\tau_{0\,\sigma}^{*}$	2×10^{-15}	2×10^{-15}	--
β_{NMP}	0.39	0.34	0.37
$\Delta E_{a\,NMR}^{*}/k_B$ (K)	6200	5750	5100
$C(rad/s)^2$	8.5×10^9	10.5×10^9	8.0×10^9

Table 1-2 Parameters from DAE using Lorentzian fraction = 0.2.[25]

	x = 0.35	x = 0.45	x = 0.55
$\Delta E_m/k_B$ (K)	6100	5650	5000
$\Delta E_b/k_B$ (K)	1100	1100	1000
$C(rad/s)^2$	10.2×10^9	8.0×10^9	7.8×10^9
$\Delta E_p/k_B$ (K)	5600	5100	--
P	0.321	0.305	--
$\Delta E_l/k_B$ (K)	1150	1150	1150

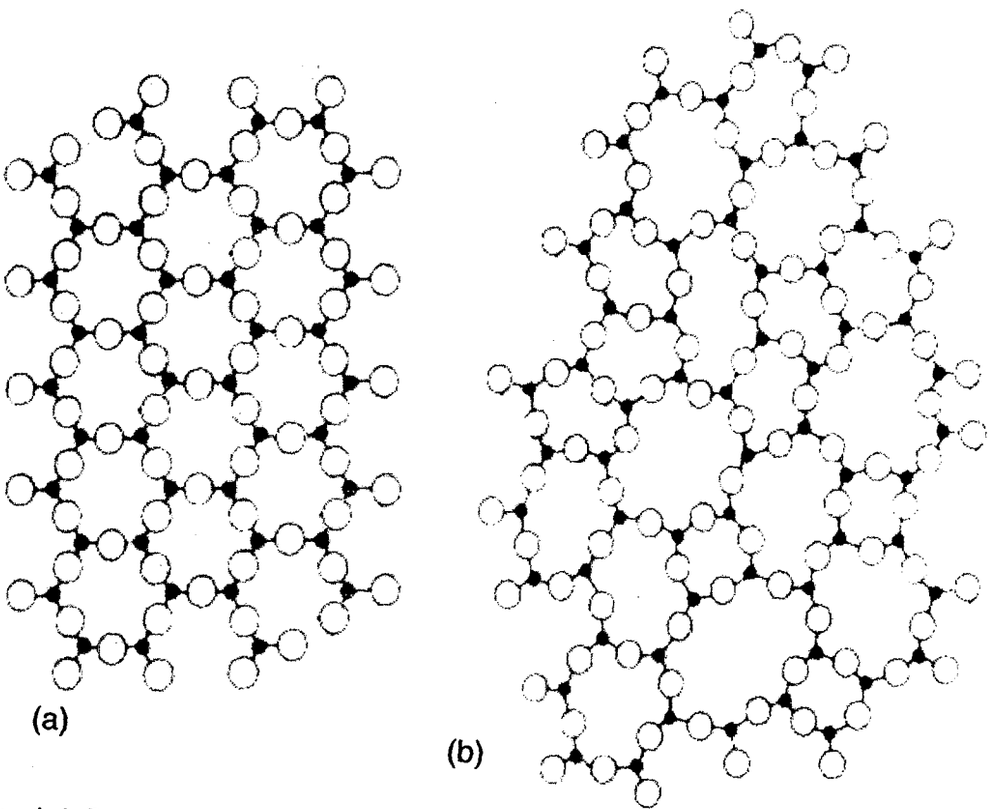

Figure 1.1 Comparison between (a) crystalline structure and (b) glassy structure.[5]

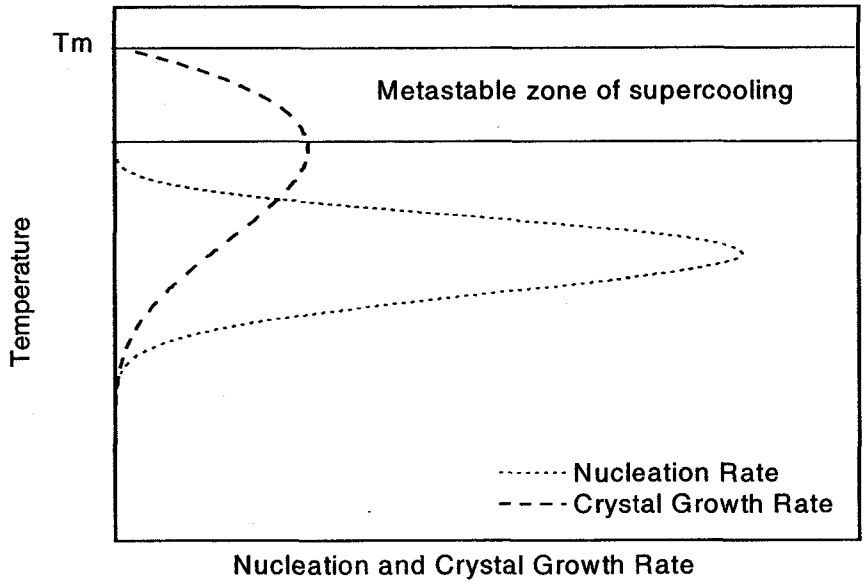

Figure 1.2 Temperature dependence of nucleation and crystal growth rates.

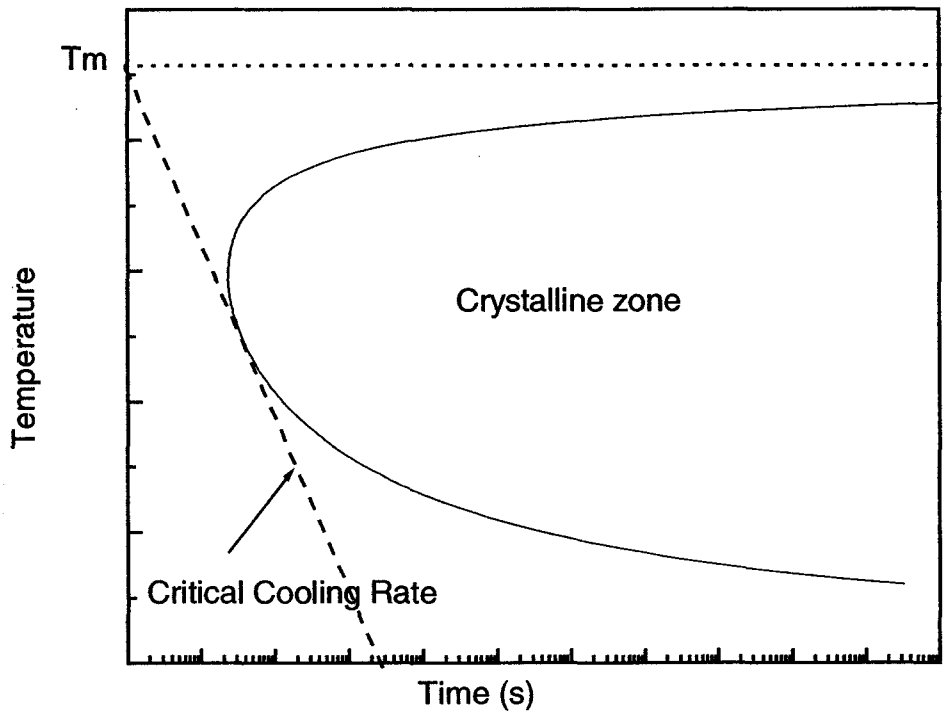

Figure 1.3 Time - Temperature - Transformation diagram showing critical cooling rate.

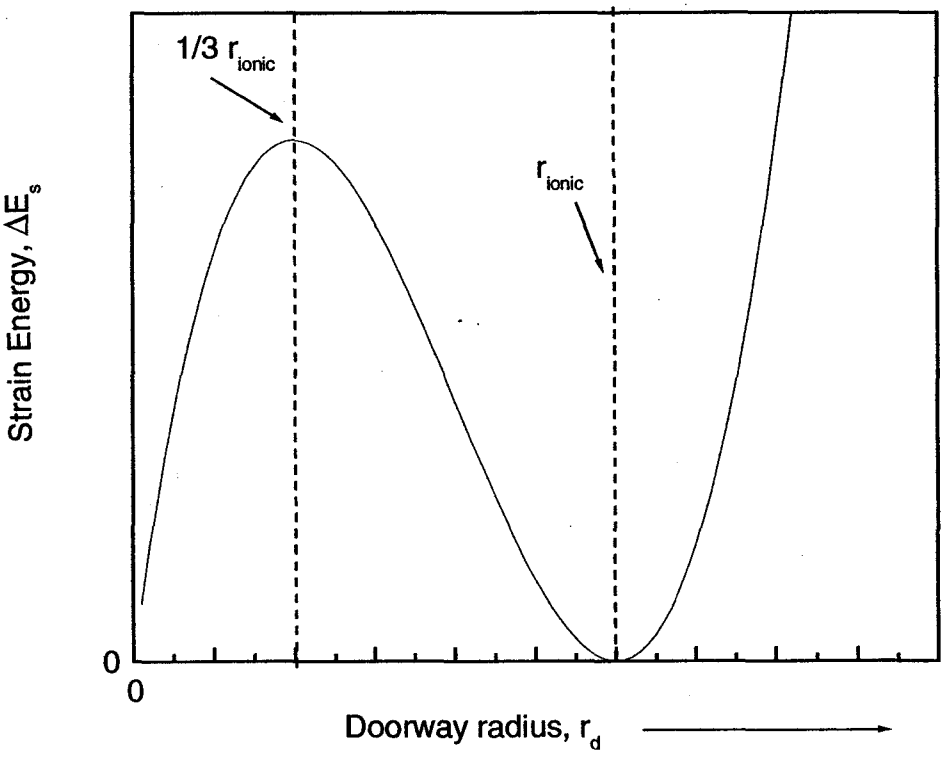

Figure 1.4 Plot of strain energy versus doorway radius from Anderson – Stuart model.[13]

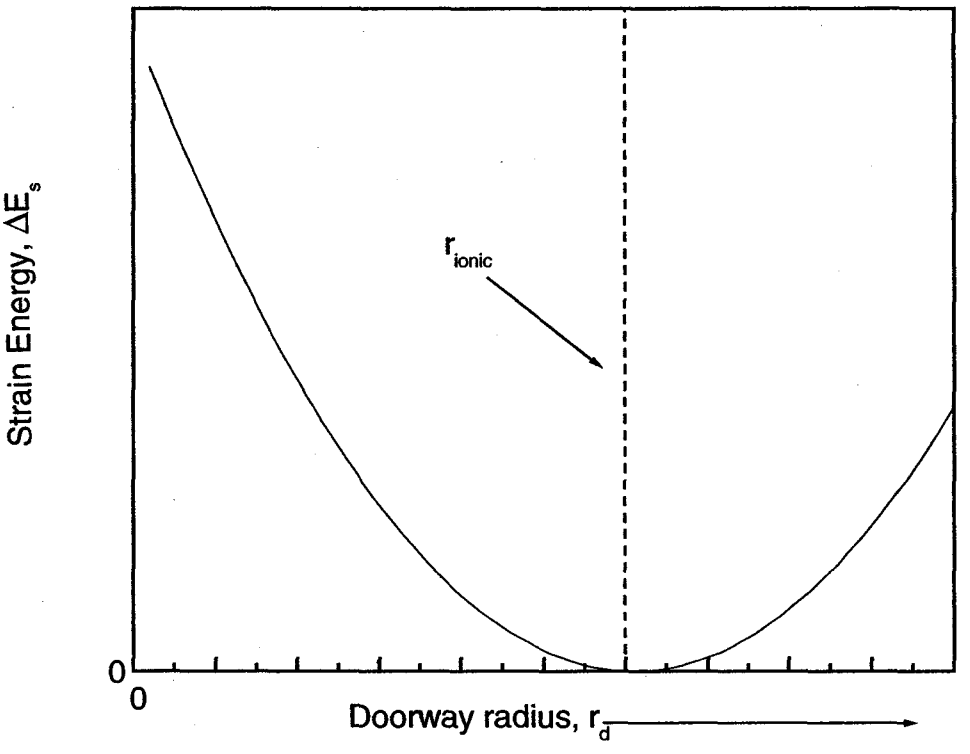

Figure 1.5 McElfresh and Howitt's correction for strain energy versus doorway radius.[14]

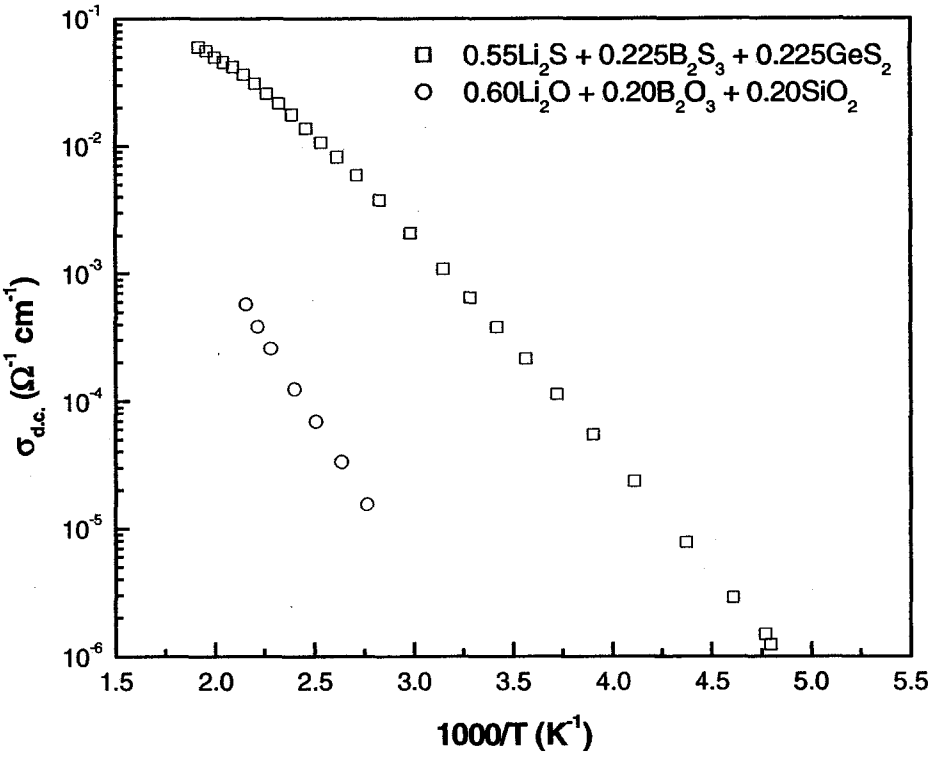

Figure 1.6 Comparison showing enhanced conductivity of sulfide systems.

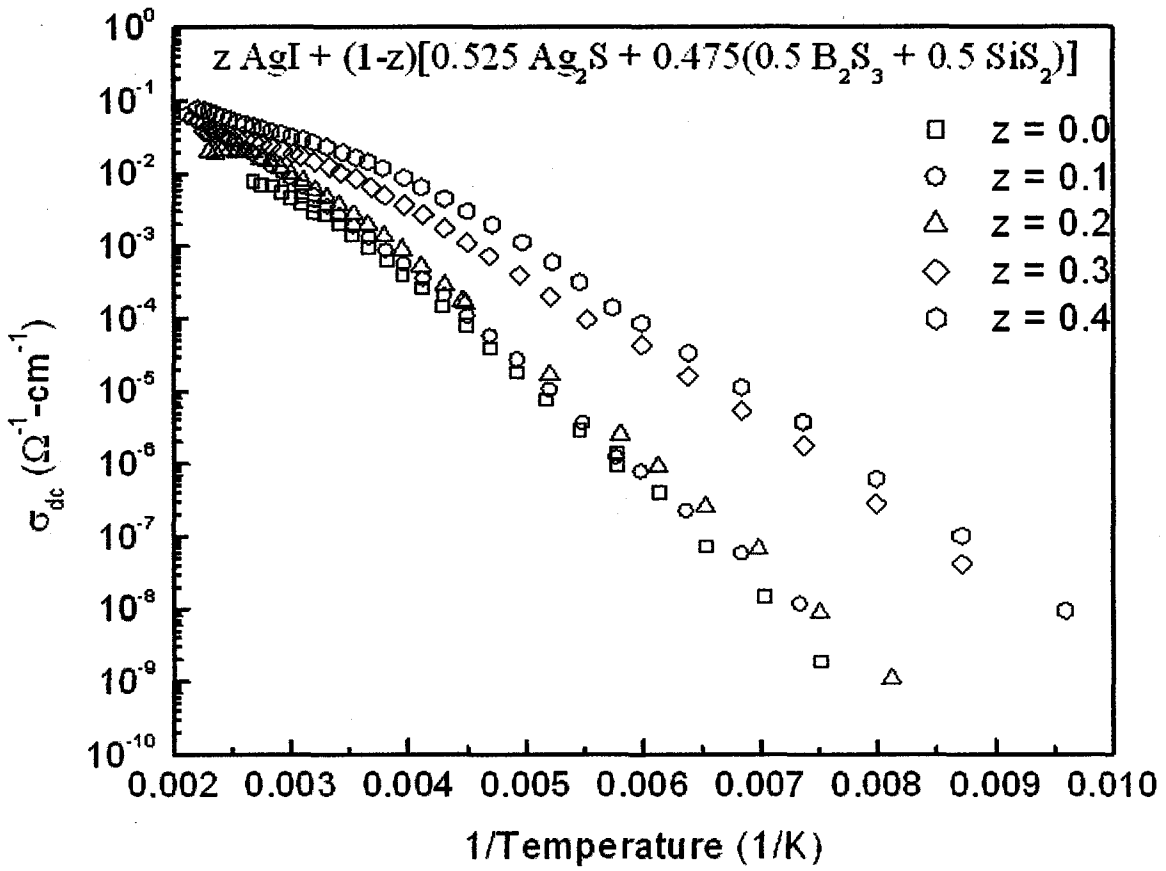

Figure 1.7 D.C. conductivity of silver thio-boro-silicate glasses.[33]

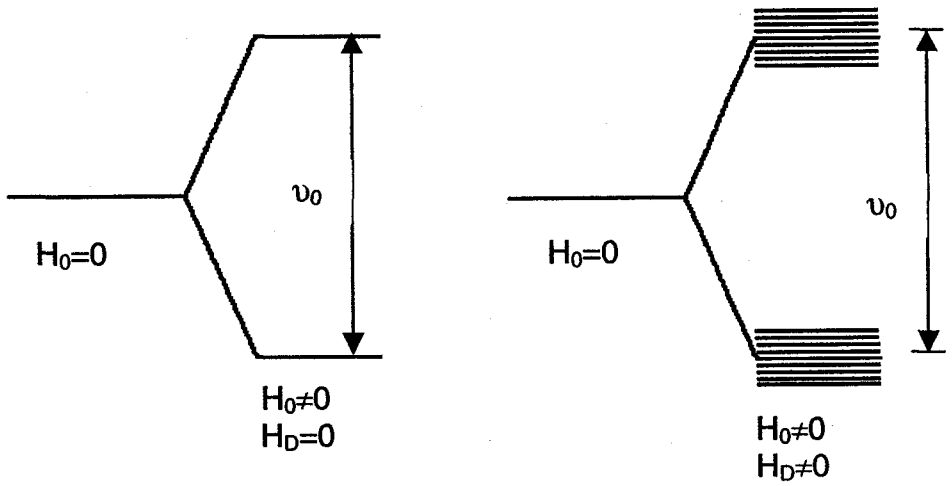

Figure 1.8 Energy level diagrams showing Zeeman splitting and dipolar broadening

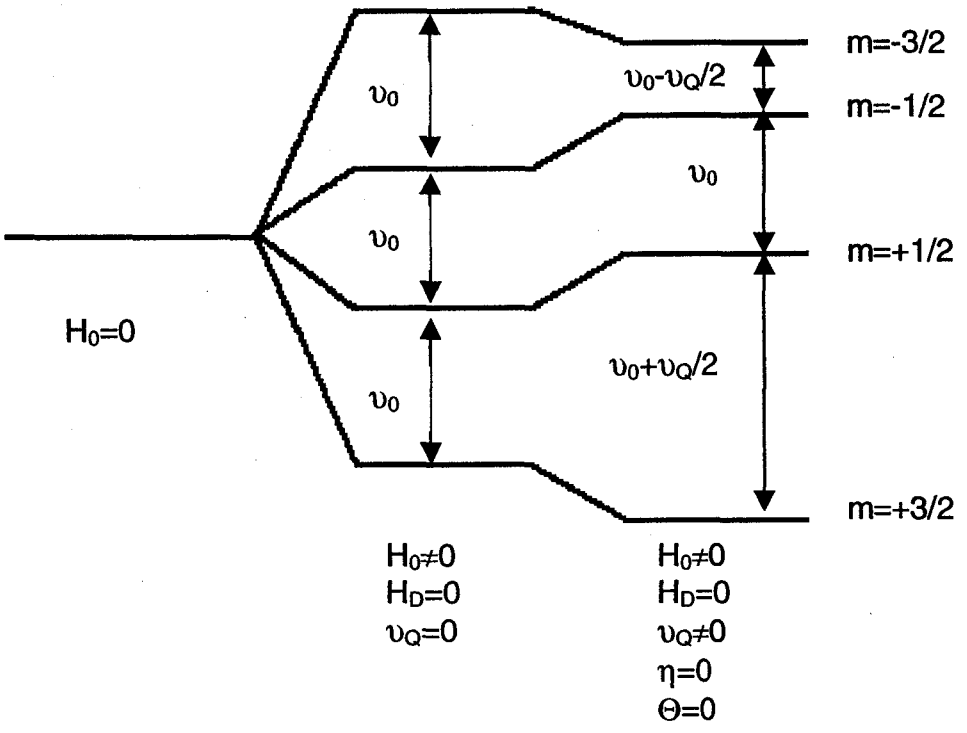

Figure 1.9 Energy level diagram showing the effects of quadrupolar interactions for a spin I = 3/2.

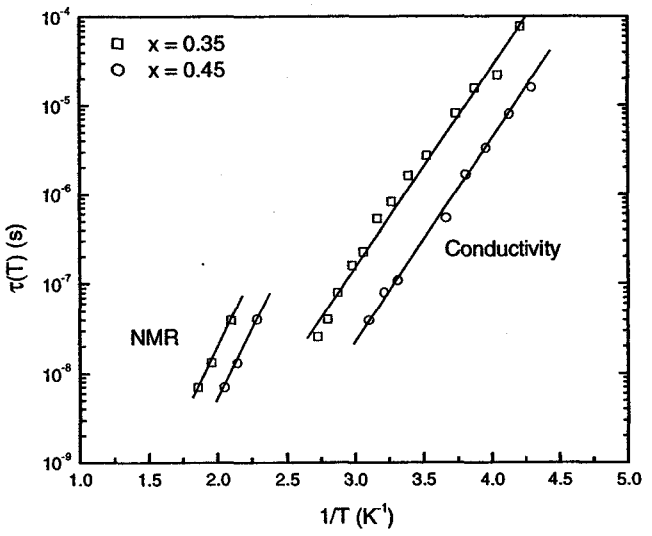

Figure 1.10 Comparison of $\tau_{NMR}(T)$ and $\tau_{\sigma}(T)$ for x = 0.45 and 0.55 of $xLi_2S + (1-x)GeS_2$ glasses.[25]

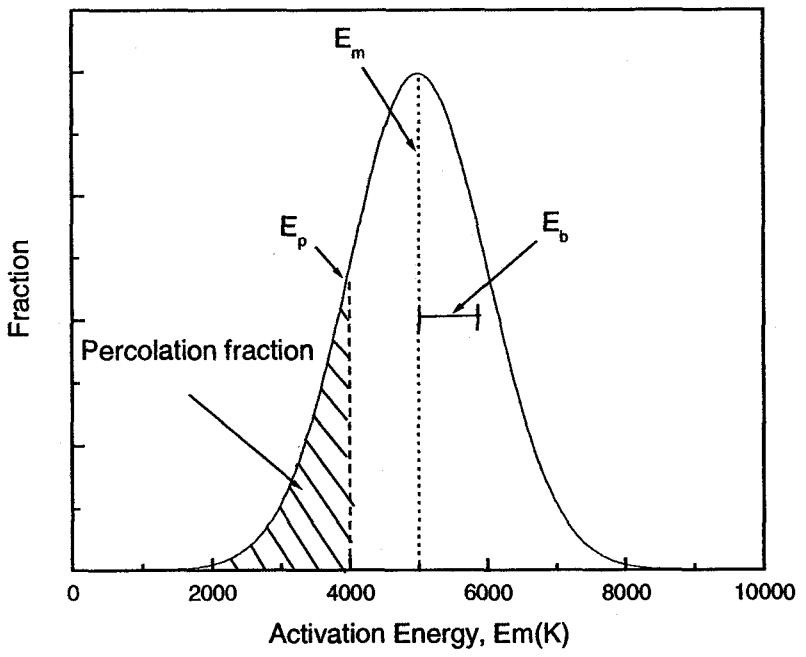

Figure 1.11 Gaussian DAE for a typical FIC glass.

1.6 References

[1] H.L. Tuller, M. Balkanski. Science and Technology of Fast Ion Conductor, NATO ASI Series B: Physics 199 (1989).
[2] C.A. Angell, Solid State Ionics **9/10**, 13 (1983).
[3] M.D. Ingram, M. A. Mackenzie, Solid State Ionics **40/41**, 671-675 (1990).
[4] Schrooten, J., Meyer, B., Martin, S.W., Submitted to Physical Review B: Condensed Matter Physics, Nov. 2001
[5] A. Varshneya. *Fundamentals of Inorganic Glasses.* Academic Press Inc., Boston (1994) 1.
[6] K.H. Sun, J. Am. Ceram. Soc. **30**, 277(1947).
[7] A. Dietzel, Z. Electrochem. **48**, 9-23 (1942).
[8] J.C. Phillips, J. Non-cryst. Sol. **34**, 153-181 (1979).
[9] J. Zarzycki. *Glasses and the Vitreous State.* Cambridge University Press, Cambridge (1991) 48.
[10] W.A. Johnson and R.F. Mehl, Trans. AIMME 135, 416 (1939).
[11] M. Avrami, J. Chem. Phys. 7, 1103 (1939).
[12] Urnes, S. Physics and Chemistry of Glasses. 8(3),125-6 (1967).
[13] O.L. Anerson, D.A. Stuart, Journal of the American Ceramics Society **37**, 573 (1954).
[14] D. McElfresh, D. Howitt, Journal of the American Ceramics Society 69, C237-C238 (1986).
[15] C.P. Slichter, Principles of Magnet Resonance, 3rd Edition., Spring Series in Solid State Sciences Vol. 1, Spring-Verlag, Berlin (1990).
[16] E. Fukushima. *Experimental Pulse NMR: A Nuts and Bolts Approach.* Addison-Wesley Publishing Company, Reading, Massachusetts (1981).
[17] N. Bloembergen, E.M. Purcell and R.V. Pund, Phys. Rev. **73**, 679 (1948).
[18] G. Williams and P.J. Hains, Faraday Symp. Chem. Soc. **6**, 14 (1972).
[19] F. Borsa, D.R. Torgeson, S.W. martin and H.K. Patel, Phys. Rev. B **46**, 795 (1992).
[20] V. Provenzano, L.P. Boesch, V. Volterra, C.T. Moynihan and P.B. Macedo, Journal of the American Ceramics Society **55**, 492 (1972).
[21] M. Dishon, G.H. Weiss and J.T. Bendler, J. Res. Natl. Bur. Stand. **90**, 27 (1985).
[22] A. Abragam, *Principles of Nuclear Magnetism*, Clarendon Press, Oxford (1961).
[23] K.L Ngai, Phys. Rev. B **48**, 13481 (1993).
[24] J. Macdonald, Journal of Applied Physics **84**, 812 (1998).
[25] K. H. Kim, D. R. Torgeson, F. Borsa, J. Cho, S. W. Martin, I. Savre. Solid State Ionics **91**, 7-19 (1996).
[26] I. Savre, F. Borsa, D.R. Torgeson and S.W. Martin. Phys. Rev. B **48**, 9336 (1993).
[27] S.R. Elliot. *Physics of Amorphous Materials,* Longman, New York (1990).
[28] J.C. Dyre. J. Appli. Phys. **64**, 2456 (1988).
[29] A. Pradel, M. Ribes, Mater. Sci. Eng. B **3**, 45 (1989).
[30] A. Pradel, M. Ribes, Mater. Chem. Phys. **23**, 121 (1989).

[31] S. W. Martin, J. Am. Ceram. Soc. **74**, 1767 (1991).
[32] J. Kincs, M.S. thesis, Iowa State University, Ames, Iowa (1994).
[33] K.L. Ngai, A.K. Rizos, Physical Review Letters, **76**(8),1296-1299 (1996).
[34] S.W. Martin, J.Schrooten, B. Meyer. Journal of Non-Crystalline Solids. **307-310**, 981-991 (2002).
[35] J.Schrooten, Ph.D. Thesis, Iowa State University, Ames, Iowa (2001).
[36] M. Tatsumisago, C.A. Angell, and S.W. Martin, J. chem.. Phys. **97**, 274 (1992).
[37] K.L. Ngai, J. Chem. Phys. **98**, 6426 (1993).

CHAPTER 2 PREPARATION AND CHARACTERIZATION OF BORON OXYSULFIDE GLASSES

By

J. Schrooten[a], B. Meyer[a,b], S. W. Martin[a,c], F. Borsa[b]

Submitted to

Journal of Non-Crystalline Solids,

September 2002

[a] Department of Materials Science & Engineering, Iowa State University, Ames, IA 50011

[b] Ames Laboratory – U.S. Department of Energy, Iowa State University, Ames, IA 50011

[c] Author to whom correspondence should be directed

2.1 Abstract

Stable, homogeneous $xB_2O_3 + (1-x)B_2S_3$ glasses were prepared between $0 \leq x \leq 0.80$. It was not possible to prepare homogeneous, stable glasses of compositions $0.85 \leq x \leq 0.95$ due to a strong exothermic enthalpy of mixing between the B_2S_3 and B_2O_3 phases. Raman, IR, and ^{11}B NMR spectroscopies, used to characterize the structure of the glasses, show that the boron oxide structures of B_2O_3, especially the six-membered (thioboroxol) rings, quickly diminish with increasing sulfide content, whereas the corresponding sulfide structures in B_2S_3 remain relatively high in concentration as the oxide content is increased. Differential scanning calorimetry (DSC) and density measurements, used to characterize the physical properties of the glasses, show that the physical properties of these boron oxysulfide glasses heavily favor the properties of B_2S_3 regardless of the amount of B_2O_3 added to the system. It is hypothesized that the stability of the thioboroxol ring group relative to that of the $BS_{3/2}$ trigonal group is a possible source of this behavior. It is suggested that the large heat of mixing for B_2O_3-rich glasses is associated with the formation of new mixed boron oxysulfide structures of composition BS_zO_{3-z} where $0 < z < 3$.

2.2 Introduction

Boron oxysulfide glasses are prepared by mixing boron sulfide (B_2S_3) and boron oxide (B_2O_3) glasses. Borate and thioborate glasses have been extensively studied and characterized as separate glasses.[1,2] B_2S_3-based glasses doped with high fractions of alkali sulfides have been shown to exhibit fast ionic conductivity, an important property for use as electrolytes in batteries or fuel cells.[3,4] Most B_2S_3-based glasses are known to be highly reactive with both water and oxygen.[5] In contrast to the thioborates, the chemical stability of many borate glasses has been well documented[6]; however, their conductivity is quite low.[7] The combination of sulfide and oxide glasses into boron oxysulfide glasses hold potential as chemically durable fast ion conducting (FIC) glasses for use in fuel cells and solid-state batteries. The addition of B_2O_3 to B_2S_3 may allow for a glass composition that is both stable in air and water as well as exhibiting fast ionic conduction.

Mixed oxysulfides are not unique to boron systems. The concept of oxysulfide materials is well known and extensively studied and examples include $MoS_{2-x}O_x$, V_2O_4S, and $TiO_{0.3}S_{1.5}$.[8,9,10]

Another motivation for this study is that during preparation, sulfide glasses often become contaminated with oxygen.[11] The physical property effect that this oxide contamination has on bulk thioborate glasses was previously unknown. This current study investigated the effect of the sulfur for oxygen substitution upon the physical properties and structure of the glasses. This study shows that the physical

properties of these glasses closely follow those of B_2S_3 and show little dependence on oxygen concentration.

B_2S_3 and B_2O_3 glasses are found to be isostructural, excepting for bond distance differences.[12] The basic unit for both of these glasses is a trigonal boron unit that can be independent (loose) or arranged into six-membered ring structures.[13,14] In B_2O_3, the rings are known as boroxol rings; in B_2S_3, the rings are known as thioboroxol rings. In pure B_2S_3 and B_2O_3, both neutron and NMR studies of these glasses show 25% of the boron atoms are found in trigonal units and 75% of the boron is found in six-membered rings. This results in an equal number of six-membered rings and trigonal units.[15,16,17]

The combination of B_2S_3 and B_2O_3 in an oxysulfide glass may cause a sulfur for oxygen substitution resulting in new structural units of the form of BS_zO_{3-z} where z is 1 or 2. The natural question then becomes, since these glasses both exhibit loose trigonal units and trigonal units in six-member rings, which trigonal unit will be substituted first by the added S to the oxide glass B_2O_3 and the added O to the sulfide glass B_2S_3. From our work on B_2S_3, we have found that the thioboroxyl rings appear to be attacked by added modifier, M_2S, only after the modifier has consumed the available loose trigonal units to form tetrahedral borons. A similar preference of added oxide modifier M_2O for the loose borate trigonal units has also been observed. These observations suggest that the six-membered ring units in both the oxide and sulfide glasses are more energetically stable than the loose trigonal units. This would imply that in turn the six-membered rings would have a preferred stability

over loose trigonal units in the presence of the other added anion, $S^{=}$ to the oxide glass and $O^{=}$ to the sulfide glass.

A further question is the relative stability of the six-membered rings to one another. The results presented in this work suggest, surprisingly, that the thioboroxyl rings have an inherent chemical stability in the presence of added B_2O_3 over that of the loose trigonal units. For this reason, it is thought that the oxygen first substitutes for the sulfur in the loose triangles enabling the sulfide thioboroxol rings to exist to higher oxygen concentrations.

2.3 Experimental

2.3.1 Preparation of the Glasses

B_2S_3 was prepared through the reaction of stoichiometric amounts of amorphous boron (99.9+%) and sulfur (99.999%) powders. This investigation used a modified version of the method reported by Martin and Bloyer[18], where the batch size was increased from 3 to 40 grams by using a larger quartz ampoule that could hold more starting material. The interior of a large quartz ampoule (~500 ml) was coated with pyrolytic carbon through the anaerobic decomposition of acetone. Stoichiometric amounts of boron and sulfur powders were placed inside of the ampoule that was then evacuated and sealed. The ampoule was then heated according to the schedule shown in Table (2-1) and then air cooled to room temperature.

The B_2O_3 that was used for the boron oxysulfide preparation was prepared through the decomposition of boric acid according to the reaction:

$$2H_3BO_3 \rightarrow B_2O_3 + 3H_2O \qquad (3\text{-}1)$$

Boric acid was placed into an alumina crucible, heated at 850°C for 1 hour, and then allowed to air quench. The temperature at which water is released from B_2O_3 is 300°C[19] and was confirmed by the NMR results that all residual H_2O had been released from the H_3BO_3 due to the lack of a tetrahedral boron resonance. The B_2O_3 was then immediately placed into a glovebox with <5 ppm H_2O and O_2. There was no evidence of crucible attack by the boric acid.

The boron oxysulfide glasses were heated to 900°C in a vitreous carbon crucible in a box furnace for 20 minutes after which the crucible was removed from the furnace and allowed to air cool to room temperature in the glovebox. Samples of $0 \leq x \leq 0.80$, and $x = 1$, where x is mole fraction B_2O_3, were glass forming by allowing the glass melt to cool to room temperature in the crucible. The glasses where generally a dark brown color (v-B_2S_3 is dark green).

For values of x between 0.85 and 0.95, the melts appeared to "explode", quite surprisingly, out of the crucible and in doing so completely coated the interior of the box furnace. While the origin of this behavior is unclear, stable glasses could not be formed in this compositional region. It is emphasized that these glasses were prepared in vitreous carbon crucibles. While B_2S_3 has a very low boiling point and must be prepared in a sealed, carbon coated silica tube; many homogeneous alkali modified boron sulfide glasses have been prepared by adding alkali sulfide to the base B_2S_3 glass and heating in vitreous carbon crucibles with little weight loss. Therefore in the absence of a very strong exothermic reaction or in the confines of a

sealed silica tube, it may be possible to form homogeneous glasses in the compositional range of 0.85 and 1.00 mol fraction of B_2O_3. Using a silica tube instead of the vitreous carbon crucible to prepare the $x > 0.8$ samples has not yet been attempted for these glasses, however.

2.3.2 Density Measurements

Density measurements were performed using Archimedes' method inside the glove box using kerosene as the suspending liquid.[20] These measurements are accurate to ± 0.01 g/cc.

2.3.3 Differential Scanning Calorimetry

Glass transition temperature measurements were performed using a Pyris 1 DSC$^+$ running Pyris software version 3.01. It has a temperature range of -170 to 750°C and a sensitivity of ±0.2 μW. All calorimetric measurements were performed by initially heating the sample above the glass transition temperature (~300°C), cooling at 10°C/min to 100°C, then reheating at 10°C/min. This was done to ensure all samples had a comparable thermal history. All DSC scans were determined by measuring the onset temperature of the thermal event. Typical sample sizes were 30 mg, and all samples were hermetically sealed into aluminum sample pans.

The Pyris 1 DSC has an advanced feature called Dynamic Differential Scanning Calorimetry (DDSC), typically known as modulated DSC on other systems. This technique applies a sinusoidal (dynamic) rate of temperature change rather than the linear temperature change used in traditional DSC. A typical method for DDSC

would be to heat the sample at 50°C/min for 5 degrees then cool at 5°C/min for 4 degrees. This greatly enhances the instruments sensitivity to weak transitions and allows for the resolution of transitions that occur close in temperature. The drawback is that DDSC scans have a very slow overall heating rate (~1°C/min), which greatly increases the time necessary to perform calorimetric measurements. This technique was used in the current investigation where many of the transitions had very small ΔC_p values and were very difficult to observe without this technique.

2.3.4 Raman Spectroscopy

Raman spectroscopy was performed using a FT-Raman Spectrometer. It uses an Nd:YAG Laser operating at 1064 nm as the excitation source and has a useful Stokes shift spectral range of 120 to 3600 cm^{-1}. Powder samples weighing less than 10 mg were used in a 180° backscatter experiment at powers of typically <100 mW to collect the Raman spectra.

2.3.5 Infrared Spectroscopy

Infra-red spectroscopy was performed using a FTIR spectrometer. The spectra were measured over the spectral range of 4400 to 400 cm^{-1} with a resolution of 2 cm^{-1}. KBr pellets were made by mixing together appropriate amounts of sample and dried KBr in a 1 to 20 mass ratio.

[+] Perkin Elmer-Instruments

2.3.6 Nuclear Magnetic Resonance Spectroscopy

^{11}B static and MAS NMR experiments were performed at 4.7 Telsa (64.179 MHz) to yield structural information about the $xB_2O_3 + (1-x)B_2S_3$ glass forming series. The effective $\pi/2$ pulse length was determined to be 3.0 μs using HBO_3 saturated in H_2O as a reference. Since ^{11}B is a quadrupolar nucleus with spin I = 3/2, a shorter pulse length ($\pi/8$) was used in order to avoid non-central line transitions. A spinning speed of 9.0 KHz in the MAS experiments was sufficient to separate out the spinning sidebands from the spectra. In both the static and MAS experiments, the data was acquired from the FID directly following a single pulse with five seconds delay between scans. Chemical shift for all spectra are in reference to $BF_3O(C_2H_5)_2$ where positive shifts are downfield.

2.4 Results

Figure (2.1) shows the Raman spectra for the boron oxysulfide glasses. Royle *et al.* [14] has identified and assigned the peaks in the B_2S_3 spectrum. The broad, asymmetric peaks at 1042 and 919 cm^{-1} and the symmetric peaks at 498 and 439 cm^{-1} are assigned to six-membered rings. The peaks at 388 and 771 cm^{-1} are assigned to loose trigonal $BS_{3/2}$ units.

Several investigators have identified and assigned the peaks in Raman spectra of B_2O_3.[21,22] The weak peaks at 471 and 599 cm^{-1} and the very strong peak at 808 cm^{-1} are assigned to six-membered ring units. The remaining weak peak at 664 cm^{-1} is assigned to loose trigonal $BO_{3/2}$ units.

As B_2O_3 is added to B_2S_3, the trigonal B_2S_3 peak at 771 cm^{-1} decreases in intensity and two new peaks grow in at 533 and 637 cm^{-1}. These peaks are tentatively assigned as $BS_{2/2}O_{1/2}$ at 533 cm^{-1} and $BS_{1/2}O_{2/2}$ at 637 cm^{-1}. This assignment is made by considering that the increased mass of the sulfur atom results in a lower vibrational frequency causing the sulfur rich unit to appear in the Raman spectra at lower wavenumbers. Table (2-2) summarizes these peak assignments. Not all peaks are present for all glasses. For example, the peak at 771 cm^{-1} is listed as high intensity for B_2S_3 and systematically decreases until there is no evidence of it in the x = 0.5 sample.Figure 2.2 shows the IR spectra for these glasses including that of pure B_2O_3 and pure B_2S_3. The B_2O_3 spectrum[23] shows the presence of primarily two peaks. A broad, intense, asymmetric peak appears approximately at 1245 cm^{-1}, while a less intense peak also appears around 720 cm^{-1}. The higher wave number mode has been associated to the B-O stretching modes of the $BO_{3/2}$ units. The lower wave number peak has been assigned to B-O-B bending. The 800 – 1200 cm^{-1} region is free of any IR active modes.

Likewise, the spectrum of pure B_2S_3 also shows predominately two peaks. The most intense peak at 772 cm^{-1} has been assigned to modes of the $BS_{3/2}$ groups, and the other peak at 990 cm^{-1} has been assigned to six-member rings.[24]

As for the oxythioborate compositions, at 10 molar percent, the presence of trigonal $BO_{3/2}$ units can be seen easily in the IR spectra. The peaks at 1254 and 721 cm^{-1} become visible. As B_2O_3 concentration is increased, the breaking up of the B_2S_3 six member ring occurs as well as the intensity of the peak at 772 cm^{-1} decreases. Two new peaks appear centered at 1100 and 810 cm^{-1}. The 1100 cm^{-1} peak

remains fairly constant in intensity from $0.2 \leq x \leq 0.7$. At both the $x = 0.1$ and 0.8 compositions, this peak starts to diminish. It is interesting to note that the mode at 1100 cm^{-1} is non-existent in the IR spectra of pure B_2O_3 and B_2S_3. Since both of these new peaks occur at higher wavenumbers than the B-S-B stretching mode between $BS_{3/2}$ units, it is likely that both of these modes are due to stretching modes of mixed $BO_zS_{(3-z)}$ units. It is proposed that the two modes are actually comprised of many modes associated with the different combinations of sulfur and oxygen atoms. Figure 2.3 shows the calculated peak positions for the different structural combinations. The force constants were calculated using Hooke's Law and assuming that the peak position of two trigonal borate units connected via an oxygen bridge bond was at 1254 cm^{-1}, and likewise for two trigonal thioborate units connected via a sulfur bridge bond to be at 772 cm^{-1}. The effective force constants were found to be 15.9 N/cm for the B-O-B stretch and 10.2 N/cm for the B-S-B stretch.

As can be seen from Figure 2.2, all of the calculated peak positions for the oxythioborate structures connected via an oxygen bridge bond are in the range of 1030 to 1200 cm^{-1}. New peaks were estimated by changing the reduced masses according to the new structures. Each structure consisted of 2 borons, one connecting oxygen or sulfur, and four outer bridging atoms, of which each one could be sulfur or oxygen. With five atoms being either oxygen or sulfur, there are thirty-two different total possible combinations, of which only twelve give rise to unique vibrational stretching modes. The calculations also show that the oxythioborate structures connected via a sulfur bridge bond are in the range of 800 to 910 cm^{-1}.

At lower x values ($x < 0.5$), the peak maximum falls slightly outside to lower wavenumbers of the calculated range. Due to the elementary nature of the calculations used, exact agreement between the calculated and the observed wavenumber ranges is not expected. However, the agreement between calculation and experiment is still good. This strongly suggests that the resulting new broad peaks could arise from the combination of all of these different structures. This further suggests that these new modes are evidence of new oxythioborate structures forming in the glass as opposed to the glasses being comprised of phase separated borate and thioborate regions which would be evidenced by only a change in the intensity of existing modes and not any change in the frequencies of the modes.

Figure (2.4) shows a DDSC scan for the 0.35 B_2O_3 + 0.65 B_2S_3 composition. Due to the very sensitive nature of DDSC, very small thermal events can be resolved. Since the B_2S_3 and B_2O_3 glass transition temperatures differ by 40 °C, it would be expected that if the samples were phase separated into two separate regions the presence of two distinct T_g signatures would be present. Since only one transition is seen, it is probable that the samples are homogeneous. Optical observations of the glasses confirm their single-phase nature.

Figures (2.5) and (2.6) show the density and T_g trends for the glasses. Notice that there is very little dependence on the presence of B_2O_3. The properties appear to favor the B_2S_3 values.

The density exhibits a shallow, broad minimum centered on $x = 0.5$ which only amounts to a density difference of 0.1 g/cc. The T_g data exhibits a similar broad minimum, but due to the lower T_g of B_2O_3 compared to B_2S_3 must sharply decrease

at the end of the glass forming range. The error bars were determined from the standard deviation of multiple measurements at each individual composition. The T_g measurements were made by determining the onset of the endothermic peak due to the softening of the glass. Errors associated with the T_g measurements are dependent upon the certainty of extrapolation of the onset temperature with each composition.

The ^{11}B NMR static spectra of pure glassy B_2S_3 and pure B_2O_3 are shown in Fig. (2.7). Due to the large dipolar broadening in the spectra, the static spectra shown in Fig. (2.8) did not yield any significant information about the structure of the oxythioborate glasses over the entire x B_2O_3 + (1-x) B_2S_3 compositional range. Since the chemical shift values were masked by the dipolar broadening, the static spectra were ambiguous in determining whether the glass structure was comprised of a simple combination of pure BO_3 and BS_3 trigonal units or of additional new trigonal structures such as BO_1S_2 and BO_2S_1.

For this reason, MAS NMR experiments were used to remove the dipolar effects to reveal the structural characteristics of the glasses. Figure (2.9) shows the ^{11}B MAS spectra for both pure glassy B_2O_3 and B_2S_3. In both cases, the quadrupolar split line shape is characteristic of ^{11}B in trigonal coordination.[25] The peak shape arises from quadrupolar splitting of the central line transition when ^{11}B is in the trigonal coordination as isolated triangles or as boroxol rings. Thus, at the short-range order, pure B_2O_3 is comprised of BO_3 units and pure B_2S_3 is comprised of BS_3 units as expected.

If the B_2O_3 and B_2S_3 components were to separate into separate phases, it would be expected to see NMR spectra that would resemble the addition of the pure B_2S_3 and pure B_2O_3 spectra in corresponding ratios. However, Fig. (2.10) shows that four new peaks appear for the x B_2O_3 + (1-x) B_2S_3 glasses. Due to the lack of alkali modifier in these borate and thioborate glasses, it is unlikely that the new sites would be tetrahedral borons.[20] This suggests two new trigonal boron units (each trigonal site accounts for two peaks), BOS_2 and BO_2S.

S. J. Hwang[11] performed ^{11}B MAS experiments to determine the oxide contamination found in pure v-B_2S_3. It was found that the oxygen contamination appeared in the form of BOS_2 and BO_2S units. Table (2-3) shows the isotropic chemical shift values for these structural units found from their study. This allows for the assignment of P1 to the BOS_2 unit and P2 to the BO_2S unit. An analysis of the widths of the quadrupolar splitting of all the possible peak combinations suggests that P1 and P3 belong to BOS_2 unit and that P2 and P4 belong to the BO_2S unit, see Table (2-4). Any other combination yields values that differ significantly from the splitting width of 2.659 kHz and 2.842 kHz for pure B_2S_3 and pure B_2O_3, respectively.

2.5 Discussion

Homogeneous mixed boron oxysulfide glasses could be prepared over the range of $0 \leq x \leq 0.8$, where x is the mol fraction of B_2O_3. For the compositions where x = 0.85, 0.90, and 0.95 the samples were not glassforming. By observation of the condition of the furnace, it was obvious that an extremely exothermic event

had occurred causing the sample to boil and splatter, completely coating the inside of the furnace. It is hypothesized that there is a strong enthalpy of mixing between B_2S_3 and B_2O_3 and is released upon the formation of the proposed structural groups B_2S_2O and B_2SO_2, this is discussed in detail below.

DSC and density measurements show that the physical properties of these mixed boron oxysulfides follow the properties of B_2S_3 regardless of the amount of B_2O_3 added to the system. The NMR and Raman results show that the peak intensities for the oxide structures, particularly the six-membered rings, quickly diminish with increasing sulfide content, whereas the peaks for the sulfide structures remain relatively intense as the oxide content is increased. It appears that the six-membered rings of the oxide structure (boroxol rings) are broken up first by the added sulfur atoms, but that the loose trigonal units in B_2S_3 are the ones first targeted by oxygen atoms. Comparing these observations leads to the conclusion that the B_2S_3 six-membered ring (thioboroxol ring) is more chemically robust to increasing oxygen concentration than the boroxol ring is to increasing sulfide concentration.

To determine the amount of B_2S_3 that would be needed to destroy all of the boroxol rings in B_2O_3, we begin by taking one mole of B_2O_3, which is 1.204×10^{24} B atoms. Earlier it was shown that 75% of the boron atoms are in boroxol rings, however, since there are three boron atoms in each ring this leads to only 4.013×10^{23} boroxol rings being present. Assuming that one sulfur atom will destroy one boroxol ring means that the addition of 4.013×10^{23} sulfur atoms will destroy all of the boroxol rings. This is equivalent to 0.22 moles of B_2S_3. So, at a composition of

0.19 B_2S_3 + 0.81 B_2O_3 all of the boroxol rings could be modified by the added S. Glass samples of 0 to 0.15 B_2S_3 could not be made due to the exothermic nature of the glass melt. Perhaps the destruction of the more unstable boroxol rings is an exothermic event that releases a sufficient amount of energy to boil the glass melt. The addition of 20% B_2S_3 may add sufficient mass to the melt to adequately absorb the exothermic heat without boiling, explaining the behavior seen in compositions of more than 20% B_2S_3.

A possible explanation with the increased robustness of the thioboroxol rings may arise from the pi-orbital stabilization by the sulfur atoms. Since sulfur is 3s3p with more electrons than oxygen (2s2p), perhaps there is sufficient overlap of the pi-orbitals of the sulfur and boron in the 6-membered ring to allow for stabilization. A similar effect is seen in alkali thioborates[2] where the alkali ion attacks the loose trigonal units of the thioborate before the six-membered rings are attacked.

A second possible explanation for the robustness of thioboroxol rings may be due to the deformation ability of a thioboroxol ring compared to that of a boroxol ring. Perhaps a thioboroxol ring can accept the strain induced when one of the sulfur atoms is replaced with an oxygen atom. If this were the case, it would be expected that there would be a shift in the Raman spectra for the thioboroxol rings. Since this shift is not observed, this hypothesis is unlikely.

The density and T_g trends may also be explained by the robustness of the thioboroxol rings. The density of a thioboroxol ring unit will be less than the density of three trigonal units due to the open structure of a ring. Since 75% of the boron atoms are in thioboroxol rings, the density of pure B_2S_3 should be determined

primarily by the density of the thioboroxol ring. If the added oxygen first reacts with the trigonal units, then the density of the oxysulfide glass would favor the density of pure B_2S_3. The minimum in the density curve at x = 0.5 could be the result of added free volume from the formation of BS_2O and BSO_2 units, whose presence is shown by NMR. At x = 0.0 there are no BS_2O and BSO_2 units present. As the B_2O_3 concentration is increased, the number of BS_2O and BSO_2 units will also increase and maximize at the x=0.5 composition. At higher B_2O_3 concentrations, the number of BS_2O and BSO_2 units will start to decrease resulting in the density going back up.

This investigation proposes that the thioboroxol rings are the more stable part of the B_2S_3 network and as such would determine the glass transition temperature of the glass. This improved stability of the thioboroxol ring would be the reason for the higher glass transition temperature compared to B_2O_3. Since these structures are those last targeted by the added oxygen, then the glass transition temperature of the oxysulfide glass should be similar to that of B_2S_3.

2.6 Conclusions

Glasses in the $xB_2O_3 + (1-x)B_2S_3$ (boron oxysulfide) system were prepared and characterized for the first time. Homogeneous glasses could be prepared for $0 < x < 0.8$, where the compositions are strongly glass forming. The density and glass transition temperatures were measured and found to vary little with composition; and is attributed to the robustness of B_2S_3 six-membered rings. Unexpected behavior is observed for compositions of $0.8 < x < 0.95$ where the samples appear to exhibit a

strong exothermic reaction on mixing. The cause for the extra heat of mixing is associated with the formation of new mixed boron oxysulfide structures, which is supported by observed new spectral features in the Raman and NMR spectra of these glasses.

2.7 Acknowledgements

The authors would like to thank Chad Martindale and Michael Royle for their assistance in preparation and characterization of the glasses in this study. This work supported in part by NSF-DMR 99-72466.

2.8 References

[1] Feller, S., *Phys. Chem. Glasses*, **41**(5), 211-215 (2000).
[2] Cho, J., Masters Thesis, Iowa State University (1992).
[3] Kincs, J., Martin, S.W., *Phys. Rev. Let.*, **76**, 70-73 (1996).
[4] Schrooten, J. Meyer, B., Martin, S.W., to be published.
[5] Bloyer, D., Masters Thesis, Iowa State University (1989).
[6] Gol'dshtein, L. M. Orenbakh, M. S. Gorpinenko, M. S., *Izv. Akad. Nauk SSSR, Neorg. Mater,* **16**(11), 1975-7 (1980).
[7] Martin, S.W., *J. Am. Ceram. Soc*, **71**(6), 438-45 (1988).
[8] Meunier, G., Dormoy, R., Levasseur, A, *Thin Solid Films*, 205, 213-217 (1991).
[9] Lince, J., *J. Mater. Res.*, **5**(1), 218-222 (1990).
[10] Tchangbedji, G., Prouzet, E., Ouvrard, G., *Materials Science Forum* Vols. 152-153, 319-322 (1994).
[11] Hwang, S. J., Fernandez, *C. Solid State Nucl. Magn. Reson.*, **8**(2), 109-121 (1997).
[12] Royle, M., Cho, J., Martin, S.W., *J. Non-Cryst. Sol.,* in press.
[13] Zarzycki, J. Glasses and the Vitreous State, Cambridge University Press (1991).
[14] Royle, M., Cho, J., Martin, S. W. *J. Non-Cryst. Solids*, **279**(2-3), 97-109 (2001).
[15] Hannon, Alex C.; Grimley, David I.; Hulme, Robert A.; Wright, Adrian C.; Sinclair, Roger N. Journal of Non-Crystalline Solids (1994), 177 299-316.
[16] Joo, C.; Werner-Zwanziger, U.; Zwanziger, J. W. Journal of Non-Crystalline Solids (2000), 261(1-3), 282-286.
[17] Sinclair, Roger N.; Stone, Cora E.; Wright, Adrian C.; Martin, Steve W.; Royle, Michael L.; Hannon, Alex C. Journal of Non-Crystalline Solids (2001), 293-295 383-388.
[18] Martin, S. W., Bloyer, D., *J. Am. Ceram. Soc.*, **74**, 1003 (1991).
[19] CRC Handbook of Chemistry and Physics., **72**, (1992).
[20] Varshneya, A., Fundamentals of Inorganic Glasses, Academic Press, Inc. (1994).
[21] Windisch, C.F., Risen, W.M., *J. Non-Cryst. Solids,* 48, 307-323 (1982).
[22] Galeener, F.L., Lucovsky, G., Mikkelsen, J.C., *Phys. Rev. B,* **22**(8), 3983-3990 (1980).
[23] E.I Kamitsos, A.P. Patsis, M.A. Karakassides, G.d. Chryssikos, J. Non-Cryst. Solids 126 (1990) .339.
[24] S.W. Martin and D.R. Bloyer, J. Amer. Ceram. Soc. 73 (1990) 3481.
[25] Sills, J.A., Martin, S.W., *J. Non-Cryst. Solids,* **175**(2,3), 270-7 (1994).
[26] H. Norh and B. Wrackmeyer, Nuclear Magnetic Resonance Spectroscopy of Boron Compounds, in P. Diehl, E. Fluck and R. Kosfeld(Eds.), NMR Basic Principles and Progress, Vol 14, Springer-Verlag, Berlin (1978).

Table 2-1 Heating schedule for preparation of B_2S_3.

Heat Rate (°C/min)	Temperature (°C)	Hold Time (min)
3	450	60
3	650	60
3	850	480

Table 2-2 Raman peak assignments for $xB_2S_3 + (1-x)B_2O_3$.

Wavenumber (cm^{-1})	Intensity	Assignment
321	Med.	6-membered ring $B_3S_3S_{3/2}$
388	Med.	Trigonal units $BS_{3/2}$
439	Med.	6-membered ring $B_3S_3S_{3/2}$
471	Low	6-membered ring $B_3O_3O_{3/2}$
498	Med.	6-membered ring $B_3S_3S_{3/2}$
533	Med	Proposed $B_2O_1S_2$
599	Low	6-membered ring $B_3O_3O_{3/2}$
637	Low	Proposed $B_2O_2S_1$
664	Low	Trigonal units $BO_{3/2}$
771	High	Trigonal units $BS_{3/2}$
808	High	6-membered ring B_2O_3
919	Med.	6-membered ring B_2S_3
1042	Med.	6-membered ring B_2S_3

Table 2-3 Isotropic Chemical shift (ppm) values for trigonal boron units.

Structural Unit	x B_2O_3 + (1-x) B_2S_3 glass (ppm)	Literature reference (ppm)
BS_3	63	63.6[21]
BOS_2	48	45.8[21]
BO_2S	31	30.3[21]
BO_3	17	17.4[11]

*ppm shifts are with reference to $BF_3O(C_2H_5)_2$

Table 2-4 Comparison of possible quadrupolar splitting values.

Combination	Pair 1	Width (kHz) at 4.7 Tesla	Pair 2	Width (kHz) at 4.7 Tesla
1	P1 and P2	1.054	P3 and P4	1.131
2	P1 and P4	3.850	P2 and P3	1.680
3	P1 and P3	2.735	P2 and P4	2.814

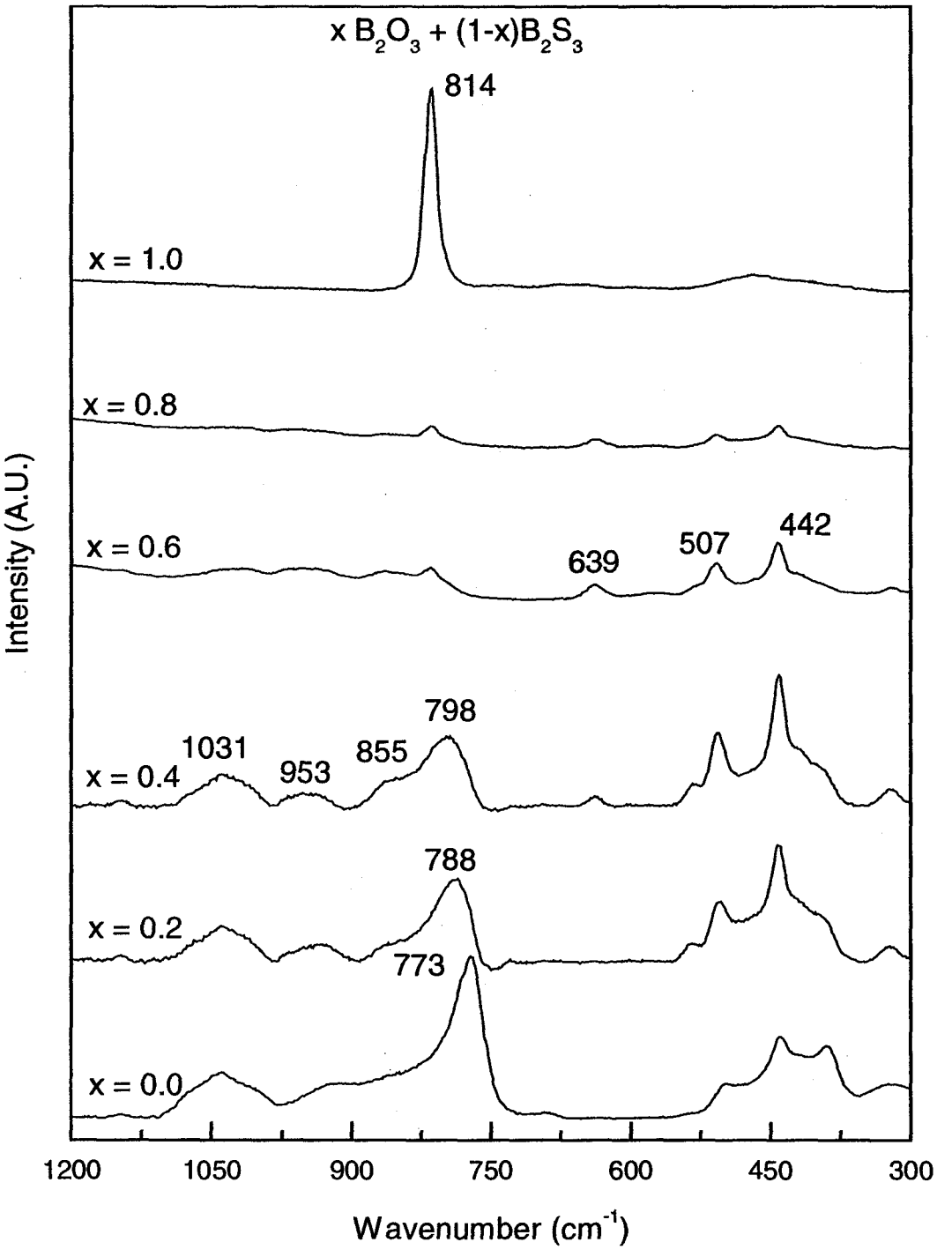

Figure 2.1 Raman spectroscopy of the xB_2O_3 + (1-x)B_2S_3 glasses. The bottom trace is pure B_2S_3 and the top trace is pure B_2O_3.

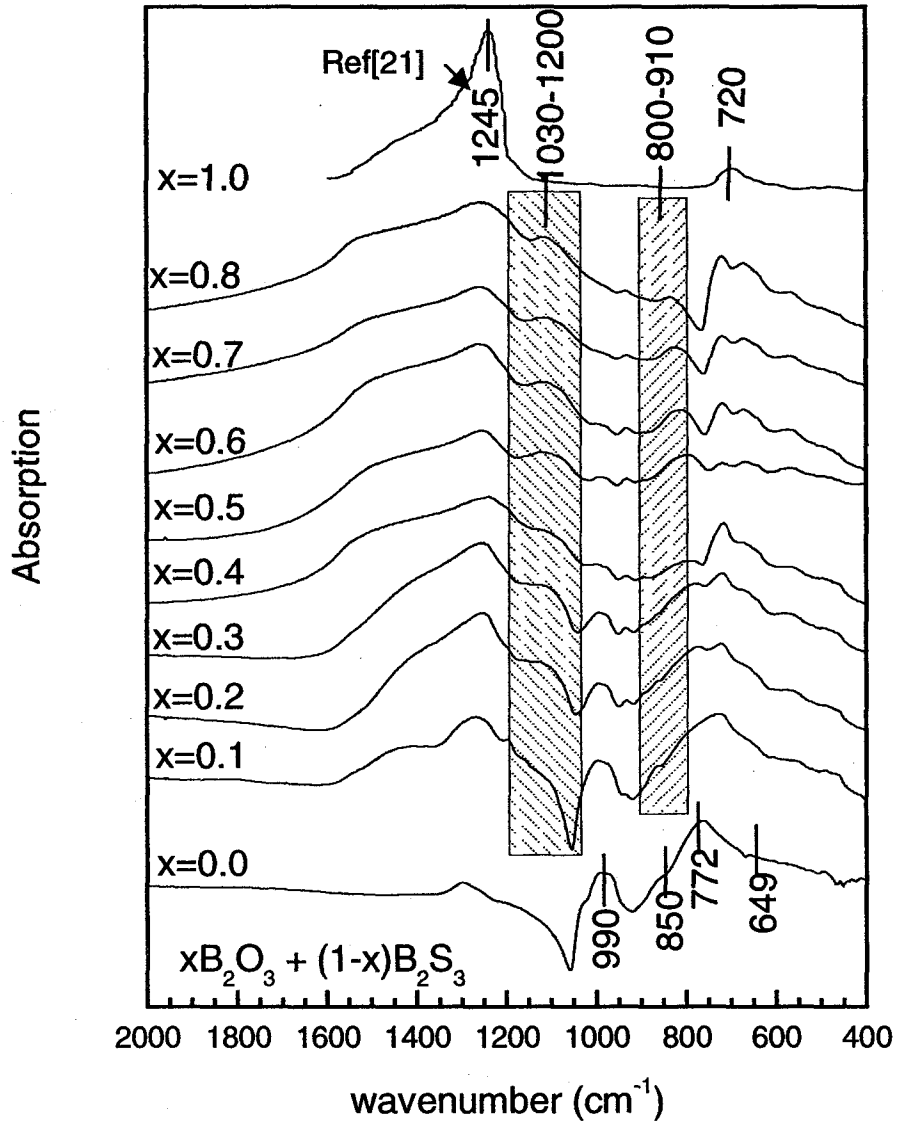

Figure 2.2 IR spectra of $xB_2O_3 + (1-x)B_2S_3$ glasses.

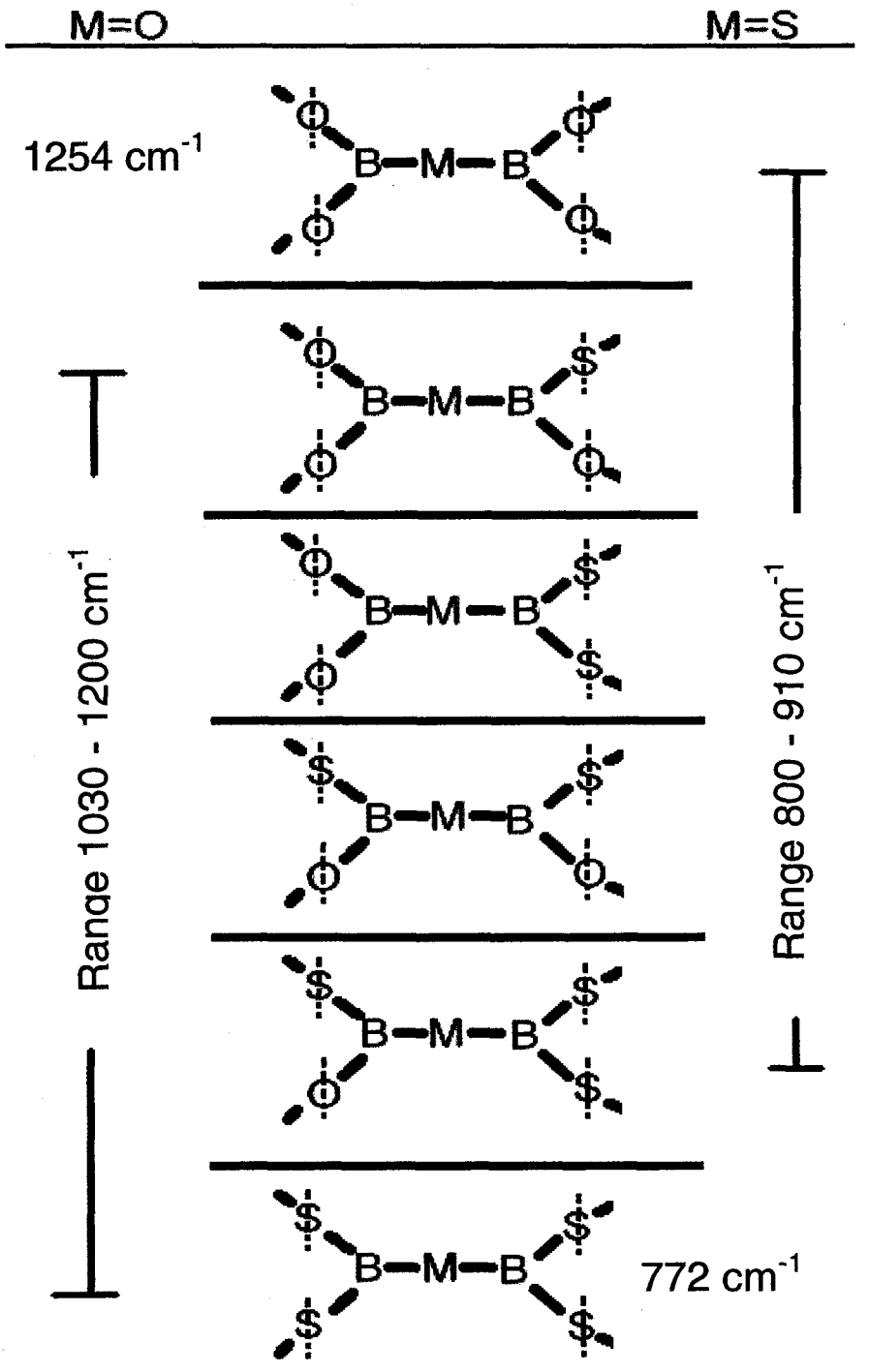

Figure 2.3 The structural units used to perform an elementary calculation of IR absorbance peak positions.

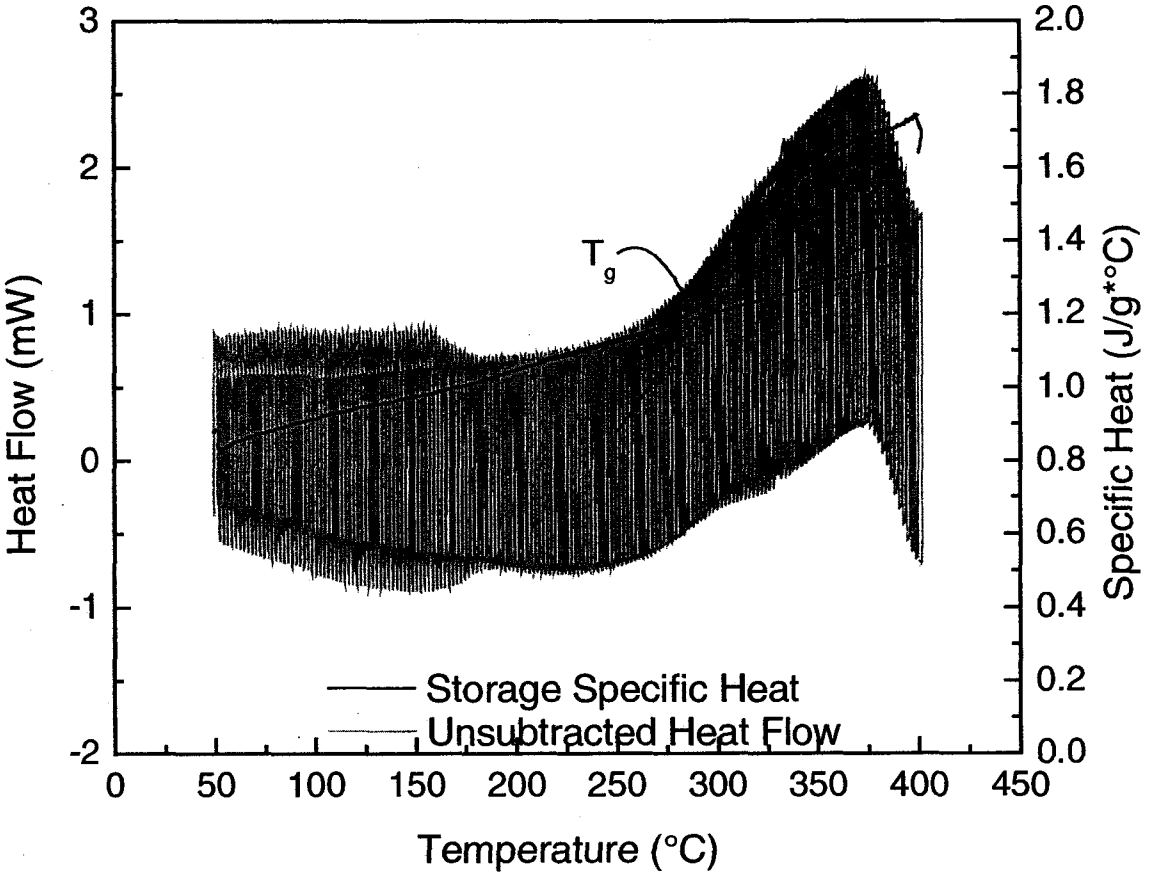

Figure 2.4 Example of a DDSC scan on the 0.35 B_2O_3 + 0.65 B_2S_3 glass. This data supports the conclusion that the sample is not phase separated because only one glass transition temperature can be seen.

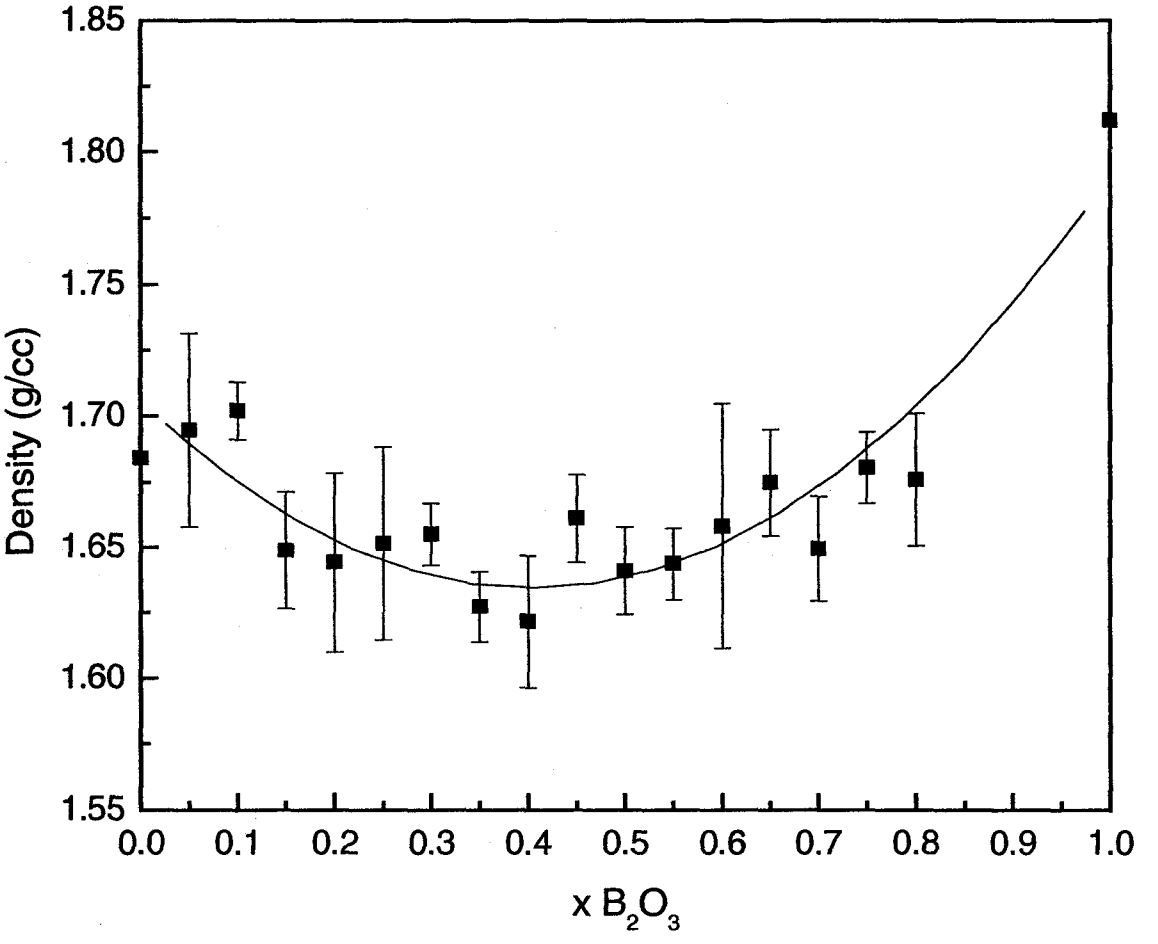

Figure 2.5 Density measurements for the $xB_2O_3 + (1-x)B_2S_3$ glasses.

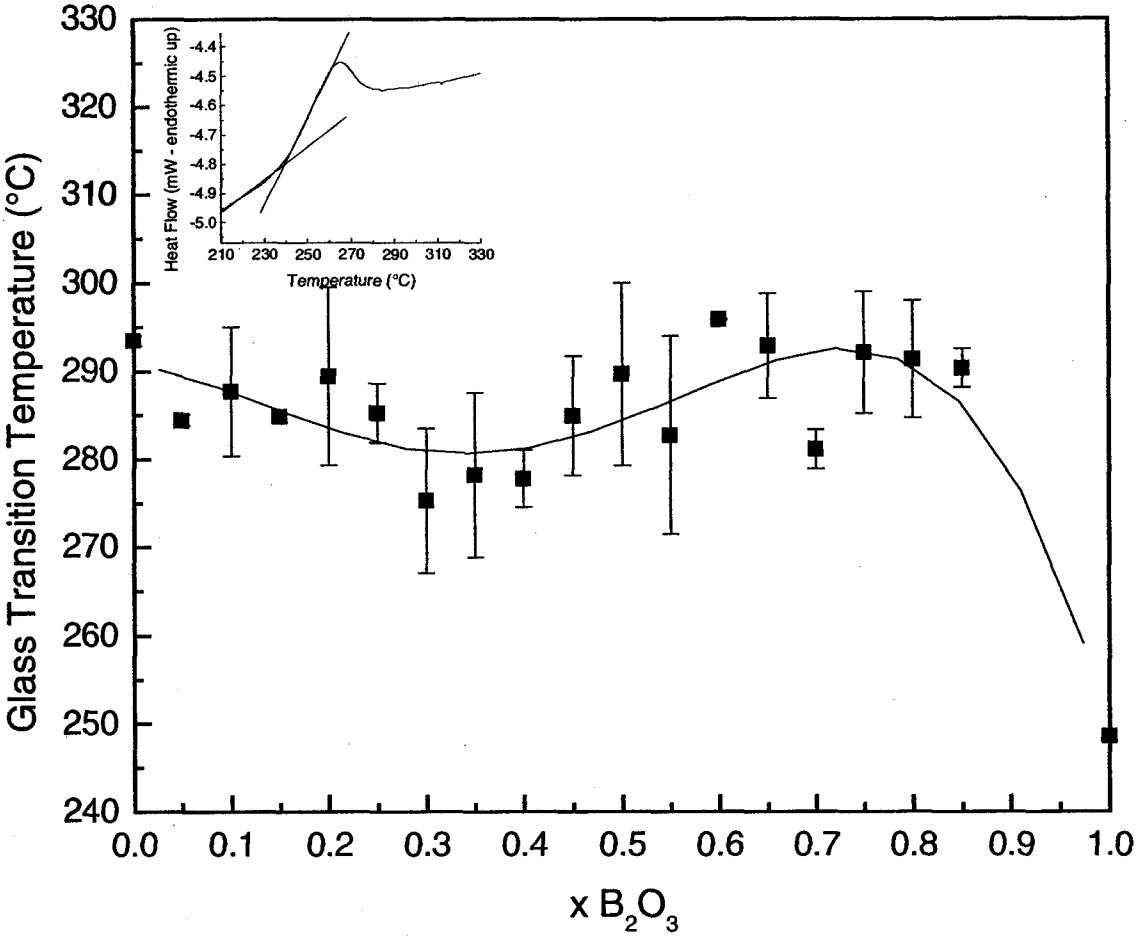

Figure 2.6 Glass transition data for the $xB_2O_3 + (1-x)B_2S_3$ glasses.

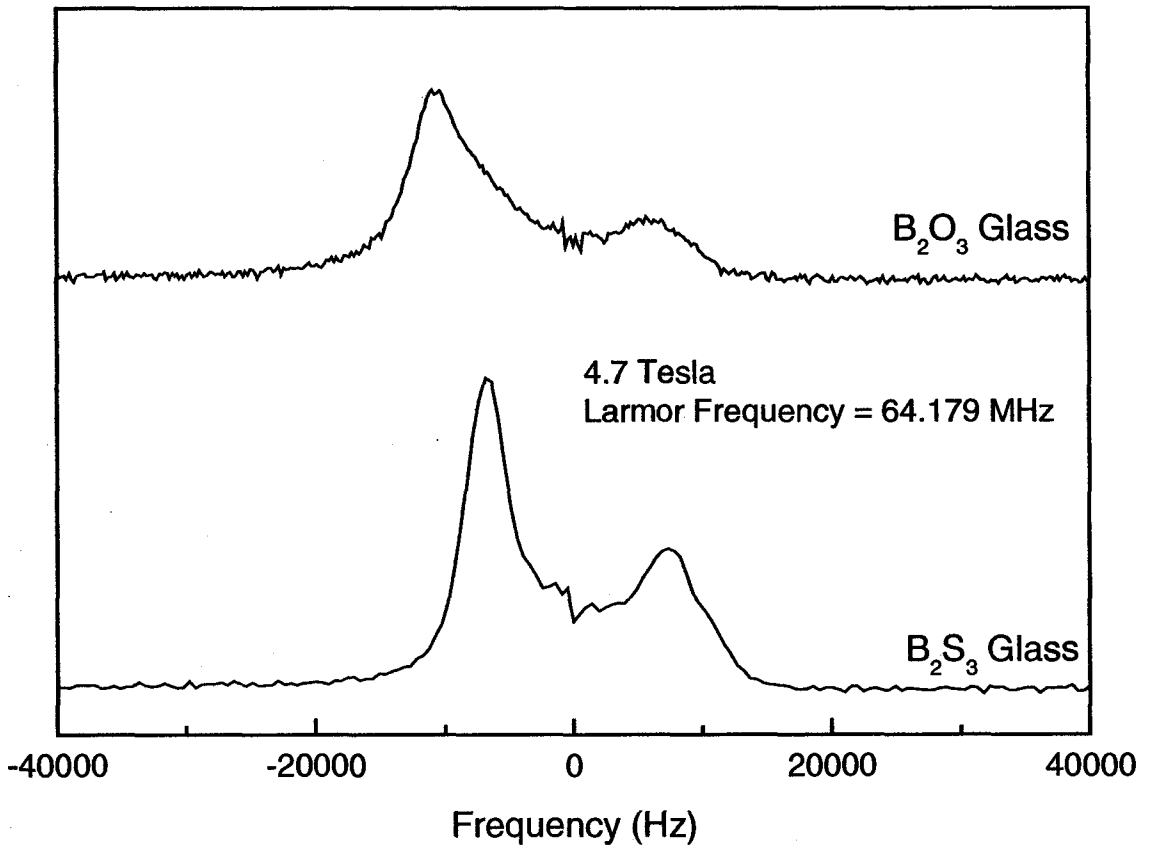

Figure 2.7 ^{11}B NMR static spectra at 4.7 Tesla of pure glassy B_2O_3 and pure glassy B_2S_3.

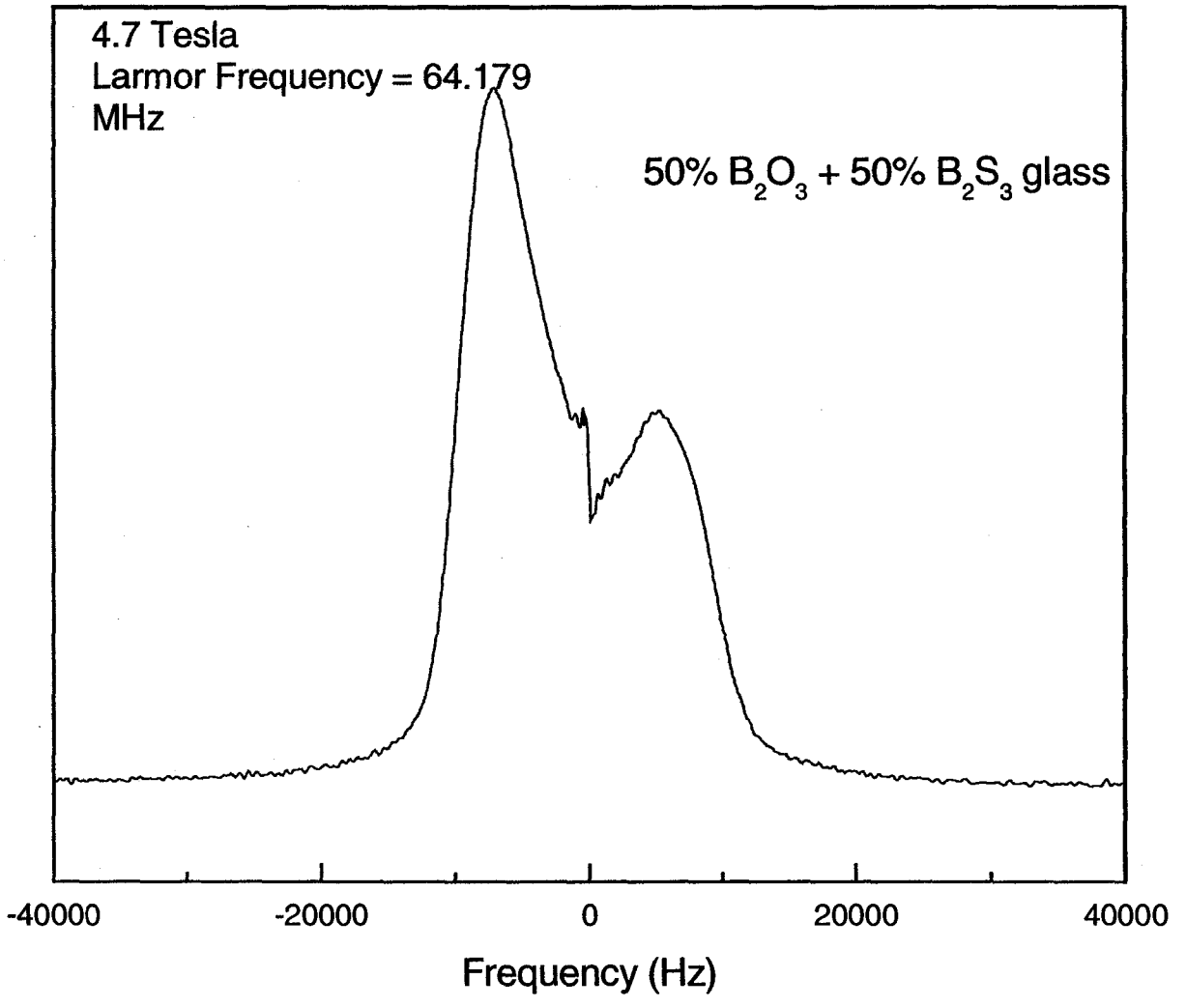

Figure 2.8 ^{11}B NMR static spectra at 4.7 Tesla of $.50B_2O_3 + .50B_2S_3$ glass.

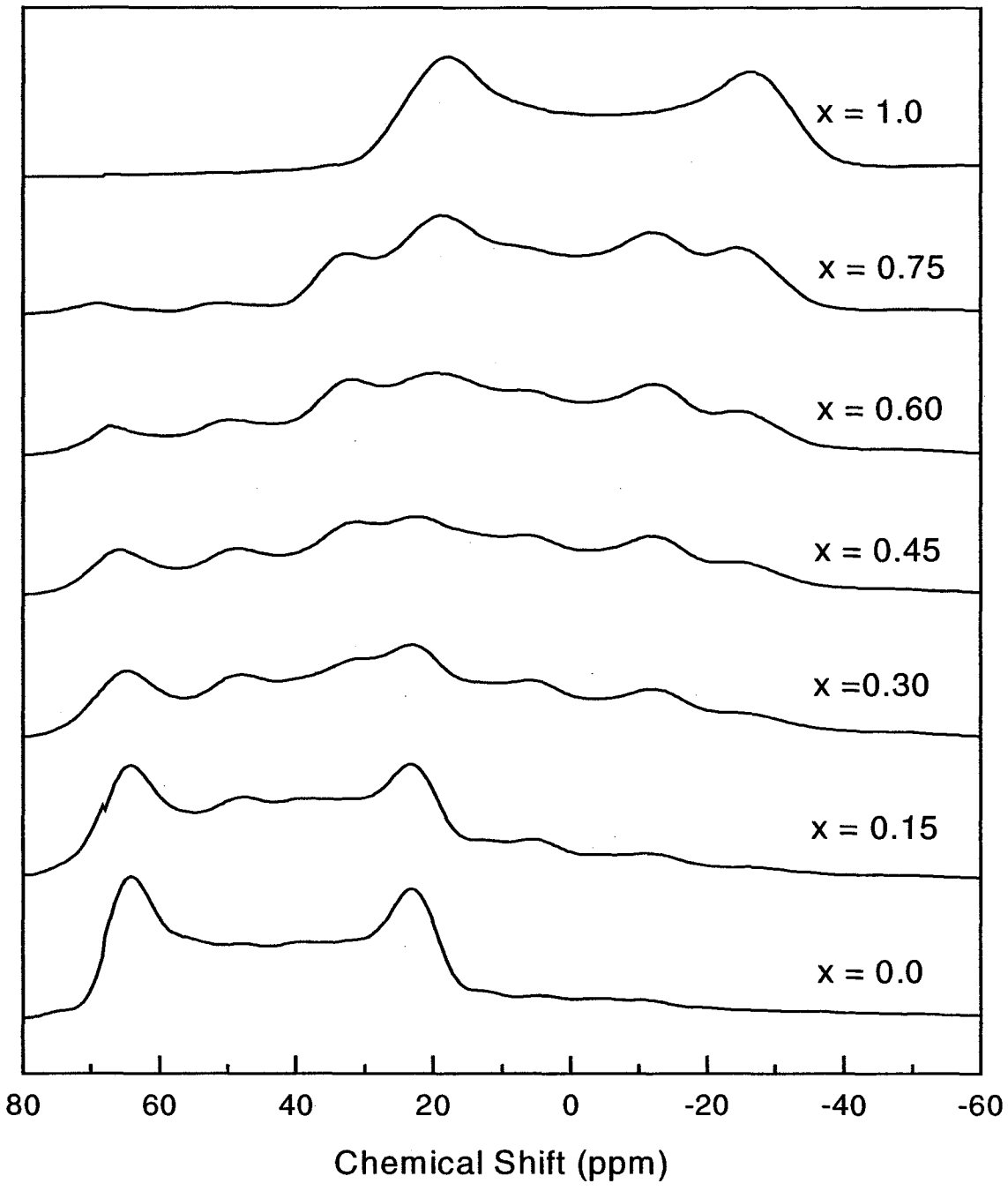

Figure 2.9 ^{11}B MAS NMR at 4.7 Tesla of x B_2O_3 + (1-x) B_2S_3 glasses.

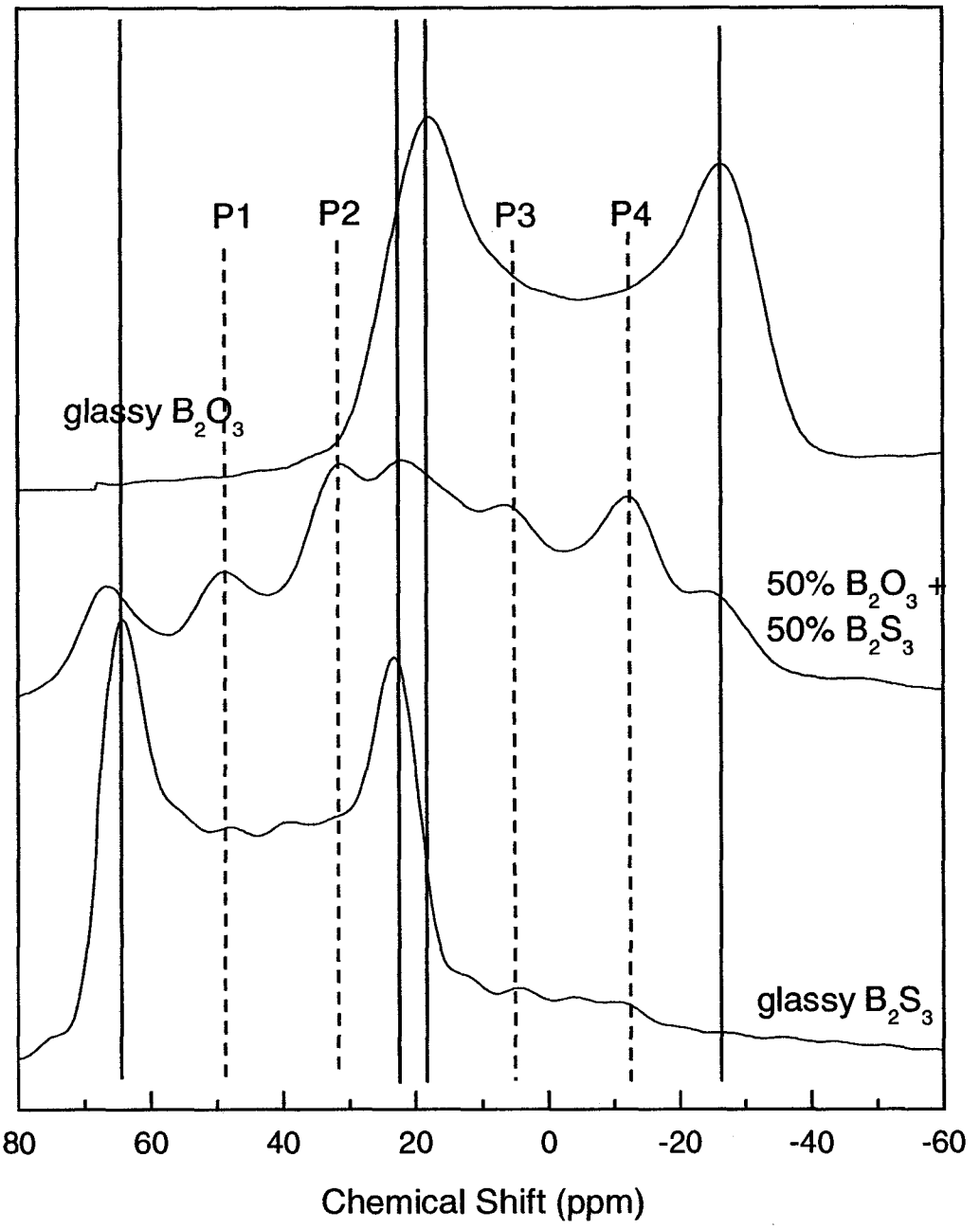

Figure 2.10 ^{11}B MAS NMR spectra showing the presence of four new peaks, P1 – P4.

CHAPTER 3 STRUCTURE AND PROPERTIES OF LITHIUM THIO-BORO-GERMANATE GLASSES

By

B. Meyer[a,b,c], S. W. Martin[b,d], F. Borsa[c]

A paper to be submitted to the Journal of Non-Crystalline Solids, May 2003

[a] Primary researcher and author
[b] Department of Materials Science & Engineering, Iowa State University, Ames, IA 50011
[c] Ames Laboratory – U.S. Department of Energy, Iowa State University, Ames, IA 50011
[d] Author to whom correspondence should be directed

3.1 Abstract

Structural studies of the ternary $xLi_2S + (1-x)[0.5\ B_2S_3 + 0.5\ GeS_2]$ glasses using IR, Raman, and ^{11}B NMR show that these glasses do not have equal sharing of the lithium atoms between GeS_2 and B_2S_3. The IR spectra indicates that the B_2S_3 glass network are under-doped in comparison to corresponding compositions in the $xLi_2S + (1-x)B_2S_3$ binary system. Additionally, the Raman spectra show that the GeS_2 glass network is over-modified. ^{11}Boron static NMR gives evidence that ~80% of the boron atoms are in tetrahedral coordinated. A super macro tetrahedron is proposed as one of the structures in these glasses in which some of them may contain boron sites substituted by germanium atoms at lower Li_2S content.

3.2 Introduction

An important part of the full study of $Li_2S + B_2S_3 + GeS_2$ ternary FIC glasses is to determine their atomic level structures and physical properties. By comparing results with binary glasses such as $Li_2S + B_2S_3$ and $Li_2S + GeS_2$ and other similar ternary glasses, conclusions about the structure can be drawn. Glasses in the $zLiI + (1-z)[xLi_2S + (1-x)(0.5\ B_2S_3 + 0.5\ GeS_2)]$ system, where x = 0.35, 0.45, and 0.55, have been prepared. In the x = 0.55 glasses, samples were doped with LiI for z = 0.0, 0.1, 0.2, and 0.3 in an effort to increase the conductivity and to determine if a non-Arrhenius behavior is present as in the case of silver thio-boro-silicates enhanced with addition of AgI.[1] The reader is referred to the conductivity and ^{7}Li NMR measurements of these lithium glasses reported in another study by the

authors.[2] DSC measurements showed that the glass transition temperature decreases with added Li_2S and LiI. IR and Raman spectroscopies were used to identify structures that showed qualitative evidence that the lithium ions prefer germanium sites over boron sites. ^{11}B and ^{7}Li static NMR measurements also show quantitative agreement for the sharing of lithium ions.

3.3 Experimental Methods

The glass compositions prepared for this study were made by reacting stoiciometric amounts of LiI (Aldrich 99% purity), Li_2S (Cerac 99.9% purity), GeS_2, and B_2S_3. Both GeS_2 and B_2S_3 were prepared by mixing and reacting germanium metal with sulfur (99.999% purity) and amorphous boron metal with sulfur, respectively.[3] Each sample was mixed and melted in a vitreous carbon crucible at 850 °C for 10 minutes. Weight loss after the first melt was recorded (always less than 5%), and then the samples were reheated for an additional 5 minutes. The molten samples were then quenched onto graphite molds held at 200°C and annealed for 30 minutes. Afterwards, the samples were cooled to room temperature at a rate of 5 °C/min. All of the samples were transparent with a reddish orange or yellowish orange color when having a thickness of approximately three millimeters.

Figure 3.1 shows the glass forming range for this system. Good glasses were formed on the 1:1 and 2:1 B_2S_3 to GeS_2 tie lines where $0.35 \leq x \leq 55$ and $0.45 \leq x \leq 0.65$, respectively. The glass forming compositions in the $Li_2S + B_2S_3$ and $Li_2S + GeS_2$ binary systems are reported from the work of Cho[4] and Souquet[5], respectively.

Glass forming data for the B_2S_3 + GeS_2 binary system is reported by Mei and Martin.[6]

3.3.1 DSC Measurements

Glass transition, crystallization, and melting temperatures were measured using a Perkin-Elmer Pryis 1 Differential Scanning Calorimeter. Approximately 10 mg. of each sample was loaded into an aluminum pan and hermetically sealed. The samples were heated at a rate of 10 °C/min from 50 °C to 500 °C. The DSC measurements were used to determine Tg in order to establish an upper limit of temperature to perform the Nuclear Spin-Lattice Relaxation (NSLR) and conductivity measurements. This was done to determine an upper temperature limit to avoid any structural relaxations and/or crystallization due to the glass-liquid transition.

3.3.2 Density Measurements

The densities of the samples were measured by using Archimedes's principle.[7] The dry mass of the sample was first recorded, and then the mass of the sample was taken submersed in liquid kerosene. The density was then calculated from Eq. (4-1). Each composition was measured individually four times using different pieces from the same sample. The density values were found by averaging the four measurements taken for each composition. The error bars were estimated by including the largest and smallest values measured. The value for the density of kerosene was independently measured to be 0.82 g/cc $\pm$ 0.01 g/cc.

$$\rho_{sample} = \frac{\rho_{keosene} m_{dry}}{m_{dry} - m_{submersed}} \qquad (4\text{-}1)$$

3.3.3 Raman Spectroscopy

The Raman spectra were taken using a Brűker FT-Raman Spectrometer. The excitation source was a Nd:Yag laser operating at 1064 nm. The Raman spectral range was 120 to 3600 cm^{-1} Stokes shifted. The measurements were performed using ~100 mW power in a 180° backscatter experiment with a laser beam diameter of ~0.1 mm. Samples were prepared by crushing into powder and compacting the powder into a special holder cavity with a diameter of 2.2 mm.

3.3.4 IR Spectroscopy

The IR spectra were obtained using a Bio-Rad FTS-40 FT-IR spectrometer using KBr pellets. The spectral range was 4400 to 450 cm^{-1} with a resolution of 0.5 cm^{-1}. KBr Pellets were prepared by mixing potassium bromide and the glass sample in a mass ratio of 10:1.

3.3.5 Boron Static NMR Spectroscopy

^{11}B static NMR measurements were performed at 64.179 MHz (4.7 Tesla) at room temperature. A $\pi/8$ pulse length was used to avoid excitation of non-central line transitions since boron has a spin of 3/2. Data was acquired immediately from the FID, and 500 scans were averaged for each sample. A delay of 5 seconds between each scan was used.

3.4 Results

3.4.1 Glass Forming Range

Glasses were prepared in the x = 0.35 to 0.55 region in the 1:1 B_2S_3:GeS_2 tie line, and also in the region of x = 0.45 to x = 0.65 of the 2:1 B_2S_2:GeS_2 tie line. Above and below these compositions, it was found that the samples crystallized using the method of quenching into a vitreous carbon mold at 200 °C as described above. Figure 3.1 shows the glass forming range based on the measurements in this study and previous work by other various groups.[4,5,6] It appears that the predominate glass forming range occurs in the window existing from the $xLi_2S + (1-x)B_2S_3$ binary line (where $0.45 \leq x \leq 0.75$) to the center of the of the ternary system. For the x = 0.55 and ratio of B_2S_3:GeS_2 is 1, the samples were doped with 10, 20, and 30 mol percent LiI.

3.4.2 Density Measurements

The densities of these glasses shown in Table 3-2 were found to be approximately 2.2 g/cc for the x = 0.35, 0.45, and 0.55 samples. This compares to values of 2.480 g/cc for the $0.45\ Li_2S + 0.55\ GeS_2$ glass composition[8] and 1.800 g/cc for the $0.65\ Li_2S + 0.35\ B_2S_3$ glass composition.[9] With increasing amounts of LiI, the density increases systematically from 2.20 g/cc to 2.59 g/cc, which is expected since the density of LiI is 4.06 g/cc.[10]

3.4.3 IR spectra of the Glasses

In the IR spectra, Figure 3.2 and Figure 3.3, there are four main peaks that appear. The following peak assignments are based on a study by Cho.[4] The 738 and 674 cm^{-1} doublet is assigned to the boron sites in tetrahedral coordination. The other two peaks at 890 and 808 cm^{-1} are associated with boron sites in trigonal coordination. The 890 cm^{-1} peak arises from trigonal boron in six-member rings. Isolated trigonal boron sites give rise to the peak at 808 cm^{-1} in the x = 0.55 sample. All of the spectra in this study closely resemble the spectra of the x = 0.48 glass in the binary system. With added Li_2S, Cho[4] (Figure 3.4) showed that the peak at 890 cm^{-1} diminishes as the peak at 808 cm^{-1} grows stronger. Studies have shown that ~75% boron atoms in pure B_2S_3 are incorporated into six-member ring structures, and the remaining 25% are contained in loose trigonal units.[11] As alkali sulfide content is increased, the six-member rings are destroyed at the expense of creating new loose trigonal units.[12] The x = 0.55 glass in the ternary system contains a much higher fraction of six-member rings compared to x = 0.55 glass composition in the binary system. As Li_2S concentration is increased, the width of the peaks narrow.

The low intensity bands in the range of 1,000 to 1,500 cm^{-1} are probably due to sites associated with oxygen contamination.[13,14] Cho et al.[4,15] showed in the binary $Li_2S + B_2S_3$ glasses through chemical analysis that bands of similar intensity in the 1,000 – 1,500 cm^{-1} range constituted less than 1 wt. % of the sample and for this were ignored. The addition of LiI to the x = 0.55 Li_2S sample some narrowing of the peaks occur, but otherwise it does not appear to significantly alter the structural features seen in the IR spectra.

3.4.4 Raman spectra of the Glasses

The spectra of the $Li_2S + GeS_2$ binary glasses by Souquet et al.[5], Figure 3.7, shows two peaks at 350 cm^{-1} and 425 cm^{-1}. These peaks are assigned to Ge-S-Ge bridge bonds and Ge with one non-bridging sulfur, respectively. The spectra, Figure 3.5, of the ternary $Li_2S + B_2S_3 + GeS_2$ glasses (Figure 3.5) show the presence of two additional peaks at 378 and 407 cm^{-1}. It is suggested that the peak at 407 cm^{-1} is associated with Ge with two non-bridging sulfurs, and the peak at 378 cm^{-1} is assigned to a germanium tetrahedral with three non-bridging sulfurs. Table 3-3 shows peak assignments from this study compared to a study by Kamitsos et al.[16] on silver thiogermanate glasses using Raman and Far-IR spectroscopies, in which they elucidated the different germanium sites, and to a silmilar study by Barrau[29] on sodium thio-germanates. The two peaks at 378 and 407 cm^{-1} increase in intensity at the expense of the peaks at 345 and 425 cm^{-1}. The growth of the peaks at 378 and 407 cm^{-1} are assigned to the creation of germaniums with 2 and 3 non-bridging sulfurs, respectively. Due to the relative inefficient Raman scattering of B_2S_3 compared to GeS_2 when using a 1064 nm^{-1} laser source, small peaks at the 500, 700-770, and 812 cm^{-1} representing the different sulfur atom stretches in alkali sulfide modified B_2S_3 glasses were detected. The intensity of these peaks were just outside of experimental noise, but do suggest confirmation of the presence of tetrahedral boron atoms (700-770 cm^{-1}), B_2S_3 six-member rings (500 cm^{-1}), and sulfur stretches in B_2S_3 trigonal units (812 cm^{-1}) as clearly shown in the IR spectra.[12,17] Similar to the IR spectra, the addition of LiI did not appear to alter the Raman spectra, Figure 3.6, significantly when added to the x=0.55 sample.

3.4.5 Boron Static NMR Spectra of the Glasses

Due to the quadrupolar nature of boron, it is possible to determine the fraction of boron atoms in trigonal and tetrahedral coordinations using NMR spectroscopy.[18,19] Due to the asymmetry in the electric field gradient of the trigonal boron environment, the energy required to induce a magnetic transition is different for a boron nucleus lying in the plane of the trigonal boron group and a nucleus aligned perpendicular to this plane. This results in a splitting of the energy levels giving rise to two peaks. The electric field gradient of the tetrahedral boron environment is spherically symmetric, and therefore no splitting of the peak is seen for the transition energy regardless of nucleus alignment. Estimating the fractional area of the tetrahedral boron peak yields that for all of the samples in the ternary $Li_2S + B_2S_3 + GeS_2$ system, ~70-80% of the boron atoms are in tetrahedral coordination (Figure 3.8). The additional of LiI did not change the fraction of tetrahedral boron atoms; the fraction remain constant at 80% as in the $x = 0.55$ Li_2S ternary glass composition.

3.5 Discussion

The appearance of the new peaks at 378 cm^{-1} and 407 cm^{-1} in the Raman spectra (Figure 3.5) suggest that the addition of Li_2S creates germanium sites with two and three non-bridging sulfurs. In comparison to the binary compositions, this would indicate that the lithium ions favor the germanium sites resulting in unequal sharing. If the sharing between B_2S_3 and GeS_2 was 1:1, it would be expected for both the IR and Raman spectra to be similar for similar levels of modification to the

corresponding spectra of the binary glasses. However, it has been seen that the Raman spectra shows that the germanium sites have more terminal sulfur bonds than the binary glasses and this suggests that these sites contain more lithium than the corresponding composition in the binary system. Similarly, the IR spectra (Figure 3.2) suggest that the boron sites have less lithium than in the corresponding $Li_2S + B_2S_3$ binary system. It is not possible to obtain a quantitative estimate of the fraction of the lithium ions shared between the germanium and boron sites from the IR and the Raman spectra alone. However, this can be obtained from the ^{11}B spectra.

The ^{11}B NMR spectra (Figure 3.8), show that for all of the compositions, approximately ~70-80% of the boron are in tetrahedral coordination. If it is assumed that for every tetrahedral boron atom there is one corresponding lithium ion, it would appear that the sharing of lithium ions would prefer boron over germanium atoms since the ratio of boron to germanium atoms is 2:1. However, any preference of sharing of lithium ions to boron would contradict the qualitative evidence given by the IR and Raman spectra for these.

Studies of the fraction of tetrahedral boron atoms in both the oxide and sulfide boron glasses have been extensively carried out.[18,20,21,22] It has been found that for all of the oxide glasses, irregardless of the added alkali, two boron atoms are converted from trigonal to tetrahedral for every added M_2O, where M is Li, Na, K, Rb, or Cs. However, the formation rate of tetrahedral boron atoms is strongly alkali dependent in the sulfide glasses as seen in Figure 3.9. For Cs, the conversion rate, 1, is the same as in the oxide case. The conversion rate for every added alkali ion

then increases to 1.25 for Rb, 1.5 to 2 for K, and 3 to 4 for Na. Following this trend, it seems possible from this data that the conversion rate could be 4 or more boron atoms converted for every added lithium ion. This would make it possible to have a sharing ratio which prefers germanium over boron, yet at the same time creates a large amount of tetrahedral boron in the system. The following paragraph works through a calculation giving an estimate of the number of lithium ions needed to convert 80% of the boron to tetrahedral coordination for one mole of the x = 0.35 sample.

Given one mole of the 0.35 Li_2S + 0.65 (0.5 B_2S_3 + 0.5 GeS_2) glass, 0.70 moles of lithium atoms and 0.65 moles of boron atoms are present. If a lithium ion was needed for every boron atom that was converted from trigonal to tetrahedral coordination (~80%), this would require 0.52 moles of lithium atoms. However, the alkali dependence of the N_4 formationn in the alkali sulfides suggest that only 1 lithium ion is needed to covert every 4 boron atoms to tetrahedral coordination. This higher conversion efficiency would only require 0.13 moles of lithium ions. This calculation estimates that 0.065 moles of the 0.35 total moles of Li_2S go to the B_2S_3 network while the remaining 0.285 moles of Li_2S are incorporated into the GeS_2 network.

The above calculation does not consider the possibility of Li_2S forming trigonal boron atoms with one or more non-bridging sulfur atoms. Table 3-4 shows the calculated compositions for the other samples assuming that an extra 5% lithium sulfide is shared to the boron helping to create trigonal boron atoms with a non-bridging sulfur. The purpose of Table 3-4 is to illustrate that for all of the

compositions prepared, there is sufficient lithium ions present to both convert 70 to 80% of the boron atoms to tetrahedral coordination and simultaneously heavily modify the GeS_2 glass network. This arises because of the anomalously high conversion rate of tetrahedral boron in the lithium thioborate glasses. It is noted that such a high conversion rate requires sulfur to be in threefold coordination. Studies of such threefold coordination are in progress.

Figure 3.9 shows the compositional dependence of the N_4 fraction versus composition for various M_2S alkali glasses. In all of the systems, there is a significant increase in N_4 with added alkali sulfide. Though, the maximum in the curve is strongly alkali dependent, by x=0.45 in all systems, there is a significant decrease in the number of tetrahedral boron atoms. In the N_4 data for the ternary glasses, Figure 3.8 , there is no significant change in the number of tetrahedral boron atoms with varying amounts of added Li_2S. Comparing this to the case of the binary $Li_2S + B_2S_3$ glasses, it would be expected at x = 0.45, N_4 would have dropped to at least 35% due to the further conversion of tetrahedral boron atoms into trigonal boron atoms with non-bridging sulfur atoms. Yet, the fraction of tetrahedral boron in the ternary glasses remains high at 80%. Also in the binary glasses, i.e. the x=0.55 composition, the peak in the IR spectra at 890 cm^{-1}, six-member rings, is no longer well resolved. This shows that the six-member ring structures that are present are now broken apart by the added Li_2S, which does not appear to be the case in the lithium ternary glasses for these compositions. This may suggest that the thioborate network of the ternary glass has a structure similar to that of the glasses in the range

of x = 0.15 to x = 0.30 Li_2S region in the binary glasses; again reflecting that the lithium atoms have a preference toward the germanium atoms.

One structural arrangement that may account for the high number of tetrahedral boron atoms in these glasses was introduced by Hebel et al.[23] and is shown in Figure 3.10. This study described the preparation and crystal structure of the $Li_{6+2x}[B_{10}S_{18}]S_x$ (where x~2) phase. The proposed structure is that of a macro-tetrahedral $B_{10}S_{20}$ fragment of a polymeric $[B_{10}S_{16}S_{4/2}]^{6-}$ unit. All of the boron in this particular fragment are tetrahedral and four of the twenty sulfurs are in three-fold coordination. At the same time, all of the tetrahedral boron atoms are also in six-member rings. This could explain the strong band intensities for both tetrahedral boron and boron in six member rings in the IR spectra. A good technique used to confirm the presence of three-fold coordinated sulfur would be extended x-ray absorption fine structure (EXAFS).[24] It is possible to obtain an average coordination number for a probed atom in conjunction with a partial radial distribution function using this technique. Sulfur is a common atom studied by EXAFS. Another powerful instrument to use would be NMR. However, with a natural abundance of 0.76% and a spin I = 3/2, ^{33}S NMR is very difficult to measure due to a very large quadrupolar broadening.[25] In some instances, the chemical shifts can be larger than 1000 ppm and the lines widths can be greater than 5000 Hz.[26] Though as more techniques are currently being developed with increasingly more powerful magnetic fields, ^{33}S NMR experiments should be readdressed.[27,28]

It has been shown that $Na_2S + GeS_2$ glasses at the sodium dithioborate composition have a similar structure to a B_4S_{10} substructure present in the $B_{10}S_{20}$

macroanion.[29] The germanium tetrahedron are connected in a way that also forms six member rings as shown in Figure 3.12. If the sharing of the lithium atoms were close to 1 to 1, it would be expected that a significant fraction of the germanium atoms may be incorporated into a $Ge_4S_{10}^{4-}$ structure. This structure should give peak intensities at ~193,144, and 116 cm^{-1}.[30,31] From the Raman spectra it seems that some $Ge_4S_{10}^{4-}$ groups exists in these compositions represented by a medium intensity broad peak centered around ~175 cm^{-1}. However, due to the large amount of lithium atoms associated with germanium sites, this structure is probably present in only a small amount. It is conceivable that a fraction of germanium atoms with four bridging sulfurs may be able to occupy boron positions within these supermacro tetrahedrons. Figure 3.11 shows a possible structure that may be present in the glasses. Due to the larger size of the germanium atom and the longer bond length of Ge-S, this would distort the six-member rings where boron atoms are also present. The addition of Li_2S would also create non-bridging sulfur atoms associated with the germanium sites, and in turn it would be no longer favorable to have germanium with terminal sulfur bonds incorporated into the super macro tetrahedron. As less germanium is incorporated into the super tetrahedron structure, less strain and distortion occurs, thus narrowing the tetrahedral peaks in the IR.

The remaining trigonal boron and tetrahedral Germanium with terminal sulfurs create a network which links the super macro tetrahedron at their corners. The structure of the remaining germanium would be expected to be very similar to the $Na_6Ge_2S_7$ and $Na2Ge_2S_3$ structural units described in the study by Barrau.[29] Barrau found that intermediate composition ranges yielded spectra reflecting the sum of the

different structures present. Another difference in the ternary glass compositions would be that the sulfur atoms should also bridge boron and germanium structural units together.

3.6 Conclusions

It has been shown that the structure of the ternary $xLi_2S + (1-x)[0.5\ B_2S_3 + 0.5\ GeS_2]$ glasses do not have equal sharing of the lithium atoms between GeS_2 and B_2S_3. The IR spectra indicates that the B_2S_3 glass network are under-doped in comparison to corresponding compositions in the $xLi_2S + (1-x)B_2S_3$ binary system. The Raman spectra show that the GeS_2 glass network is over-modified in comparison to the binary $xLi_2S + (1-x)GeS_2$ binary glass system. ^{11}Boron static NMR gives evidence that ~80% of the boron atoms are in tetrahedral coordinated. A super macro tetrahedron is proposed as one of the structures in these glasses in which some of them may contain boron sites substituted by germanium atoms at lower Li_2S content. The super macro tetrahedrons are then connected by trigonal boron and tetrahedral germanium heavily modified with Li_2S that make up the rest of the glass network.

Table 3-1 Weight loss measurements for the various compositions upon heating.

Sample	Before heating(g)	After heating (g)	% loss
x = 0.35	2.964 ± 0.002	2.824 ± 0.002	4.7
x = 0.45	2.99 ± 0.002	2.908 ± 0.002	2.7
x = 0.55, z = 0.0	2.991 ± 0.002	2.923 ± 0.002	2.2
x = 0.55, z = 0.1	1.99 ± 0.002	1.915 ± 0.002	3.8
x = 0.55, z = 0.2	1.993 ± 0.002	1.911 ± 0.002	4.1
x = 0.55, z = 0.3	2.687 ± 0.002	2.608 ± 0.002	2.9

Table 3-2 Density for ternary samples in zLiI + (1-z)[xLi_2S + (1-x)(0.5B_2S_3+0.5GeS_2)] glasses.

Sample	Density (g/cc)
X=0.35	2.19 ± 0.06
X=0.45	2.23 ± 0.06
Z=0.0, X=0.55	2.20 ± 0.06
Z=0.1, x=0.55	2.28 ± 0.06
Z=0.2, x=0.55	2.37 ± 0.06
Z=0.3, x=0.55	2.59 ± 0.06

Table 3-3 Raman peak assignments for alkali modified thio-germanates.

Assignment M = Li, Na, or Ag	Lithium thio-boro-germanate glasses(cm^{-1})	Sodium thio-germanate glasses(cm^{-1})[29]	Silver thio-germanate glasses(cm^{-1})[16]
$GeS_{4/2}$	350 (350 ref[5])	345	345
$MSGeS_{3/2}$	378	390	370
$M_2S_2GeS_{2/2}$	407	419	400
$M_3S_3GeS_{1/2}$	428 (425 ref[5])	469	420

Table 3-4 Calculated "equivalent binary" compositions present in the $xLi_2S + (1-x)[0.5\ B_2S_3 + 0.5\ GeS_2]$ ternary glasses.

Sample	Thio-borate binary composition	Fraction of Li shared to B	Thio-germanate binary composition	Fraction of Li shared to Ge
x = 0.35	0.202 Li_2S + 0.798 B_2S_3	24%	0.451 Li_2S + 0.549 GeS_2	76%
x = 0.45	0.220 Li_2S + 0.780 B_2S_3	17%	0.575 Li_2S + 0.425 GeS_2	83%
x = 0.55	0.244 Li_2S + 0.756 B_2S_3	13%	0.680 Li_2S + 0.320 GeS_2	87%

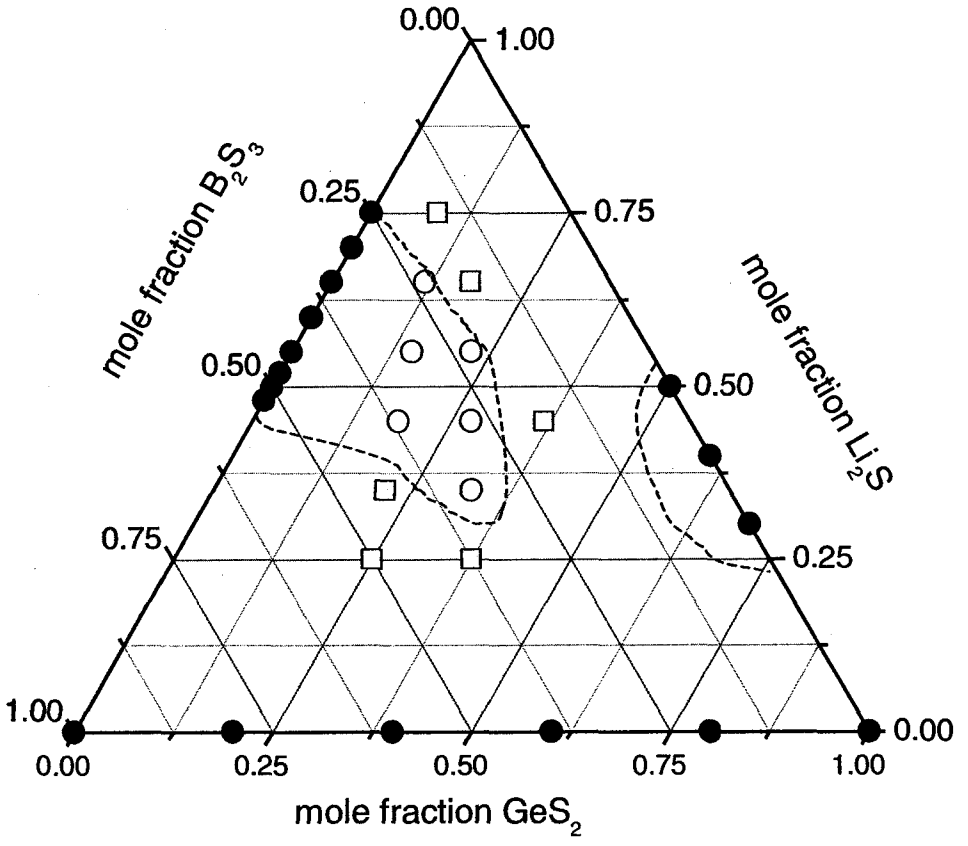

Figure 3.1 Glass forming range of $Li_2S + B_2S_3 + GeS_2$ glasses. (○) Glass samples prepared in this study. (□) Samples prepared in this study that crystallized and/or phase separated. (●) Other reported glass forming compositions.[4,5,6]

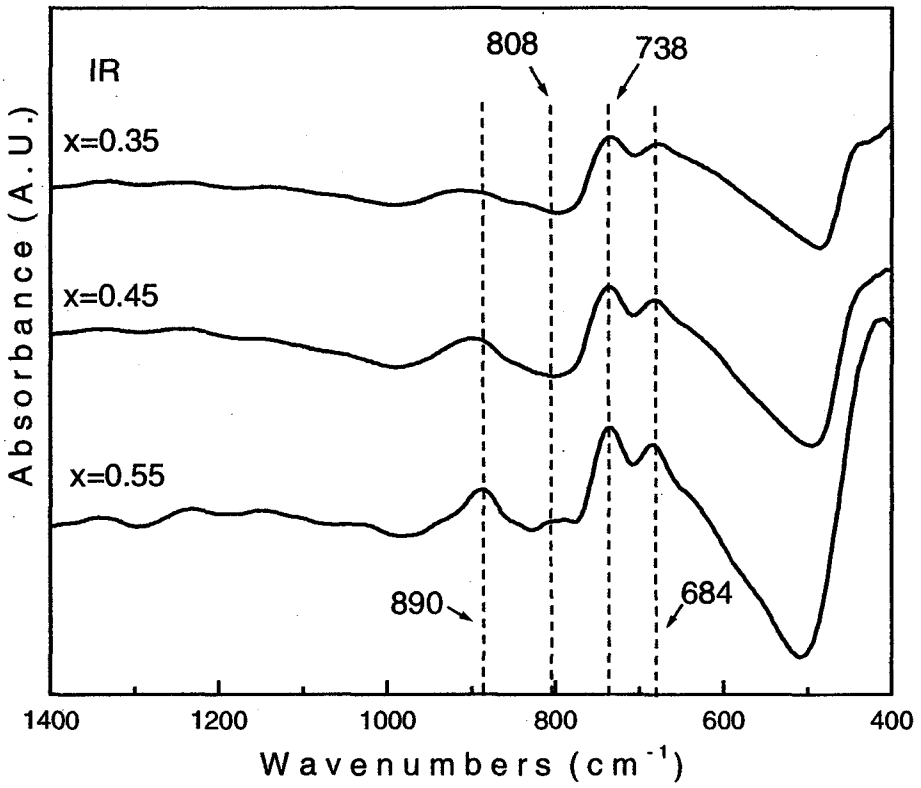

Figure 3.2 IR spectra of $xLi_2S + (1-x)[0.5\ B_2S_3 + 0.5\ GeS_2]$ glasses.

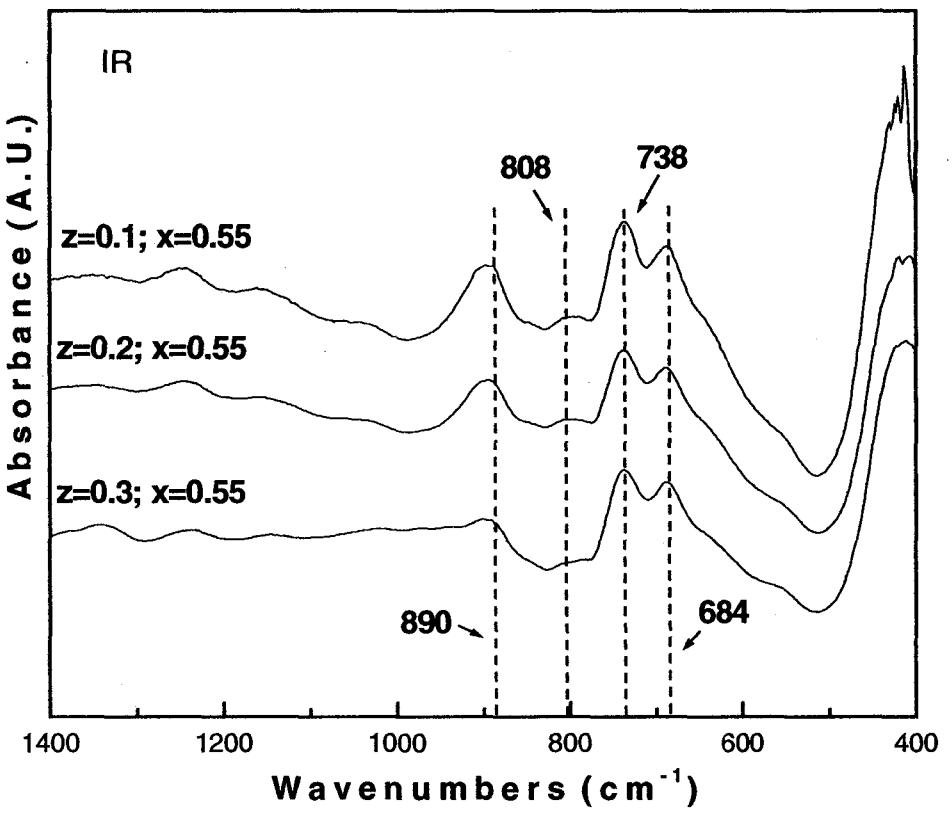

Figure 3.3 IR spectra of zLiI + (1-z)(0.55Li_2S + 0.45[0.5 B_2S_3 + 0.5 GeS_2]) glasses.

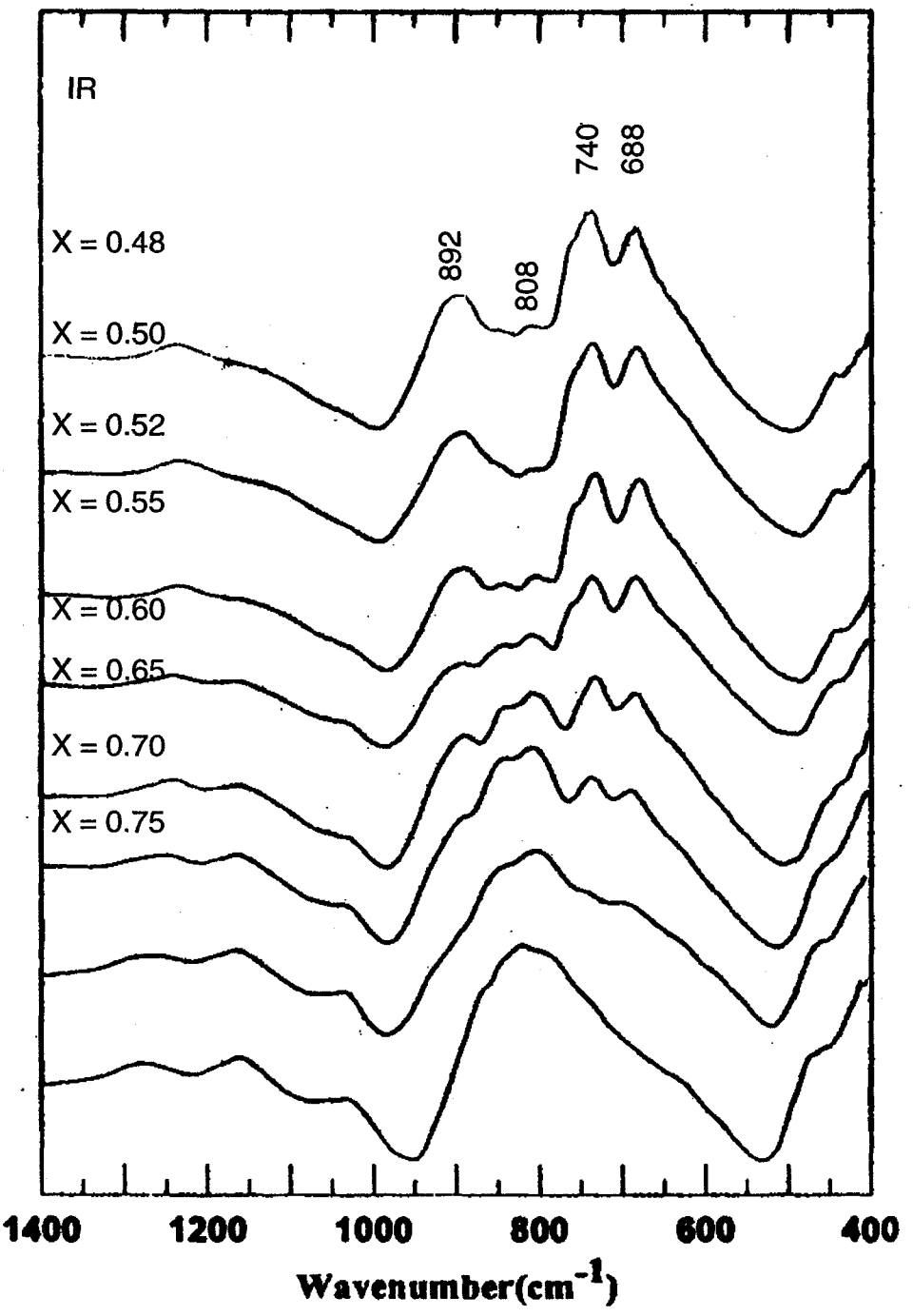

Figure 3.4 IR spectra of binary $xLi_2S + (1-x)B_2S_3$ glasses.[4]

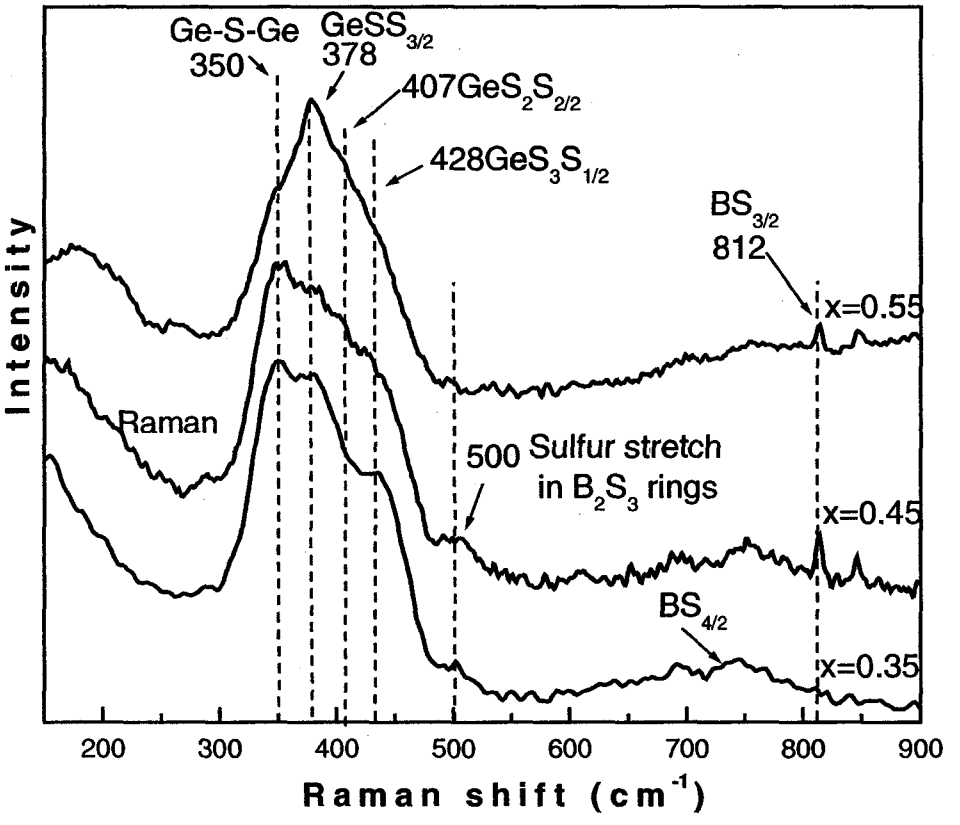

Figure 3.5 Raman spectra of ternary $xLi_2S + (1-x)(0.5\ B_2S_3 + 0.5\ GeS_2)$ glasses.

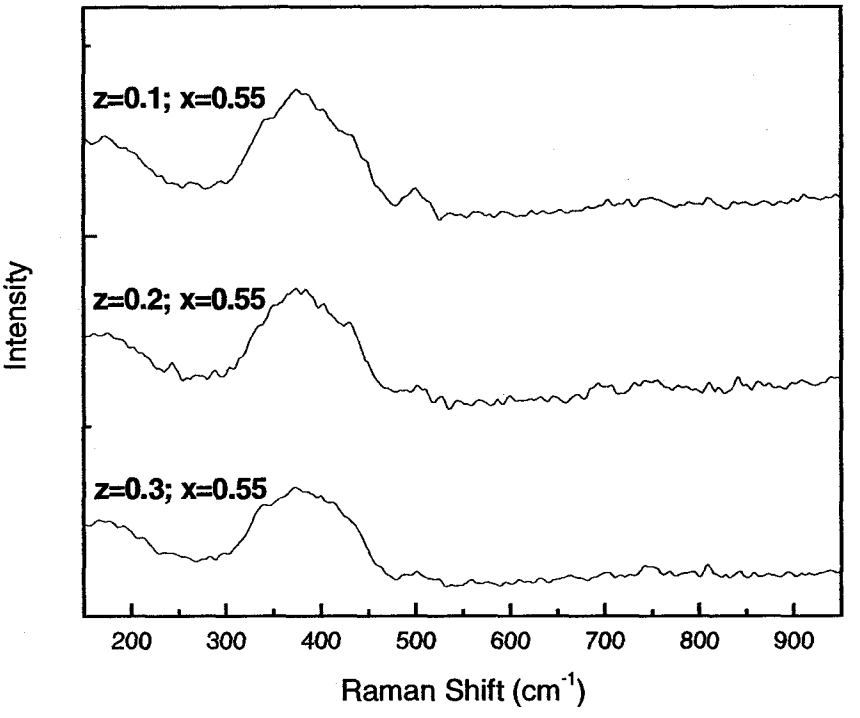

Figure 3.6 Raman spectra of zLiI + (1-z)(0.55Li_2S + 0.45[0.5 B_2S_3 + 0.5 GeS_2]) glasses.

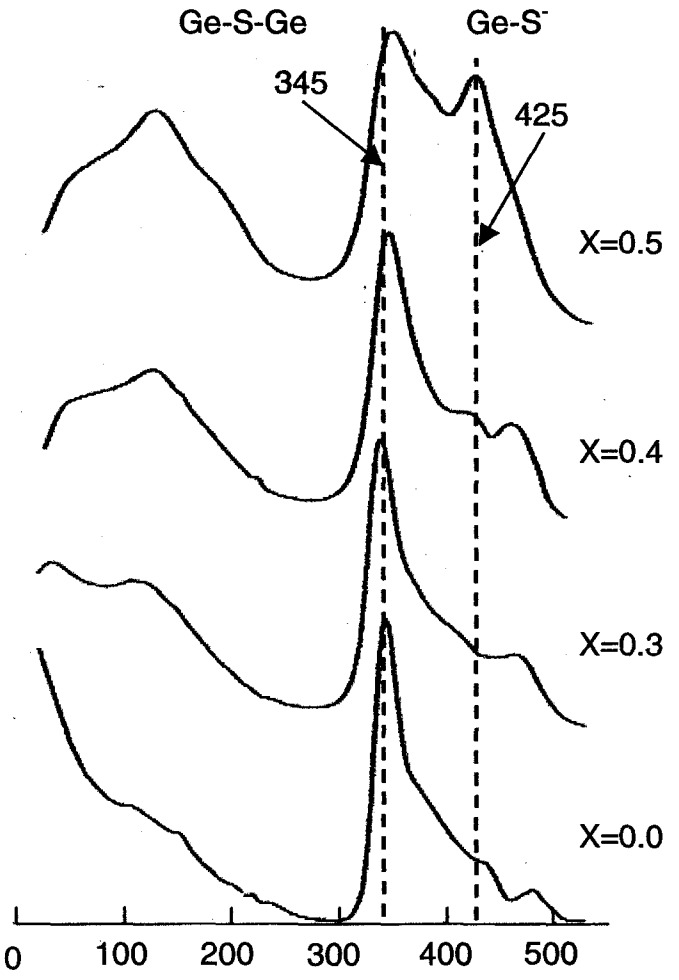

Figure 3.7 Raman spectra of binary $xLi_2S + (1-x)GeS_2$ glasses.[5]

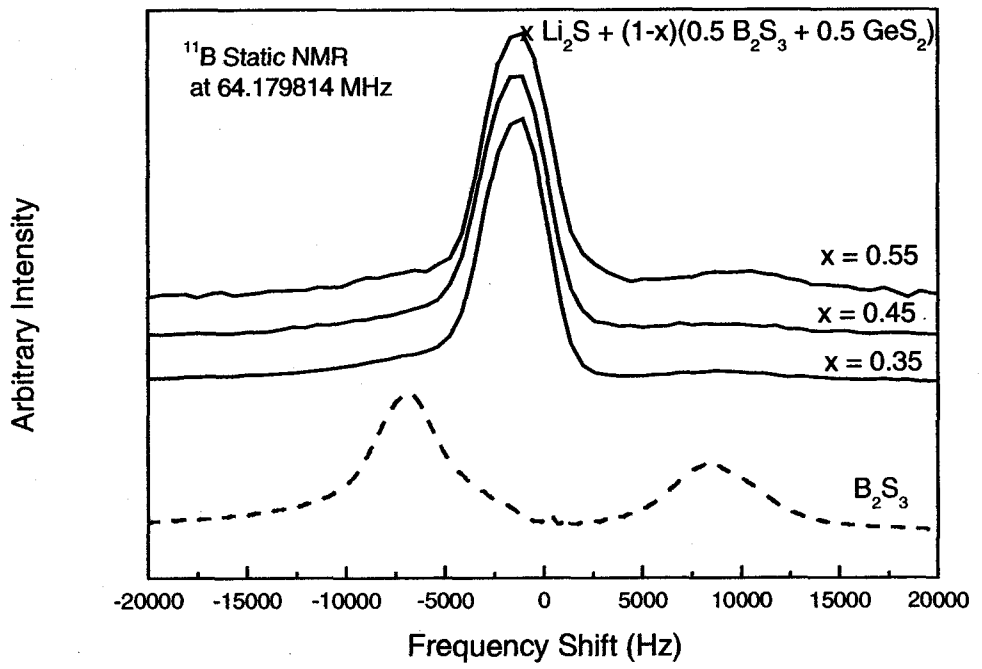

Figure 3.8 Static ^{11}Boron NMR spectra of B_2S_3 and the $xLi_2S + (1-x)[0.5\ B_2S_3 + 0.5\ GeS_2]$ glasses.

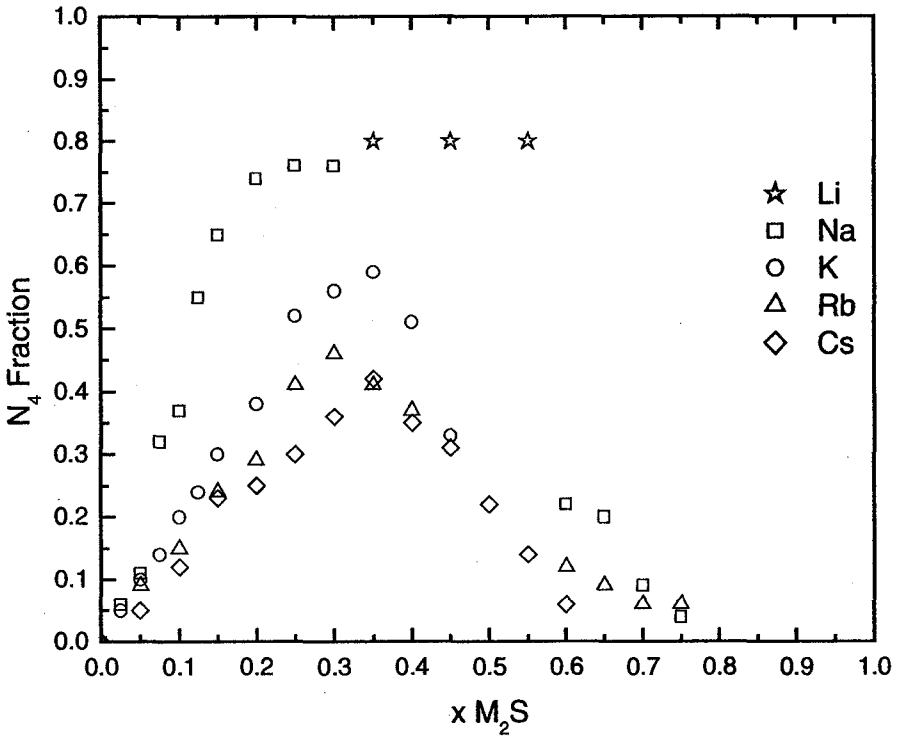

Figure 3.9 Comparison of N_4 fraction of tetrahedral boron in $xM_2S + (1-x)B_2S_3$ where M is Na, K, Rb, or Cs.[20,21,22]

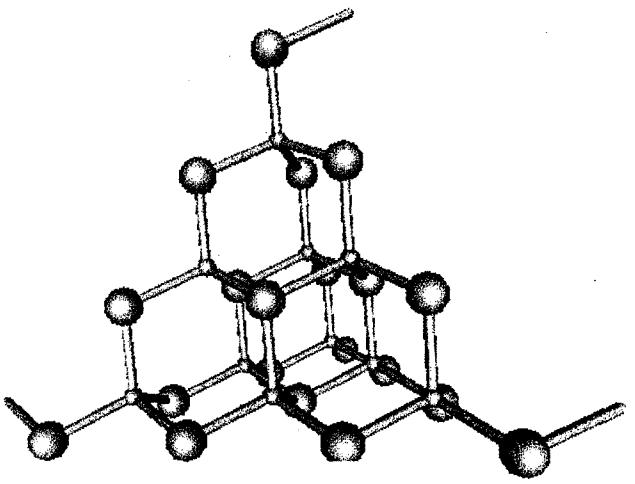

Figure 3.10 Ball and stick model of the $[B_{10}S_{18}]^{6-}$ macroanion.[31]

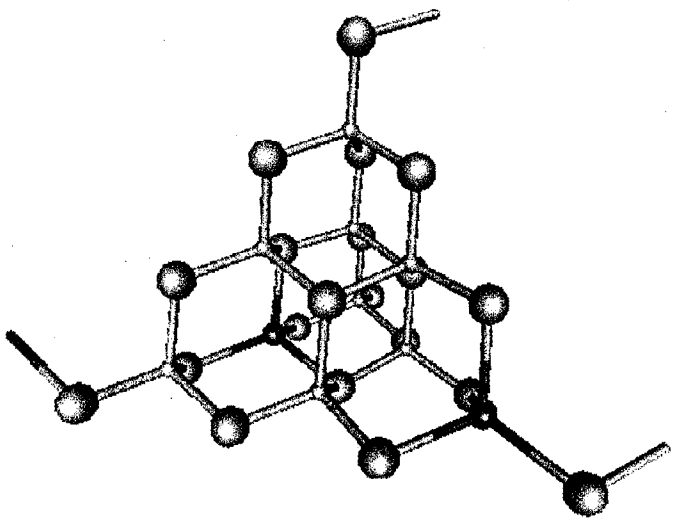

Figure 3.11 Possible structure for $[Ge_2B_8S18]^{6-}$ unit.

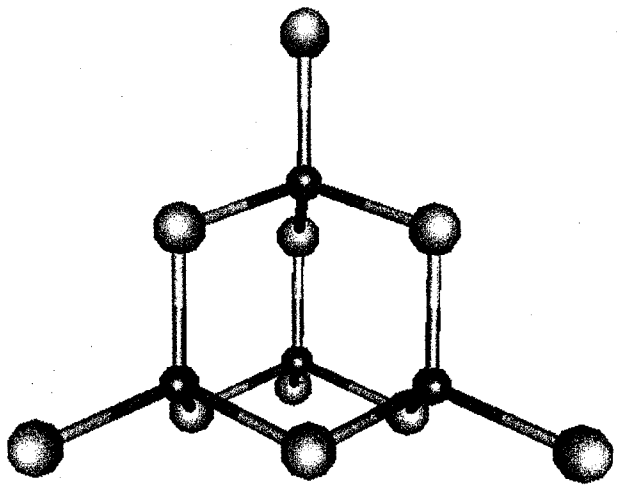

Figure 3.12 $Na_4Ge_4S_{10}$ structural unit in the $xNa_2S + (1-x)GeS_2$ glasses.[5]

3.7 References

[1] J. Kincs, S.W. Martin, Phys. Rev. Let., **76**, 70-73 (1996).
[2] B. Meyer, J. Schrooten, S.W. Martin, F. Borsa. To be submitted.
[3] S.W. Martin, D.R. Bloyer, J. Am. Ceram. Soc., **73**(11), 1003 (1991).
[4] J.Cho, S.W. Martin. Journal of Non-Crystalline Solids **170**, 182-189 (1994).
[5] J.L. Souquet et al. Solid State Ionics **3/4**, 317-321(1981).
[6] Mei, Quiang, Ph.D Thesis, Iowa State University, Ames, IA (2003).
[7] P. Tipler, Physics. Worth Publishers, Inc. New York, NY 1982, 378-381.
[8] K.H. Kim, D.r. Torgeson, F.Borsa, J. Cho, S.W. Martin, I. Savre, Solid State Ionics **91**, 7-19 (1996)
[9] K.H. Kim, D.r. Torgeson, F.Borsa, J. Cho, S.W. Martin, I. Savre, G. Majer, Journal of Non-Crystalline Solids **211**, 112-125 (1997).
[10] D. R. Lide, Handbook of Chemistry and Physics, CRC Press. New York, 82 Edition. (2001)
[11] Sinclair, Roger N.; Stone, Cora E.; Wright, Adrian C.; Martin, Steve W.; Royle, Michael L.; Hannon, Alex C. Journal of Non-Crystalline Solids 293-295 383-388 (2001).
[12] Royle, M.; Cho, J.; Martin, S. W. Journal of Non-Crystalline Solids **279**(2-3), 97-109 (2001).
[13] Hanbin Liu, Guangqui Shen, Progress in Crystal Growth and Characterization of Materials (2000) 235-241.
[14] K. Blaszczak, A. Adamczyk, Journal of Molecular Structure **596**, 61-68 (2001).
[15] S.W. Martin, D.R. Bloyer, Journal of the American Ceramics Society. **74**, 3481 (1990).
[16] E. I. Kamitsos, J.A. Kapoutisis, G.D. Chryssikos., Journal of Solid State Chemistry **112**, 255-261 (1994).
[17] J. Schrooten, B. Meyer, S.W. Martin, J. Non-Cryst. Stolids 318, 27-36 (2003).
[18] J.F. Emerson, P.E. Stallworth, P.J. Bray, J. Non-Cryst Solids **113**, 235 (1989).
[19] G.E. Jellison Jr., L.W. Panek, P.J. Bray, G.B. Rouse Jr., J. Chem. Phys. **66**, 802 (1977).
[20] Sills, J. A.; Martin, S. W.; Torgeson, D. R. Journal of Non-Crystalline Solids **175**(2,3), 270-7 (1994).
[21] Sills, J. A.; Martin, S. W.; Torgeson, D. R. Journal of Non-Crystalline Solids **168**(1-2), 86-96 (1994).
[22] Cho, J.; Martin, S. W.; Meyer, B.; Kim, K.-H.; Torgeson, D. R. J. Non-Cryst. Solids **270**(1-3), 205-214 (2000).
[23] P. zum Hebel, B. Krebs, M. Grune and W. Muller-Warmuth, Solid State Ionics 43, 133 (1990).
[24] Chemical Analysis: X-Ray Absorption, Koningberger and Prins. Vol. 92. New York (1988).
[25] H. Eckert, J.P. Yesinowski, J. Am. Chem. Soc. **108**, 2140 (1986).

[26] G. Barbarella, Prog. Nucl. Magn. Reson. spectrosc. **25**, 317 (1993).
[27] W. Daunch, P. Rinaldi, Journal of magnetic Resonance, Series A **123**, 219-221 (1996).
[28] R. Aitken, S. Arumugan, J. Chem. Soc., Perkin Trans. 2, 225-226 (2002).
[29] B. Barrau, M. Ribes, M. Maurin, Journal of Non-Crystalline Solids **37**, 1-14 (1980).
[30] A. Műller, B.N. Cyvin, S.J. Cyvin, S. Pohl, B. Krebs. Spectrochimica Acta, **32A**, 67-74.
[31] V.S. Pohl and B. Krebs, Zanorg. Allg. Chem. **424**, 265-272 (1976).

CHAPTER 4 NMR SPIN-LATTICE RELAXATION AND CONDUCTIVITY OF LITHIUM NON-ARRHENIUS FIC GLASSES

By

B. Meyer[a,b,c], S. W. Martin[b,d], F. Borsa[c], D. Martin[b]

A paper to be submitted to Physical Review B

May 2003

[a] Primary researcher and author
[b] Department of Materials Science & Engineering, Iowa State University, Ames, IA 50011
[c] Ames Laboratory – U.S. Department of Energy, Iowa State University, Ames, IA 50011
[d] Author to whom correspondence should be directed

Abstract

^{7}Li Nuclear Spin Lattice Relaxation (NSLR) and ionic conductivity measurements of Li doped $Li_2S + GeS_2 + B_2S_3$ glasses were performed to investigate the ion hopping dynamics and the non-Arrhenius conductivity behavior that has been observed in some fast ion conducting glasses. The NMR experiments were performed at 4 MHz and 8 MHz and over a temperature range of 183 to 523 K. Conductivity measurements on these glasses were also performed over the same temperature range. A distribution of activation energies (DAE) model was used to fit the NSLR results and conductivity results. Comparisons are made to previously studied lithium thio-germanate and lithium thio-borate glasses to help yield information about the conduction mechanisms in these new glasses. An ion trapping model (ITM) is used in conjunction with the distribution of activation energies model to describe the non-Arrhenius behavior observed in the dc conductivity.

4.1 Introduction

Fast ionic conducting glasses have received much attention for their potential for use in batteries and fuel cells.[1] It has been discovered that many of these highly conducting glasses show a non-Arrhenius behavior in the conductivity at higher temperatures.[2] Both NMR and ionic conductivity measurements have been used to gain valuable insight regarding the nature of ionic motion.[3] It has been well established that the dc conductivity in ionic conducting glass systems is a result of decoupling of the motions of the weakly bound cations from the host network comprised of B, Ge, and Si bonded together by oxygen or sulfur.[4] Models have been developed to explain the conductivity and NMR data for these conductive

materials. To date, the Kohlrausch-Williams-Watts (KWW) function and a distribution of activation energies (DAE) have been two of the most common models used to describe the NMR and conductivity data. However, neither model can explain the recently observed deviation from Arrhenius behavior of the conductivity at high temperature.[12] In this paper, we address the problem of the microscopic origin for the non-Arrhenius behavior by a combination of NMR and conductivity measurements in highly conducting superionic glasses.

This study will show that in spite of the deviation from Arrhenius behavior in the conductivity, there is no detectable corresponding deviation from the predicted curve for the NMR data by the DAE model for this particular family of glasses. A new trapping model[5] has been developed which accurately fits the non-Arrhenius behavior in the dc conductivity and gives insight to possibly why no deviation is seen in the NSLR measurements.

4.2 Experimental

4.2.1 Sample Preparation

The glass compositions prepared for this study were made by reacting stoichiometric amounts of high purity LiI(Aldrich 99% purity), Li_2S(Cerac 99.9% purity), GeS_2, and B_2S_3. Both GeS_2 and B_2S_3 were prepared by mixing and reacting germanium metal with sulfur and amorphous boron metal with sulfur.[6] All preparations were performed inside a high purity helium glove box, < 5 ppm O_2 and H_2O. Each sample was mixed and melted in a vitreous carbon crucible at 850 °C for 10 minutes. Weight loss was then recorded (typically less than 4%) and the sample was then reheated for another 5 minutes. The samples were poured into a graphite mold pre-heated to 200 °C. Samples quenched into brass molds would tend to

fracture or stick to the mold depending on the annealing, temperature whereas graphite molds allowed higher annealing temperatures without the samples sticking. Samples for NMR were then crushed and sealed into an evacuated quartz tube for NMR experiments. Samples for conductivity were annealed at 200 °C (at least 50 °C below Tg) for thirty minutes and then allowed to cool to room temperature at 5 °C/min. The disks were then sputtered coated with gold on both sides to form blocking electrodes for the conductivity experiments. The sputtering was performed at a pressure of 10^{-1} mbar of Argon, with a current of 18 mA for a total of four minutes on each side.

4.2.2 Density Measurements

Density measurements were made using Archimedes's principle.[7] These measurements were necessary to estimate the ion concentration in the samples needed to model the conductivity data. Results are shown in Table 4-1.

4.2.3 Conductivity Measurements

Complex impedance measurements were performed using a Solartron 1260 AC impedance spectrometer. The measurements were made by applying a sinusoidal voltage across the sample. Measurements were made from 180 to 520 K over a frequency range of 0.1 Hz to 10 MHz. The temperature was controlled to within ± 1 °C by placing the sample into a specially designed wide temperature range cell capable of reaching temperatures as low as 100 K to as high as 723 K.[8] Temperature control was accomplished by passing pre-cooled helium gas through a tube wrapped with nozzle-band heaters. Temperature scans were made at every

~12 °C. Individual frequency scans were not started until the standard deviation of the temperature was within 0.07 °C for the last 30 points measured every 2 seconds.

4.2.4 NMR Measurements

All NMR samples were sealed under vacuum in quartz tubes using an oxygen and propane torch to prevent sample contamination with oxygen and water in the atmosphere. ^{7}Li NSLR measurements were performed at Larmor frequencies of $\omega_L / 2\pi$ = 4 and 8 MHz over a temperature range of 180 to 520 K. The NMR spectrometer used was a phase-coherent pulse spectrometer which implemented a programmable pulse sequencer designed by Adduci.[9] This spectrometer also used a double side band r.f. switch designed by Torgeson. A fast recovery receiver designed by Adduci was used to retrieve the signal.[10] $T_{1\rho}$ measurements were acquired by applying a spin-lock pulse at an effective frequency of 70 KHz. The NMR signal intensity was then measured as a function of the duration of the spin-lock pulse.

Temperature scans in the NMR experiments were obtained by placing the sample into a custom built high temperature probe (Tmax ~500 °C) which used a furnace cavity placed inside a vacuum jacketed sleeve, variable temperature chamber. An Omega Engineering model 2012 three-term temperature controller was used to control the temperature. All measurements were performed when the temperature control was stable to within $\pm$1 degree Celsius. The furnace employed resistive heating, while dry nitrogen gas could be passed through as an air exchange to help facilitate cooling.

The ^{7}Li NSLR rate was measured using either saturation recovery or inversion recovery. Both methods were compared at different temperatures and were found to be in agreement. Saturation recovery consisted of a saturation pulse

followed by a 90° read pulse which was typically 2 μs long. The spectral width of the radio frequency pulses was sufficiently wide to excite both the central (1/2 ←→ -1/2) and satellite (±3/2 ←→ ±1/2) transitions of the ^{7}Li nuclei so that a single exponential recovery of the nuclear magnetization was observed in all cases. At all temperatures the acquisition delays were set to be at a minimum of ten times T_1.

$T_{1\rho}$ measurements were also performed using a 3.6 μs 90° pulse followed by a spin locking pulse. This method allows for the measurement of NSLR rates at an effective frequency in the rotating frame $\omega_1 = \gamma H_1$, where H_1 is the intensity of the r.f. field. While the spin-locking pulse is applied, the magnetization aligned along the H_1 direction no longer decays in a time characterized by the spin-spin relaxation, T_2, process. Instead it decays with a time, $T_{1\rho}$, representative of the time it takes for energy exchange with the lattice.[11] By varying the length of the spin-locking pulse, a value for $T_{1\rho}$ was extracted. The effective frequency for this $T_{1\rho}$ measurement was 70 kHz for ^{7}Lithium.

4.3 Model Development

4.3.1 Distribution of Activation Energies Model

It has been found that the correlation times for ionic hopping motion as derived from NMR and from conductivity measurements differs by an order of magnitude.[12,22,23,24] The NMR correlation time, τ_{NMR}, is determined by the BPP theory which gives $\tau_{NMR} \approx \omega_L$ at the peak of the NSLR curve. The correlation time for conductivity, τ_σ, is determined by $\tau_\sigma \approx \omega$ at the frequency above the dc plateau where the conductivity starts to increase. Several theoretical models have been proposed to account for the discrepancy.[13,14] However, it was shown that by incorporating a simple DAE with a percolation threshold it is possible to account for this discrepancy in a physically understandable fashion.[15,16] The major assumption

of this approach is that the ions are present in the glass and reside on a set of chemical sites that have differing energy barriers. This assumption is valid in view of known characteristics of the local disorder for a glass. The local disorder gives rise to barriers seen by hopping ions that vary in height and depth.

The DAEs are represented by the quantity $Z_{NMR}(\Delta E_a)$, where ions hop with different rates (r_a).

$$r_a = r_{0a} \exp(-\Delta E_a / k_b T) \tag{5-1}$$

ΔE_a is the activation energy barrier that an individual ion experiences when attempting to hop. The pre-exponential factor, r_{0a}, is a number representing the attempt rate of hopping at infinite temperature. An important key here is that the ion hopping attempt rates have been limited to numbers that are physically realistic. Kim[15] used the following relationship to obtain reasonable values for r_{0a},

$$r_{0a} = (\Delta E_a / 2m)^{0.5} / d \tag{5-2}$$

where m is the mass of the lithium ion, and 4 Å, a value that is slightly less than the Li ion separation distance calculated from composition, was used for the average jump distance, d. By assuming that each Li ion is neighbored by 6 empty sites, the pre-exponential factor for the correlation time was taken as:

$$\tau_{0a} = 1 / 6r_{0a} \tag{5-3}$$

The correlation time for any particular activation energy barrier can be calculated from Eq. (5-4).

$$\tau_a = \tau_{0a} \exp\left(\frac{\Delta E_a}{k_B T}\right) \tag{5-4}$$

The average relaxation rate, R_1, over the distribution of energy barriers can then be calculated from the following equation provided that the dipolar spin-spin (T_2) relaxation is significantly faster than the individual R_1 values for each ion.

$$R_1(\omega_L, T) = C\int_0^{\infty}\left[\frac{\tau_a}{1+\omega_L^2\tau_a^2} + 4\frac{\tau_a}{1+4\omega_L^2\tau_a^2}\right]Z_{NMR}\,d\Delta E_a \qquad (5\text{-}5)$$

As seen in Eq. (4-1), the average relaxation rate for the system, R_1, has a dependence upon temperature (T) and the Larmor frequency (ω_L). C is the coupling constant which gives a measure of the average of the square of a change in local quadrupolar field when the ion hops from site to site. Kim et al.[15] assumed a Gaussian DAE for Z_{NMR} centered at an average ΔE_m with ΔE_b as the standard deviation.[17] The following relationship for the DAEs, Z_{NMR}, was used.

$$Z_{NMR}(\Delta E_a) = \frac{1}{\sqrt{2\pi}\Delta E_b}\exp\left[-\frac{(\Delta E_m - \Delta E_a)^2}{2\Delta E_b}\right] \qquad (5\text{-}6)$$

In a random structure with varying activation energy barriers, it is required to have continuous percolation paths over the lowest barriers. From percolation theory[18], for a simple cubic lattice where each ion has z = 6 directions to hop, it is necessary to have a percolation fraction of P = 0.25 or higher for d.c. percolation. Assuming the same condition holds true for a glassy system, a fit for dc conductivity can be obtained when applying a percolation threshold.

$$P = \frac{\int_0^{\Delta Ep} Z_{NMR}(\Delta E_a)\,d\Delta E_a}{\int_0^{\infty} Z_{NMR}(\Delta E_a)\,d\Delta E_a} \qquad (5\text{-}7)$$

The average correlation time of the mobile ions that contribute to the measured conductivity is given in Eq. (5-8).

$$\tau_{avg}(T) = \frac{1}{P}\int_{0}^{\Delta Ep} \tau_a(\Delta E_a, T)_{ZNMR}(\Delta E_a)d\Delta E_a \qquad (5\text{-}8)$$

Eq. (5-9) below is the conductivity equation used to fit the dc conductivity where N is the concentration of cations, P is the percolation fraction, d is the jump distance (~4 Å), and $\tau_{avg}(T)$ is the average correlation time over the percolation threshold.

$$\sigma_{dc}(T) = \frac{NPe^2d^2}{6k_BT\tau_{avg}} \qquad (5\text{-}9)$$

Eq. (5-9) is used to fit the d.c. conductivity based upon the NMR determined distribution, $Z_{NMR}(\Delta E_m, \Delta E_b)$. P and ΔE_p are adjusted parameters to fit the d.c. conductivity.

4.3.2 Ion Trapping Model

D. Martin has developed a model which accurately fits the conductivity data for glasses and crystals showing non-Arrhenius behavior.[5] The implications of this model suggests that once an ion is thermally activated it is capable of traveling distances greater than 10 Å before it is recaptured into an anion site. This model is quite distinct from other models where a cation performs a single hop to the next neighboring location which is on the order of only a few Angstroms. A brief explanation of this model is given; however for a more complete derivation the reader is referred to the paper by Martin.[5]

Given a system with a concentration, c_0, of ions that can be activated to hop, the fraction of ions that are thermally promoted is given by Boltzmann statistics. In Eq.

(5-10), ΔEa is the activation energy, k_B is Boltmann's constant, T is temperature, and c(T) is the temperature dependent concentration of hopping ions.

$$c(T) = c_0 e^{\frac{-\Delta Ea}{k_B T}} \tag{5-10}$$

After the ions are thermally activated, they are considered as freely diffusing ions. Thus, the calculation for the drift velocity was performed using the approach from the kinetic theory of gases.[19] An activated ion would acquire a drift velocity over the mean free path λ until an event occurs to stop its travel. Therefore, in the presence of an electric field we can write the following relationship.

$$\frac{1}{2} m\left((\upsilon_{0x} + \Delta\upsilon_x)^2 + \upsilon_{0y}^2 + \upsilon_{0z}^2\right) \cong \frac{1}{2} m\upsilon_0^2 + m\upsilon_{0x}\Delta\upsilon_x = k_B T + q\lambda \frac{dV}{dx} \tag{5-11}$$

Since thermal energy does not have a preferential axial direction we can write.

$$\upsilon_0^2 = \upsilon_{0x}^2 + \upsilon_{0y}^2 + \upsilon_{0z}^2 = 3\upsilon_{0x}^2 \tag{5-12}$$

From Eqs. (5-11) and (5-12), the average drift velocity is written as the following.

$$\Delta\upsilon_x = \frac{q\lambda}{\sqrt{\frac{2mk_B T}{3}}} \frac{dV}{dx} \tag{5-13}$$

The current generated by the drifting charges is:

$$i_x = qcA\langle\Delta u_x\rangle = qcA \frac{q\lambda}{\sqrt{\frac{2mk_B T}{3}}} \frac{dV}{dx} \tag{5-14}$$

Conductivity is given by the current density divided by the electric field.

$$\sigma = \frac{cq^2\lambda}{\sqrt{\frac{2mk_B T}{3}}} \tag{5-15}$$

The mean free path, λ, is taken to be the reciprocal of the additive inverses of two mean free paths, λ_0 and λ_1. In this model, it is hypothesized that as a cation is migrating through the glass network, it experiences both repulsive and attractive forces due to other anions and cations respectively. As the mobile cation increasingly approaches an anion, the attractive forces become greater and

ultimately pull the cation into the trap. The number of anions is temperature dependent. Therefore, λ_1, the temperature dependent mean free path, is calculated in Eq. (5-16) from the concentration of coulombic traps created by the thermal excitation of cations from their equilibrium sites and the trapping cross-section of interaction, πd^2.

$$\lambda_1(T) = \frac{1}{\sqrt{2}\pi d^2 c_0 \exp\left(\frac{-\Delta Ea}{k_B T}\right)} \tag{5-16}$$

In Eq. (5-17), d is calculated by equating the electrostatic force between an anion and cation to the centripetal force experienced by a moving cation at a distance, d, away from the center of an anion site.

$$d = \frac{e^2}{8\pi\varepsilon_0\varepsilon_\infty kT} \tag{5-17}$$

Since the concentration of traps is temperature dependent, this would lead to an infinite mean free path at T = 0 K. To avoid this unacceptable result, λ_0 has been proposed to introduce a low temperature mean free path maximum. Hence, $\lambda(T)$ takes on the following form which is the reciprocal of the additive inverses of the two mean free path terms.

$$\lambda(T) = \left[\frac{1}{\lambda_0} + \frac{1}{\lambda_1(T)}\right]^{-1} \tag{5-18}$$

At low temperatures λ_0 is much smaller than λ_1 and therefore dominates as the overall mean free path. As temperature increases the number of extrinsic traps increase at the same rate that new ions are thermally activated. It can be seen in the above equation, at higher temperature λ_1 gradually becomes much smaller than

λ_0 and dominates the equation. The extrinsic traps can be thought as the vacant sites from which the ions were activated. When an ion comes within the vicinity of these charged vacant sites, it is attracted by the coulomb force.

It should be noted that the concept of the ITM is similar to variable range hopping introduced by Mott for electronic conduction in glasses containing transition metal ions.[20,21] The similarities arise in that conducting electrons see coulombic potential wells created by the presence of transition metal ions, e.g. V^{4+}, V^{5+} or Fe^{2+} and Fe^{3+}.

4.4 Results

4.4.1 Static ^{7}Lithium NMR Measurements

At room temperature and above, only one narrow ^{7}Li NMR central line was seen in the absorption spectra at both 4 MHz and 8 MHz. At these temperatures, the normally seen broader line associated with the satellite transitions was narrowed due to the fast motion of the Li+ ions in these glasses. Therefore, as reported by Kim et al.[22] all of the relaxation measurements yielded a single exponential recovery. In fact, for initial conditions of saturation of both the central and satellite lines, the single exponential recovery of the nuclear magnetization yields:

$$R_1 = T_1^{-1} = \frac{2}{5}(W_1 + 4W_2) \qquad (5\text{-}19)$$

where W_1 and W_2 are the quadrupolar relaxation transition probabilities between Zeeman levels with $\Delta m = \pm 1$ and ± 2 respectively.

Figure 4.1 shows the ^{7}Li relaxation rates, $R_1(\omega,T)$, on a semi-log plot for the z=0.0; x=0.55 sample. On the low temperature side, the asymmetry in the curve is due to the nature of disordered materials and has been explained by the DAEs

model proposed by Kim et al.[22] Also, shown in the figure is $T_{1\rho}$ measurements for the respective samples at an effective frequency. In the rotating frame $\omega_1 = \gamma H_1$ where H_1 is the intensity of the radio frequency (r.f.) induced field.

Examining the relaxation rate curves, it was found that the z=0.0; x=0.55 glass exhibited a very broad maximum around 250 K. The maximum relaxation rates were approximately 100 ms^{-1} and 150 ms^{-1} for the 4 MHz and 8 MHz curves, respectively. At higher temperatures the relaxation curves appear to coalesce into a common straight line upon which the slope represents the average activation energy of the ionic species in the sample. At lower temperatures, R_1 curve shows an asymmetry which is accounted for in the DAE model. At lower temperatures the measured relaxation curve deviates from the BPP predicted ω^{-2} dependence. This effect which has been typically seen in many glassy systems is due to non-exponential decays of the time correlation function that arises from having a DAE.[22]

The NSLR curves were fitted using 4 Å, a value slightly smaller than the calculated ion separation distance based on composition, for the jump distance, d. This value was used to determine the hop attempt rate given by equation (5-2). Eqs. (5-2) - (5-4) were used to calculate the correlation times for different activation energy barriers. The parameters ΔE_m, ΔE_b, and C were then adjusted to yield good fits of the NSLR data at all frequencies measured.

The DAE model gives a good agreement using the parameters that were derived from the NMR measurements and is then used to calculate the conductivity data. Before the development of the DAE model, it had been observed the NMR

and conductivity measurements yielded parameters that differed significantly using the KWW stretched exponential function.[22,23,24]

The DAE model is based upon from the Bloembergen-Purcell-Pound (BPP) theory.[25] The BPP theory describes the situation where all ions see a single activation energy. The magnitude of this activation energy greatly affects the frequency at which the ions are successfully able to hop across the barrier based on a Boltzmann's probability. However, Kim et al.[15] showed that it was necessary to incorporate a DAE to accurately account for the low-temperature-side asymmetry of the NSLR theory maximum observed in glasses. The activation energy derived from the high temperature frequency independent region of the NSLR curve is proportional to the measured activation energy from the d.c. conductivity experiments when using the DAE model.

In this work it was found that fitting the data with a single DAE required a width of 1800 K, Figure 4.1 and Figure 4.2. A DAE with such a broad distribution was not surprising; it was expected that a large width would be needed to account for the differences in activation energies between the two incorporated glass formers (B_2S_3 and GeS_2). While the single DAE fit was reasonably good, the full breath of the curve could not be well fitted without having an overshoot on the low temperature side. Not surprisingly, a second DAE can be used to more accurately fit both the high and low temperature sides, Figure 4.4. With two distributions, the fit is better in that the full breadth of the curve is accounted for and there is less of a low temperature overshoot. A comparison can be seen in Figure 4.1 and Figure 4.3. Similarly, Kim et al.[12] found that it was necessary to use two distributions to fit the

relaxation curves in the binary thio-borate glasses, where the two separate distributions describe boron atoms in trigonal and tetrahedral coordination.[26] In this current study, it was found that the two distributions needed to fit the data represent lithium atoms associated with germanium sites and tetrahedral boron sites. From the ^{11}B NMR spectra, it is reasonable to assume that there are some trigonal boron sites present which do have some lithium ions associated with them. The ^{11}B NMR spectra show that 80% of the boron are in tetrahedral coordination. If it is assumed that there are an equal number of trigonal boron with non-bridging sulfur and trigonal boron with all bridging sulfur, then ~5% of the lithium could be associated with trigonal boron atoms. Since two distributions are already being used, this extra 5% does not make a significant impact in the shape of the relaxation curves; thus it does not unambiguously improve the fit used. Therefore, a distribution of activation energies for lithium ions associated with trigonal boron atoms with a non-bridging sulfur was not included.

Table 4-2 gives the parameters, ΔE_m, ΔE_b, and C in Eqs. (5-5) and (5-6) used to give best fits to the data shown in Figure 4.5. As shown in Figure 4.6 the activation energy, ΔEm, decreases in both the germanium sites and boron tetrahedral sites with increasing Li_2S. For the germanium sites in the ternary glasses, values very similar to that of the germanium sites in the binary $Li_2S + GeS_2$ system were used. For the case of the boron sites, there is no direct comparison since only binary glasses at the x = 0.65 and 0.70 compositions were prepared. However, a systematic decreasing trend can be seen when plotting the average activation energy versus composition for x = 0.35 to x = 0.7. The average activation

energy decreases from 4200 to 3300 K. A slight decrease in the activation energy was seen with added LiI for the germanium sites, while the activation energy for the boron sites remained unchanged, Figure 4.11.

Similar to the germanium sites in the binary glasses, the width, ΔE_b, of the distribution does not change significantly with added Li_2S over the x = 0.35 to x = 0.55 compositional range, Figure 4.7. However, there is a decrease from 650 to 480 K in the width of the distribution for the tetrahedral boron sites from x = 0.35 to x = 0.55 in the ternary system. For the LiI doped glasses, no significant change in the distribution width was seen, Figure 4.12.

Some assumptions had to be made when selecting values for the coupling constants, C in Eq. (5-5). The first assumption was that the environments that the lithium ions see around the germanium and boron atoms in the ternary glasses will probably not differ greatly from the corresponding sites in the binary glasses. Hence, the coupling constants, C, in the ternary glasses were taken to approximately be the same as to the values used in fitting the corresponding binary systems. The values for C are shown in Figure 4.8. The total relaxation, R_{total}, was then fitted by taking a weighted average of the relaxation times for both the germanium sites and boron sites in the ternary glasses. The two sites are weighted according to the fraction of lithium ions associated with them. The sum of the fraction parameters, f1 and f2 in Eq. (5-20), should equal 1 to account for all of the lithium ions in the samples. This effectively creates a weighted average of the two distribution sites to give the overall measured relaxation curve. The total relaxation is given by Eq. (5-20).

$$R_{Total}(\omega_L, T) = f1 * R_1(\omega_L, T) + f2 * R_2(\omega_L, T) \quad (5\text{-}20)$$

Values for the coupling constants, which are embedded in the R_1 and R_2 terms in the equation above, used in the fits are shown in Table 4-4. The coupling constant values used in the fit reveals that the lithium atoms are distributed such that 70% to 80% of the lithium ions undergo relaxation around germanium sites, while the remaining 20% to 30% relax around boron sites. Fits to the NSLR curves for samples containing various concentrations of LiI are shown in Figure 4.13 through Figure 4.16. Equal sharing based on composition alone would seem to suggest 67% of the lithium to be associated with boron and 33% to be associated with germanium since the ratio of boron to germanium is 2:1. However, the preference of lithium ions to distribute heavily toward germanium sites is in agreement with the qualitative results shown by IR and Raman spectra taken of these glasses.[27]

4.4.2 Conductivity Results

4.4.2.1 D.C. Conductivity Results

Figure 4.17 shows the real part of the ac conductivity for the z = 0.2; x = 0.55 sample. In order to more accurately measure the dc conductivity, the d.c. values were determined using a Nyquist plot (Figure 4.18), and extrapolating to the x-axis intercept along the real impedance axis.

Figure 4.19 shows the d.c. conductivity on an Arrhenius plot for the highest conducting LiI doped glasses. The highest conductivity measured at room temperature is between 10^{-3} and 10^{-4} $(ohm\ cm)^{-1}$. With increasing Li_2S content, the activation energy decreases. This can be seen by the changes in slope of the data curves on the Arrhenius plot. As predicted by the NMR data, the addition of LiI only

causes a slight decrease in the activation energy. Similar to the silver fast ion conducting systems[28], the addition of LiI does increase the conductivity. The glasses in this study also show increasing deviation from Arrhenius behavior with increasing LiI content.

In an effort to rule out electrode effects and oxidation of the glass giving rise to the non-Arrhenius behavior, two consecutive temperature scans were performed on the same z = 0.2; x = 0.55 sample. The heating profile, Figure 4.21, shows that the sample was held for 6 hours at 200 °C for six hours before cooling and repeating the run with the same sample. It can be seen that the second run almost exactly overlays on top of the first run, Figure 4.20.

The dc conductivity was fitted with the DAE model by using the distribution of activation energies determined by the NMR measurements. The average correlation time, τ_{avg}, was determined by taking the weighted average of all correlation times corresponding to activation energy barriers from 0 K up to a percolation threshold, ΔE_p given in Table 4-5. The value for ΔE_p is determined by best fitting Eq. (5-9) to the dc conductivity data. Again, 4 Å was used for the average jump distance, d, for reasons discussed above. The ion concentration, c_0, was calculated from composition and density measurements shown in Table 4-1. Typically, the value determined for ΔE_p represents the limit where the fraction of activation energy barriers at lower values comprise approximately 1/3 of the total distribution sites determined by NMR.

The dashed lines in Figure 4.19 are fits to the data using the Distribution of Activation Energies model with a percolation threshold. It can be seen from Figure

4.19) that the DAE model fails to fit the Non-Arrhenius behavior. However, the DAE model does accurately predict the Arrhenius portion of the dc conductivity plots.

The ITM is able to fit both the Arrhenius and non-Arrhenius regions of the d.c. conductivity very well as shown in Figure 4.22. The dc conductivity was fitted using Eq. (5-18) where ΔE_a was substituted by the integral over the NMR determined distribution of activation energies, Z_{NMR}. Ion concentration, c_0, was calculated from the known composition and density measurements shown in Table 4-1. Since the conductivity in these glasses are high, and the ac impedance measurements are limited to 1 MHz, it is impossible to experimentally determine values for ε_∞ even at liquid nitrogen temperatures. We have chosen to use the Lorentz-Mossotti relation, $\varepsilon_\infty \sim n^2$, where n is the index of refraction to estimate the optical frequency value of ε_∞. In the present case, the index of refraction parameter was allowed to vary for purposes of fitting the data and in the future refractive index measurements will be made to confirm the values obtained. The values for n_0, index of refraction, remained at a value of approximately 1.5 regardless of the concentration of LiI, a value not to dissimilar than that expected for these glasses, Figure 4.23. λ_0 values were calculated from the inverse cube root of Eq. (5-10) where the temperature is set to Tg. λ_0 increases from 5.5 nm to 6.6 nm with the addition of LiI (Figure 4.24). Figure 4.25 shows the average activation energy used and its comparison to the weighted average calculated from the NMR determined parameters. The values for the width of the distribution of activation energies, ΔE_b, is shown in Figure 4.27 and are on the order of 450 K. The width, ΔE_b, used in the ion trapping model is quite

narrow compared to experimentally determined values by NMR, $\Delta E_b \sim 1200$ K. A comparison between the NMR determined width and the width fitted for the ITM is shown in Figure 4.26.

4.5 Discussion

4.5.1 Analysis of the Effects of Electrode Reaction and/or Oxidation

The consecutive temperature dependent conductivity scans shown in Figure 4.20 were performed to rule out any electrode reaction or oxidation of the sample that could give rise to the non-Arrhenius conductivity behavior. This extra step was important to perform considering that the NSLR curves do not show any apparent deviation from BBP theory at the corresponding temperatures where the non-Arrhenius behavior occurs in the dc conductivity plots. After the first temperature scan, the sample was held at 200 °C to determine what time dependent effects were due to electrode effects or oxidation of the sample. The change over a six hour period was insignificant in comparison to the deviation from non-Arrhenius behavior. Yet, this alone is not sufficient to rule out electrode reaction and/or oxidation. While the sample is held at highest temperature, the kinetics of the degradation process should be the fastest. This implies that the reduction in conductivity due to these processes should be greatest with a sample held at the highest temperature (T_{end}) compared to a sample ramped over a range of temperatures (T_{begin} to T_{end}) in the same duration of time. However, if electrode reaction or oxidation of the sample was assumed to cause the non-Arrhenius behavior, then in the best case, the dc conductivity behavior of the sample in a second temperature scan would be an

Arrhenius line passing through the last high temperature value measured on the first scan. As seen in the Arrhenius plot shown in Figure 4.20, the second temperature scan falls directly on top of the first scan especially in the non-Arrhenius region. Any electrode reaction or oxidation that could have occurred in the first run should be irreversible and thus the second scan would show a conductivity that is significantly lower for the second temperature scan. Therefore, the fact that the second run repeats the first is strong evidence suggesting that the non-Arrhenius effect is due to a bulk effect of the sample and not a result of oxidation or electrode reaction.

4.5.2 DAE Approach to Fitting the NMR and Conductivity Data

The T_1 measurements at all temperatures yielded a single exponential relaxation curve suggesting that all of the lithium atoms were able to reach a common spin temperature. The fitted parameters from using two distributions with the DAE model showed that the average activation energy (ΔE_m), distribution width (ΔE_b), and coupling constants (C) for the ternary system are consistent with the binary thio-borates and binary thio-germanates values. The resulting sum of the two distributions yields an overall single asymmetric DAE for the ternary glasses.

Similar to silver thioborogermanate glasses[29], ^{11}B NMR has shown that a very high fraction, ~80%, of the boron atoms in these glasses are in tetrahedral coordination. The very small fraction of the trigonal boron atoms that have associated lithium ions allows for a range of values for ΔE_m, ΔE_b, and C to be used without changing the NSLR fits significantly. Hence, unambiguous values for ΔE_m, ΔE_b, and C cannot be obtained by introducing this third DAE for the boron atoms in trigonal coordination with non-bridging sulfur atoms.

As Li_2S content is increased the average activation energy for both the germanium sites (6000 K to 5100 K) and boron sites (4200 K to 3700 K) decrease accordingly. The trend of decreasing widths of the DAE's with added Li_2S is consistent with binary thio-germanate and binary thio-borate glasses.

The coupling constants for the germanium sites were found to be higher in the ternary glasses compared to the binary. Qualitatively the ^{11}B NMR, ^{7}Li NMR, IR, and Raman data all suggest that there is large preference for the lithium ions to associate with germanium sites. It appears that ~70 to 80% of the lithium goes toward the germanium, though this number can vary depending on what values are assumed for the coupling constants and if any lithium are assigned to trigonal boron groups with one non-bridging sulfur.

As LiI concentration is increased, the average activation energy for the germanium site environments decreases from 5200 K to 4800 K. The energy barrier height for the tetrahedral boron also decreases from 4100 K to 3900 K. The lowering of the activation energy is typically seen in many glass systems when halide salts are added.[29,30]

4.5.3 Ion Trapping Model of the Non-Arrhenius Conductivity

Table 4-6 shows the parameters used to fit the data with the Ion trapping model. Except for the decreasing activation energy width added LiI, there doesn't appear to be any significant trends in the parameters with change in composition. The index of refraction, n, has a fairly constant value of 1.5. It is very important that this parameter is confirmed through independent refractive index measurements. As the index of refraction has a significant affect on the value for the effective trapping diameter. λ_0 gradually increases with added LiI because the average activation energy decreases with added LiI and thus gives rise to a larger number of ions thermally activated at the same temperatures when compared to samples with

higher average activation energies. When using the compositionally determined value for c_0, it is necessary to use an average activation energy that is the weighted average of the middle activation energies for the two distributions from the NSLR experiments. This weighted average is calculating using 70 to 80 % of the lithium ions associate to the germanium sites for the respective compositions. However, the width used in the fit with the ion trapping model is 2 to 3 times smaller than determined by NMR (Figure 4.26). Even with perfect overlap of both the boron and germanium distributions of activation energies, it is expected that the average distribution width determined by the ion trapping model would be at least a minimum of the larger, germanium distribution, width which is approximately 1000 K for this series of glasses.

The first issue is regarding the narrow distribution shown in Figure 4.26 needed to fit the conductivity data using the Ion Trapping Model. In the DAE model it is necessary to incorporate a percolation fraction of approximately 30 % at the lower energy barriers to give rise to the macroscopic conductivity. The ITM is able to fit the data with a single narrow distribution centered around ΔEm determined by NMR.

With the non-Arrhenius behavior in the d.c. conductivity at higher temperatures, it would not be unreasonable to expect to all see a deviation from BPP theory at corresponding temperatures for these glasses. Yet, NSLR measurements have shown that no departure from BBP theory on the high-temperature-side exists for these glasses.

The fact that no deviation seen in the NSLR curves at higher temperatures and the narrow distribution is required for the ITM could be a simple consequence of the differences in the significance of the measured ΔEa of the DAE model and the ITM. There could be an extra small activation energy barrier that must be overcome

for the cation to be excited above all barriers, i.e. to behave "free like". If this extra barrier is not overcome, the cation is hops back into the site from which it was thermally activated. This maybe further explained by determining the actual number of ions that contribute to the macroscopic conductivity. Hypothetically, it could be possible that the number of ions contributing to actual macroscopic conductivity could be as low 5% of the total ions thermally activated. That is only 5% of the ions have sufficient thermal energy to overcome all barriers, cation labeled (B) in Figure 4.28. If this were the case, NMR would be insensitive to this 5% and the signal would be dominated by the 95% of ions being thermally activated and recaptured from the site they left, cation labeled (A) in Figure 4.28. The remaining 5% would be undetectable outside of the noise in the NMR measurements.

The ITM does not explicitly state that this scenario occurs, however, it also does not exclude the possibility for the scenario either. The ITM establishes that the average distance that a mobile ion travels is $\lambda trap(T)$. It should be noted that this value is an "average" and does not describe specifically the dynamics of the ions individually. Therefore, theoretically it could be possible for a large number of ions to travel very short distances (e.g. 4 Å) while a small population of ions travel significantly longer distances (e.g. 100 Å) compared to $\lambda trap(T)$. Any distribution of distances traveled is allowable as long as the weighted average of distance traveled is $\lambda trap(T)$.

It should be mentioned that the unified site relaxation model developed by Bunde et al.[31] suggests a localized hopping back and forth motion until a coulombic field is relaxed and that the neighboring target site relaxes to adjust for the incoming ion. Neutron scattering measurements for both $Ag_2S + B_2S_3 + GeS_2$ and $Ag_2S + B_2S_3 + SiS_2$ samples covered in previous work have shown that the ion-ion separation is only 3-4 Å for the heavily doped silver glasses.[32,33,34] Calculations of

the separation distance from the composition and density are also in agreement that the separation distance should be on the order of a few Å. This would also suggests that the cations contributing to the conductivity must travel longer distances to find an open anion site opposed to hopping to the neighboring site which is already occupied by a cation only a few Angstroms away. Otherwise, the cation is destined to fall back into the site from which it was thermally activated.

4.6 Conclusions

This study has shown that the NMR and d.c. conductivity data of the ternary compositions can be fitted using weighted sums of the binary components. It has been determined from the NMR fits that 70 to 80% of the lithium ions are associated to Germanium sites. Again, the DAE model provides an excellent fit for the Arrhenius portions of the d.c. conductivity plots at low temperatures. The ITM can be used to accurately fit the d.c. conductivity at both low temperatures and higher temperatures where the non-Arrhenius behavior dominates. However, the ion trapping model uses a distribution of activation energies width which is one half to one third the width of the expected distribution as determined by NSLR. It is possible that the ΔEa determined by the two models do not have the same significance. One scenario that a small fraction (maybe only 5%) on the thermally activated ions are excited over all barriers and are able to contribute to the macroscopic conductivity. The remaining 95% of the cations that are thermally activated are recaptured from the site they left and this is the population that dominates the NMR relaxation.

Table 4-1 Density and ion concentration for ternary samples in zLiI + (1-z)[xLi_2S + (1-x)($0.5B_2S_3$+$0.5GeS_2$)] glasses.

Sample	Density (g/cc)	Calculated total ion (number/m^3), C_0
X=0.35	2.19 ± 0.06	1.028×10^{28}
X=0.45	2.23 ± 0.06	1.467×10^{28}
Z=0.0, X=0.55	2.20 ± 0.06	1.943×10^{28}
Z=0.1, x=0.55	2.28 ± 0.06	1.878×10^{28}
Z=0.2, x=0.55	2.37 ± 0.06	1.828×10^{28}
Z=0.3, x=0.55	2.59 ± 0.06	1.875×10^{28}

Table 4-2 Average activation barriers, ΔE_m, determined from NSLR measurements using DAE fit in $zLiI + (1-z)[xLi_2S + (1-x)(0.5B_2S_3+0.5GeS_2)]$ glasses.

Composition	Germanium site (binary)[22]	Germanium site (ternary)	Tetrahedral boron site (binary) [26]	Tetrahedral boron site (ternary)
X=0.35	6100 K	6000 K $\pm$200 K		4200 K $\pm$100 K
X=0.45	5650 K	5500 K $\pm$200 K		4000 K $\pm$100 K
X=0.55	5000 K	5100 K $\pm$200 K		3700 K $\pm$100 K
X=0.65			3430 K	
X=0.7			3300 K	
	Germanium site (quartenary)		Boron tetrahedral site (quartenary)	
Z=0.1; x=0.55	5100 K $\pm$200 K		3700 K $\pm$100 K	
Z=0.2; x=0.55	4900 K $\pm$200 K		3700 K $\pm$100 K	
Z=0.3; x=0.55	4800 K $\pm$200 K		3700 K $\pm$100 K	

Table 4-3 DAE standard deviation, ΔE_b, determined from NSLR measurements and DAE fit in $zLiI + (1-z)[xLi_2S + (1-x)(0.5B_2S_3+0.5GeS_2)]$ glasses.

Composition	Germanium site (binary) [22]	Germanium site (ternary)	Tetrahedral boron site (binary) [26]	Tetrahedral boron site (ternary)
X=0.35	1100 K	1100 K $\pm$100 K		650 K $\pm$50 K
X=0.45	1100 K	1100 K $\pm$100 K		540 K $\pm$50 K
X=0.55	1000 K	1000 K $\pm$100 K		480 K $\pm$50 K
X=0.65			360 K	
X=0.7			260 K	
	Germanium site (quartenary)		Boron tetrahedral site (quartenary)	
Z=0.1; x=0.55	1000 K $\pm$100 K		400 K $\pm$50 K	
Z=0.2; x=0.55	1000 K $\pm$100 K		440 K $\pm$50 K	
Z=0.3; x=0.55	1000 K $\pm$100 K		400 K $\pm$50 K	

Table 4-4 Coupling constants, C, determined by NSLR measurements and DAE fit for $zLiI + (1-z)[xLi_2S + (1-x)(0.5B_2S_3+0.5GeS_2)]$ glasses.

Composition	Germanium site (binary) [22]	Germanium site (ternary)	Tetrahedral boron site (binary)[26]	Tetrahedral boron site (ternary)
X=0.35	10.2 $(rad/s)^2$	10.7 $(rad/s)^2$ $\pm$0.5 $(rad/s)^2$		6.7 $(rad/s)^2$ $\pm$0.5 $(rad/s)^2$
X=0.45	8.0 $(rad/s)^2$	8.5 $(rad/s)^2$ $\pm$0.5 $(rad/s)^2$		6.4 $(rad/s)^2$ $\pm$0.5 $(rad/s)^2$
X=0.55	7.8 $(rad/s)^2$	8.1 $(rad/s)^2$ $\pm$0.5 $(rad/s)^2$		6.3 $(rad/s)^2$ $\pm$0.5 $(rad/s)^2$
X=0.65			6.3 $(rad/s)^2$	
X=0.7			6.5 $(rad/s)^2$	
	Germanium site (quartenary)		Boron tetrahedral site (quartenary)	
Z=0.1; x=0.55	8.1$(rad/s)^2$ $\pm$0.5 $(rad/s)^2$		5.5 $(rad/s)^2$ $\pm$0.75 $(rad/s)^2$	
Z=0.2; x=0.55	8.1 $(rad/s)^2$ $\pm$0.5 $(rad/s)^2$		5.5 $(rad/s)^2$ $\pm$0.75 $(rad/s)^2$	
Z=0.3; x=0.55	8.1$(rad/s)^2$ $\pm$0.5 $(rad/s)^2$		5.5 $(rad/s)^2$ $\pm$0.75 $(rad/s)^2$	

Table 4-5 Percolation fraction values used in fitting data with the DAE model.

Sample	Percolation fraction	ΔE_p	Average Activation Energy, ΔE_m
Z=0.0; x=0.45	0.404	4680 K	3957 K (0.33 eV)
Z=0.0; x=0.55	0.404	4460 K	3762 K (0.32 eV)
Z=0.1; x=0.55	0.312	4140 K	3604 K (0.31 eV)
Z=0.2; x=0.55	0.324	4060 K	3525 K (0.30 eV)
Z=0.3; x=0.55	0.352	4060 K	3525 K (0.30 eV)

Table 4-6 Parameters used for the Ion Trapping Model in zLiI + (1-z)[xLi_2S + (1-x)(0.5B_2S_3+0.5GeS_2)] glasses.

Sample	Index of refraction	λ_0	Average activation energy, ΔE_m	Distribution width, ΔE_b
Z=0.0; x=0.45	1.4	6.106 nm	5300 K (0.451 eV)	465 K
Z=0.0; x=0.55	1.55	5.039 nm	4870 K (0.415 eV)	415 K
Z=0.1; x=0.55	1.4	5.604 nm	4818 K (0.410 eV)	475 K
Z=0.2; x=0.55	1.4	5.496 nm	4750 K (0.405 eV)	475 K
Z=0.3; x=0.55	1.5	6.522 nm	4670 K (0.398 eV)	450 K

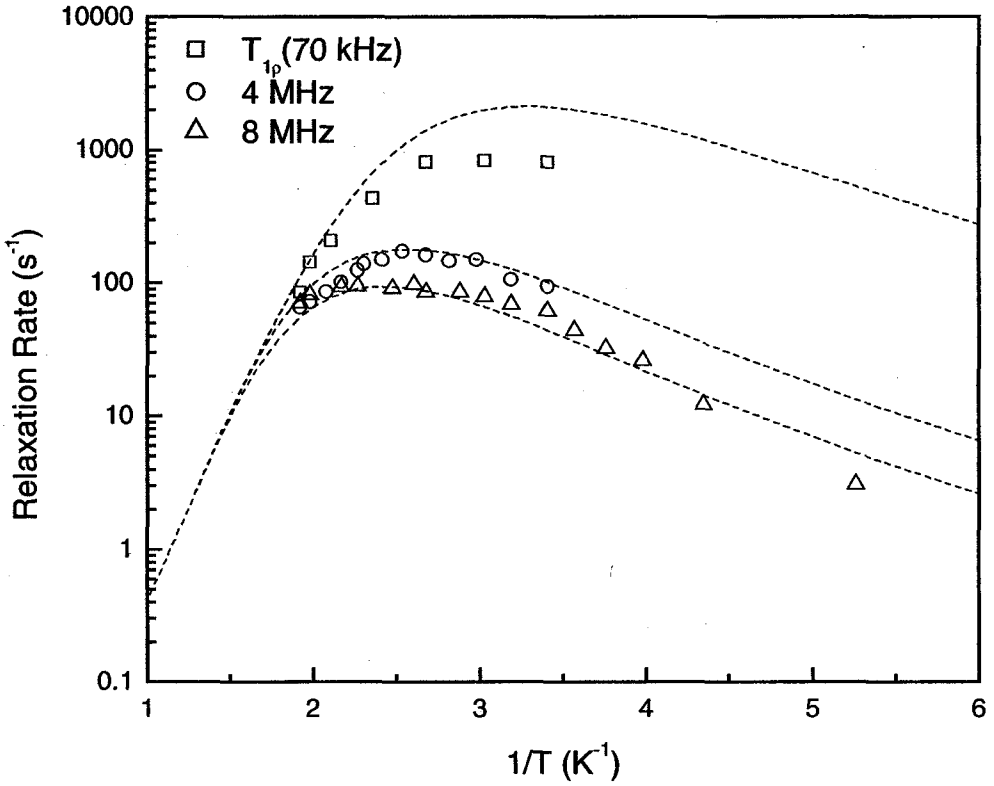

Figure 4.1 Fit of single DAE to R_1 data for $0.55Li_2S + (0.45)(0.5B_2S_3+0.5GeS_2)$ glass.

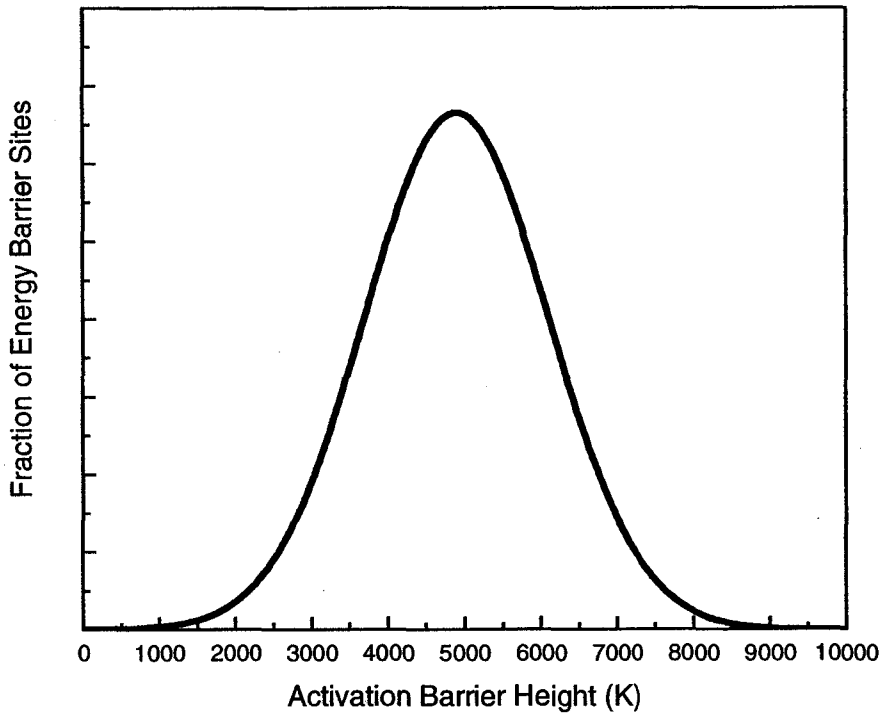

Figure 4.2 Single DAE for $0.55Li_2S + (0.45)(0.5B_2S_3+0.5GeS_2)$] as determined from the fit of the R_1 data.

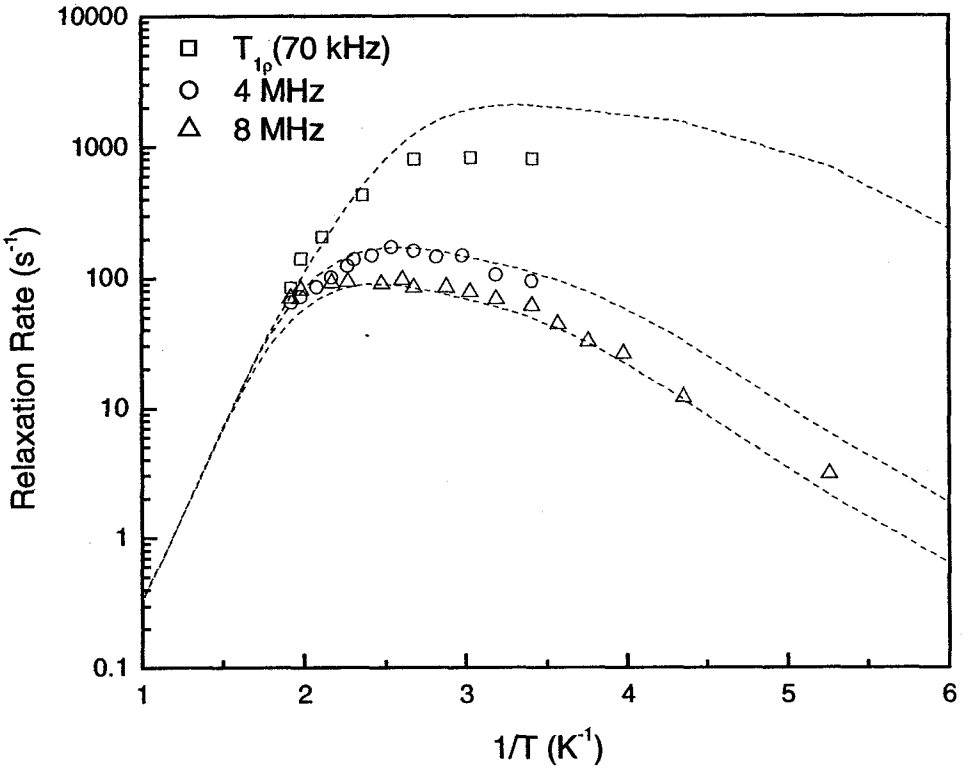

Figure 4.3 NSLR measurement and fit using two Gaussian DAEs, one for Li^+ ions in boron sites and another for Li^+ ions in Ge sites.

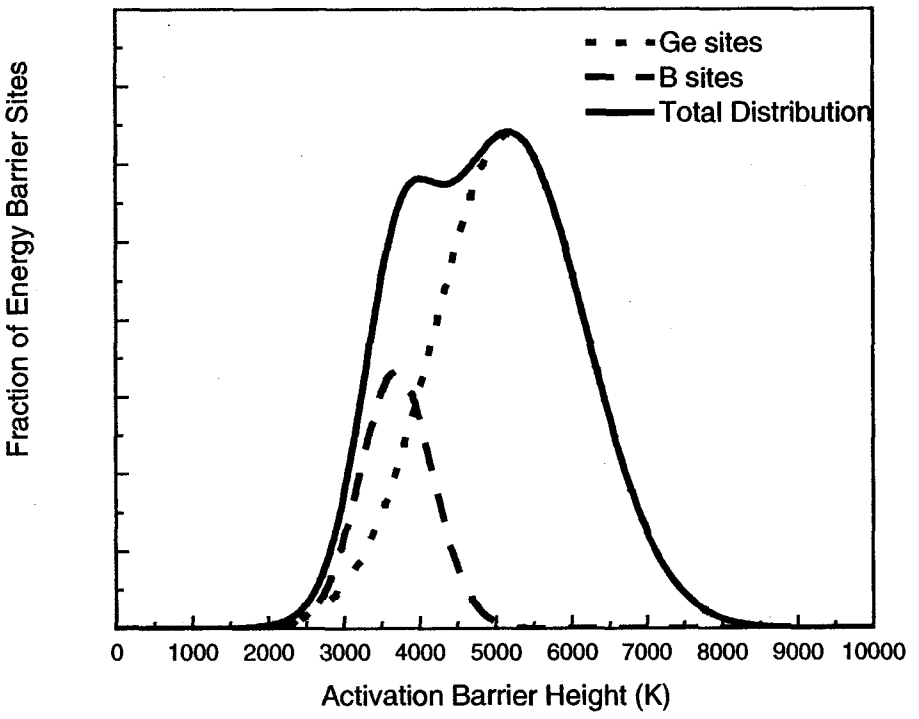

Figure 4.4 Total DAE using two separate Guassian DAEs in $0.55Li_2S + (0.45)(0.5B_2S_3+0.5GeS_2)$.

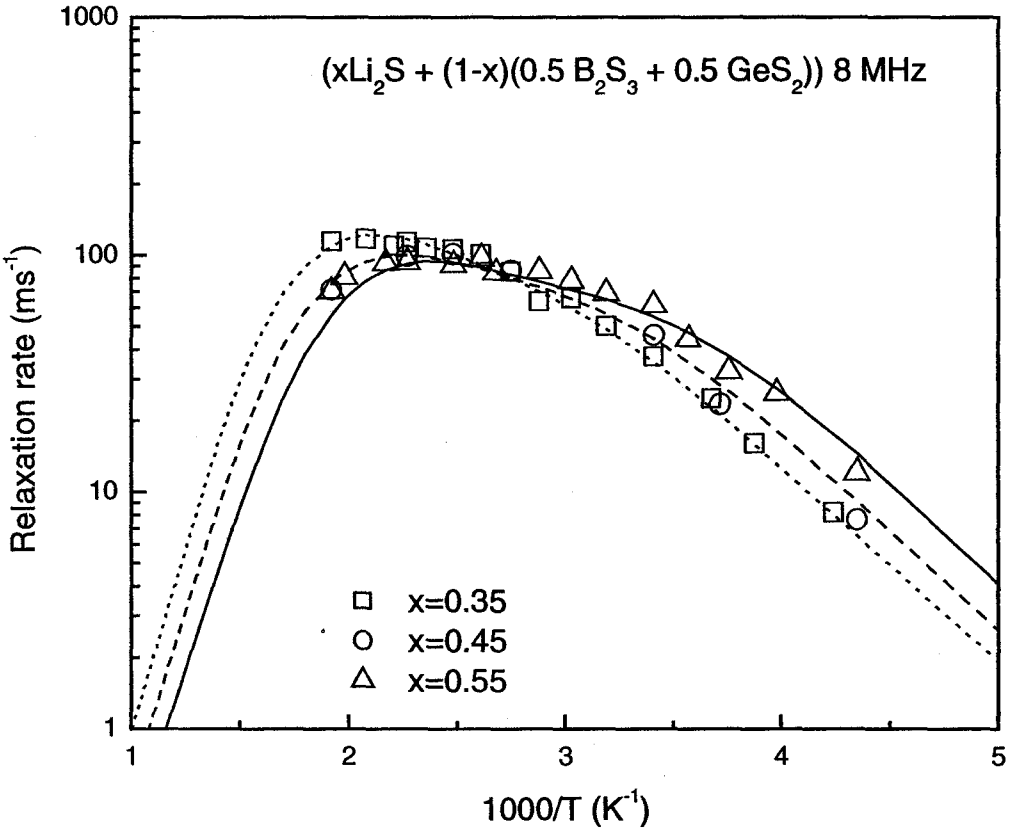

Figure 4.5 DAE fits to NSLR data for x=0.35, 0.45 and 0.55 ternary glasses.

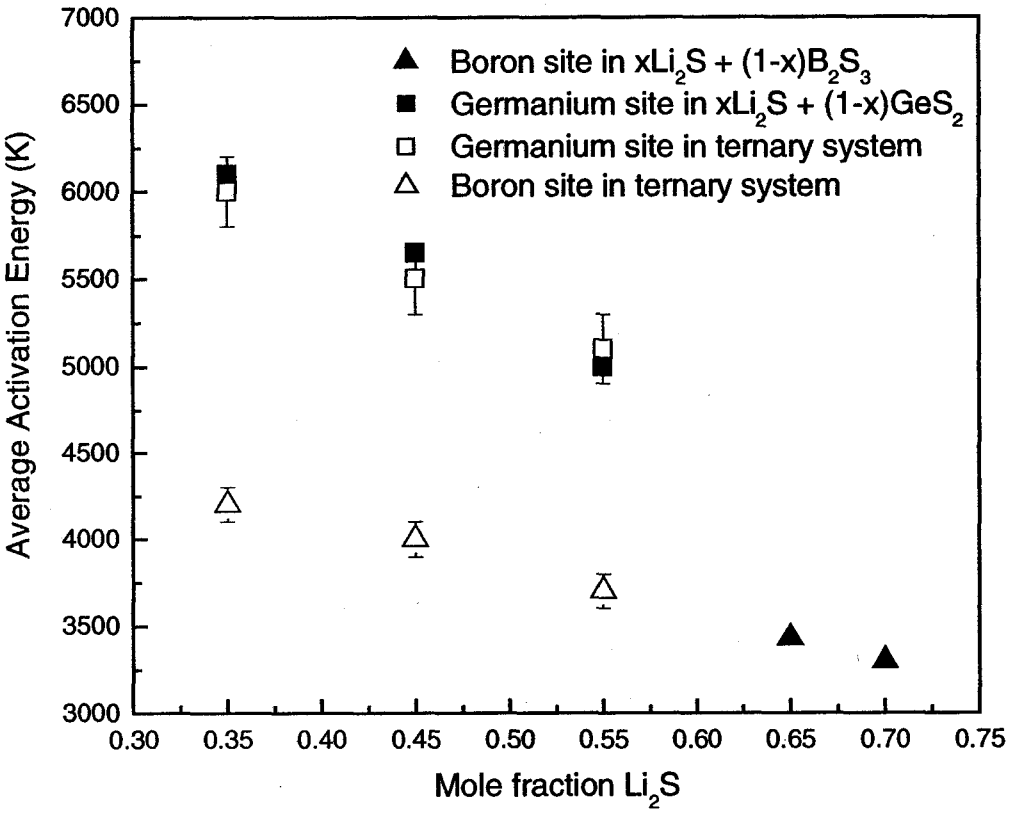

Figure 4.6 Average activation energies determined by NSLR measurements and DAE fits.

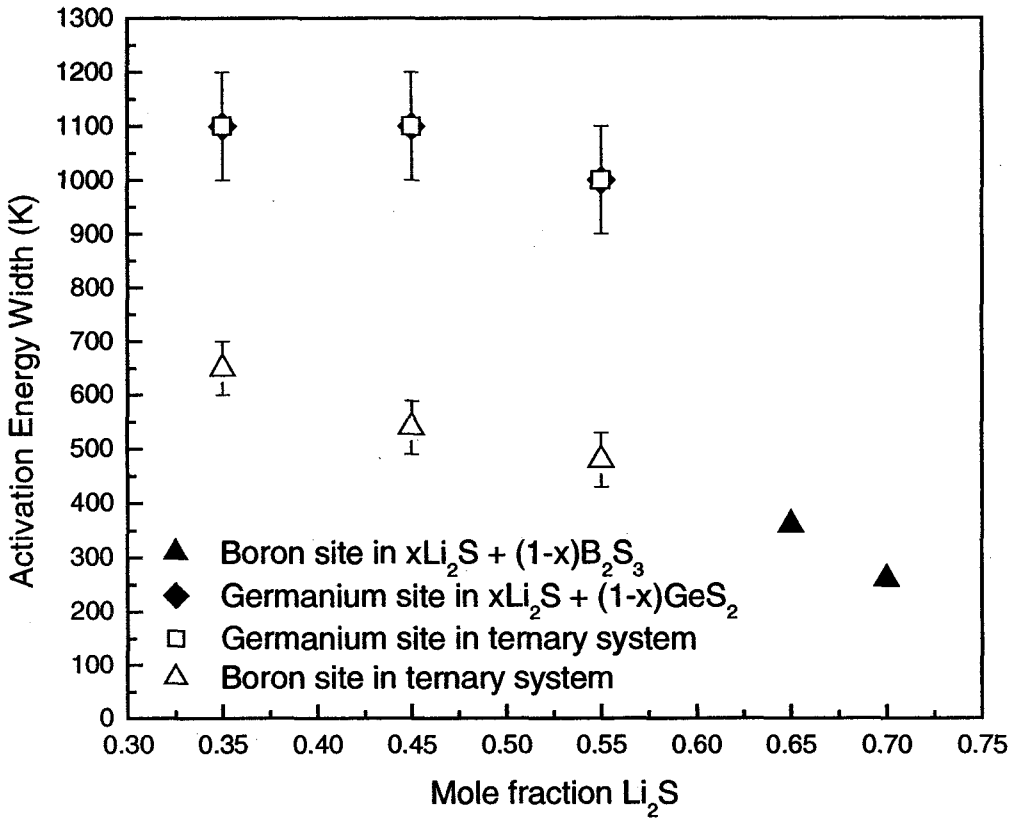

Figure 4.7 Distribution widths determined by NSLR measurements and DAE fit and compared to the values obtained for lithium thio-borate and lithium thio-germanate binary glasses.

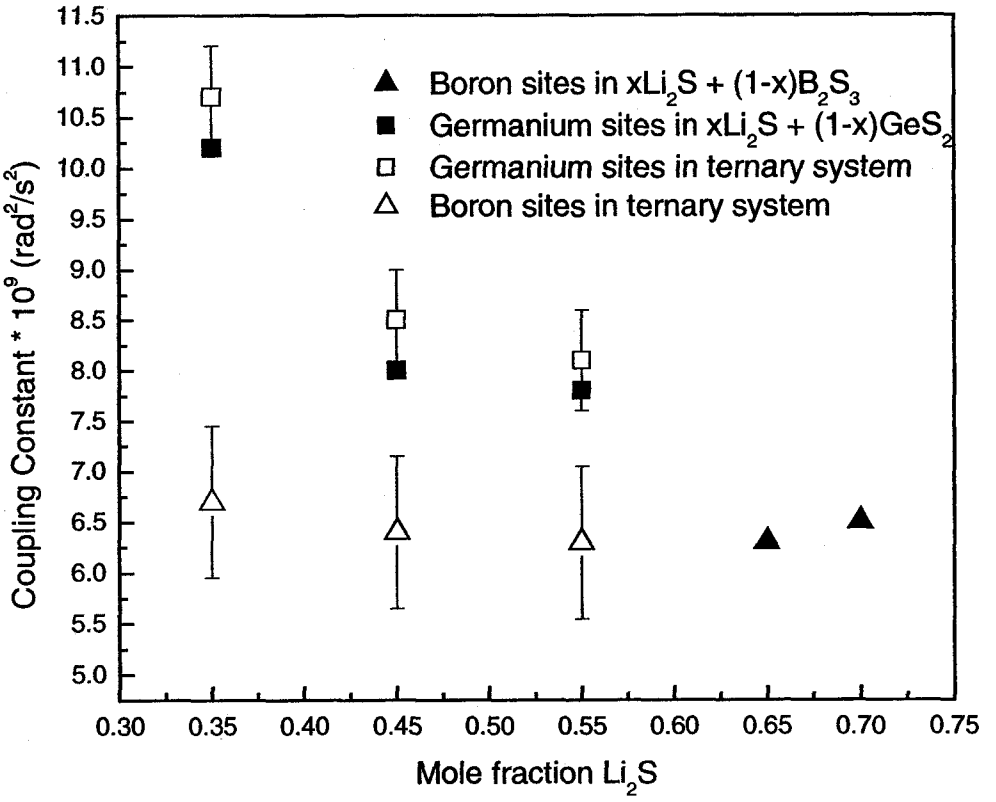

Figure 4.8 Coupling constants determined by NSLR measurements and DAE fit and compared to the values obtained for lithium thio-borate and lithium thio-germanate binary glasses.

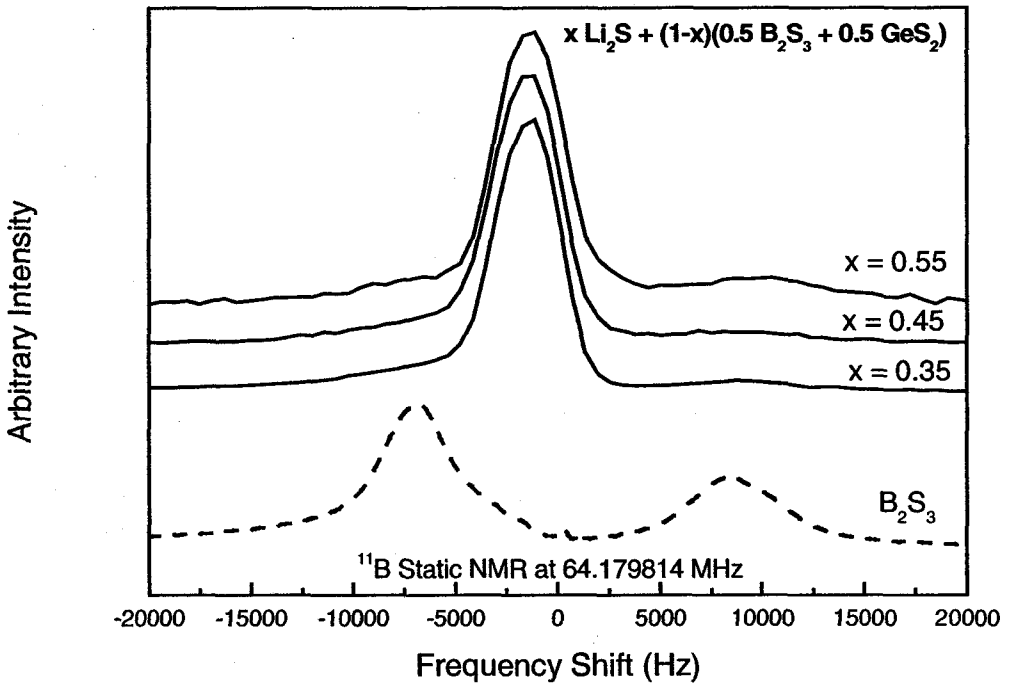

Figure 4.9 Static ^{11}B NMR spectra showing comparison of samples to pure B_2S_3.

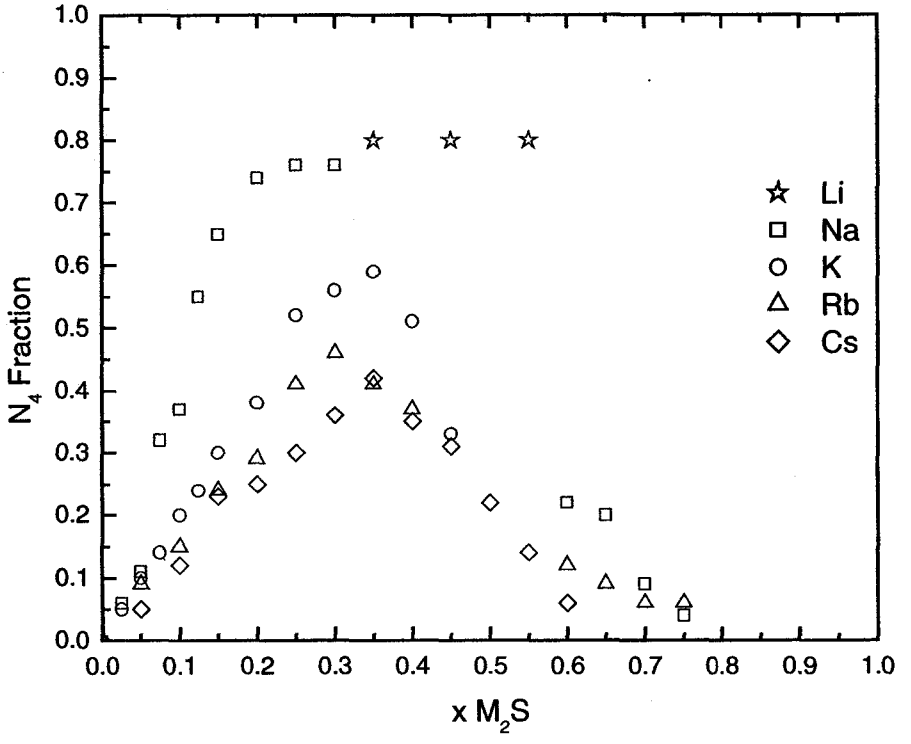

Figure 4.10 Fraction of tetrahedral boron atoms present as a function of M_2S content.

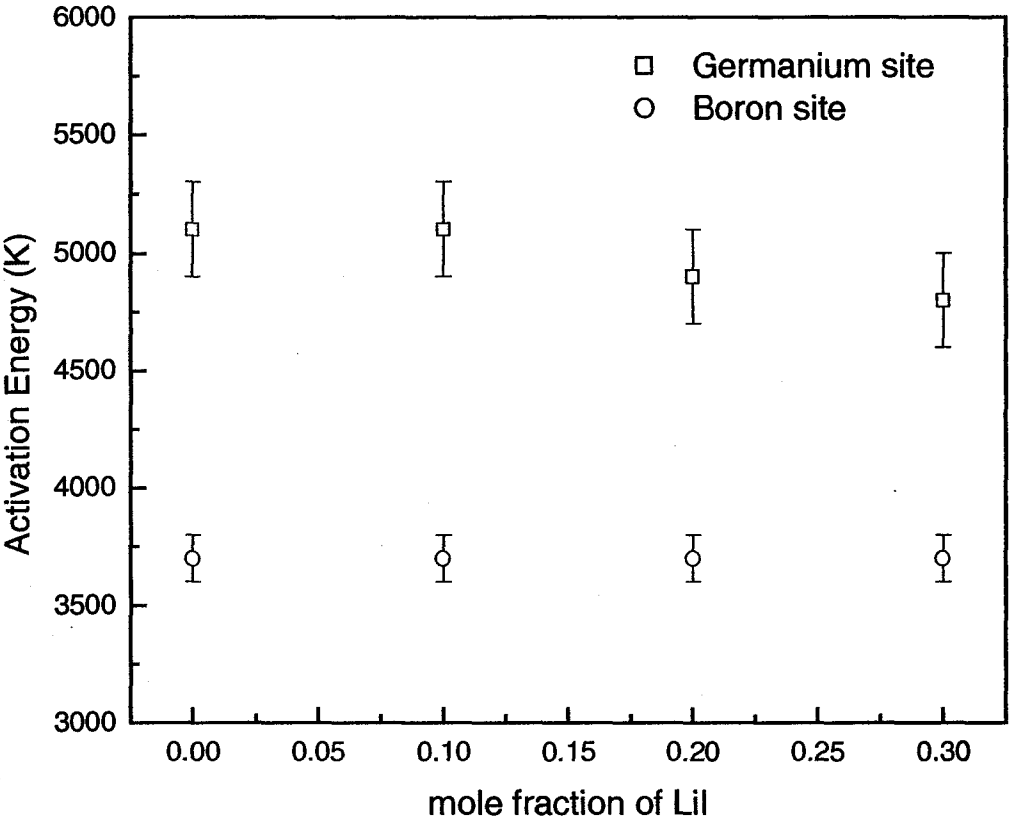

Figure 4.11 Average activation energies, ΔE_m, for zLiI + (1-z)[0.55Li_2S + (0.45)(0.5B_2S_3+0.5GeS_2)]

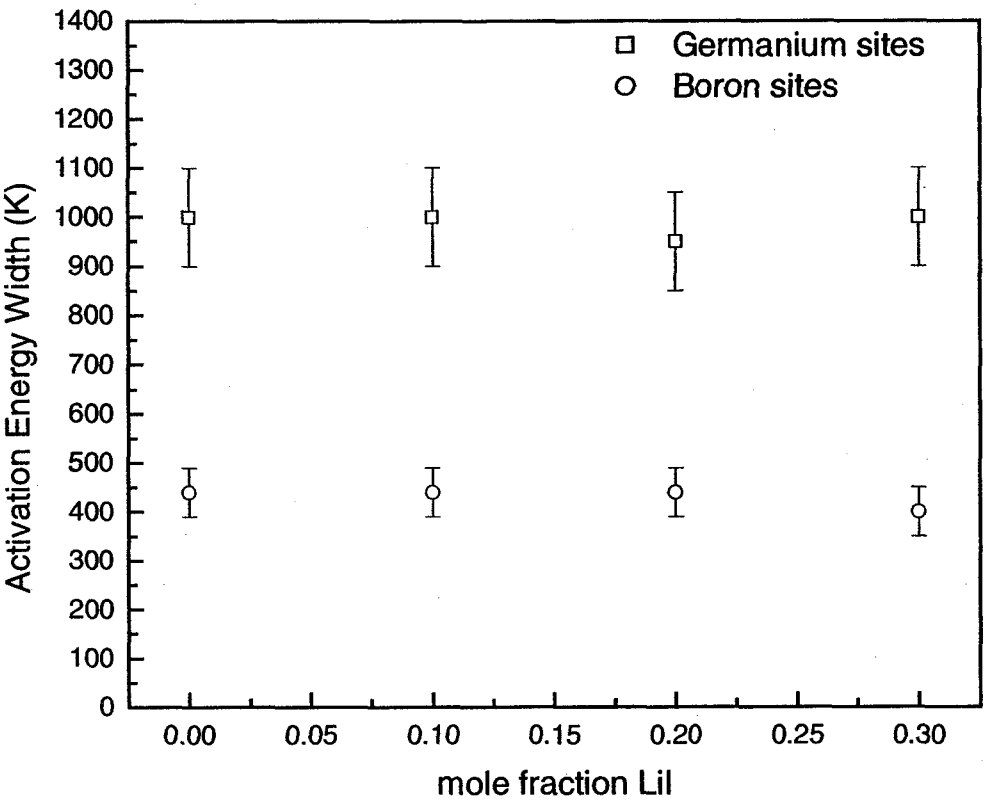

Figure 4.12 Distribution widths, ΔE_b, determined from NSLR measurements using DAE fits for $zLiI + (1-z)[0.55Li_2S + (0.45)(0.5B_2S_3+0.5GeS_2)]$.

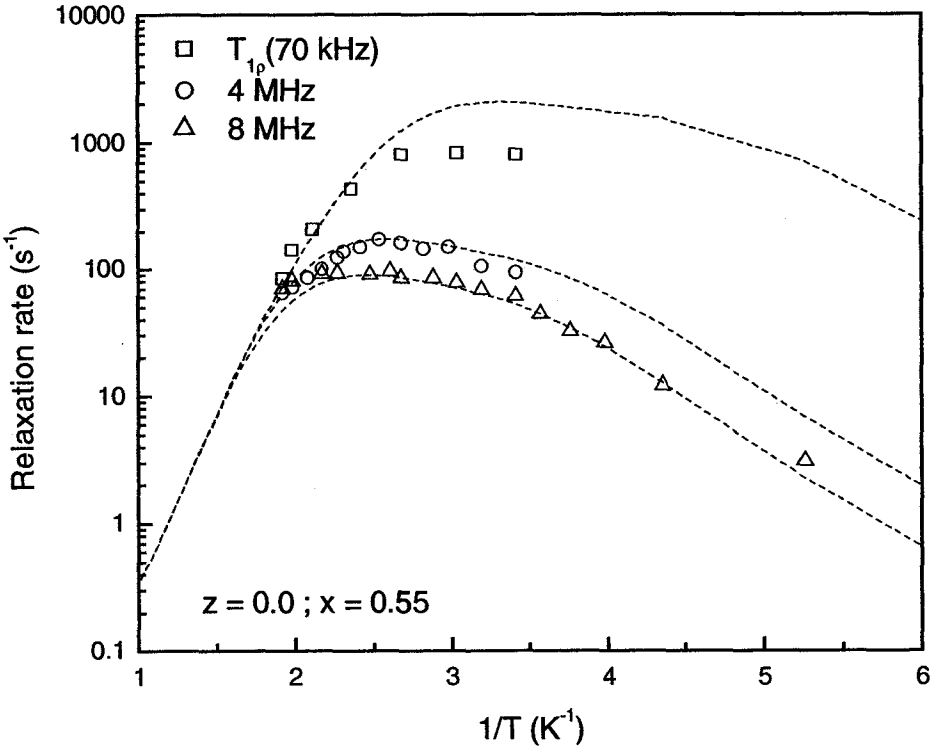

Figure 4.13 NSLR rates for $0.55Li_2S + 0.45(0.5B_2S_3+0.5GeS_2)$ glass.

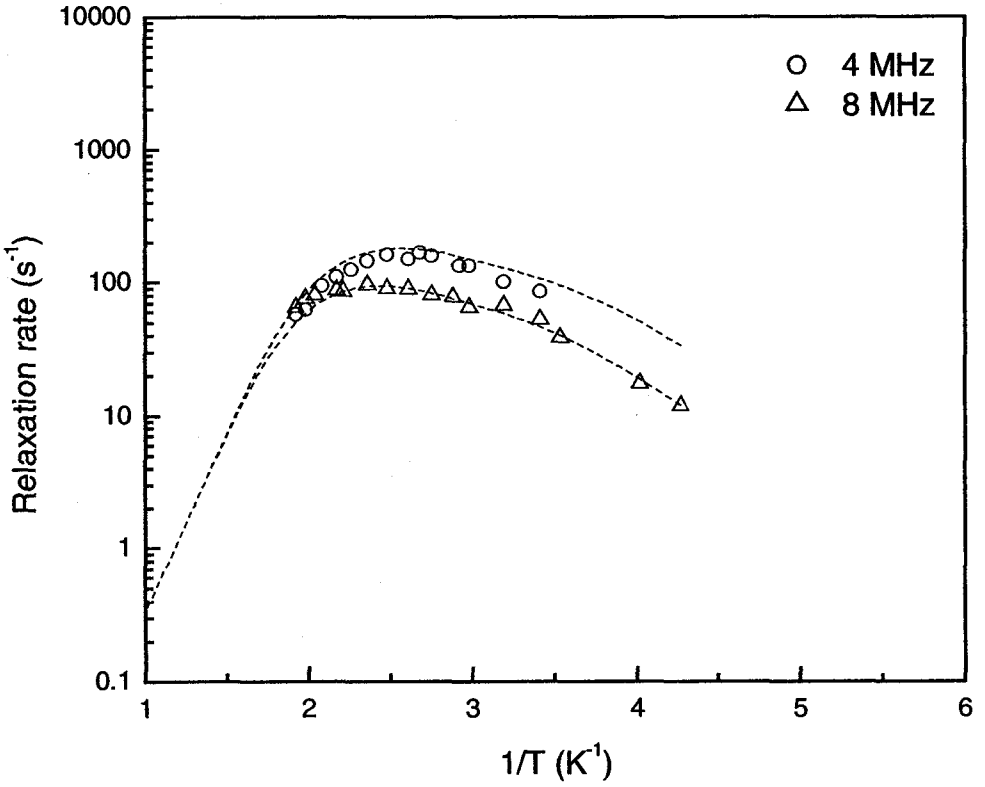

Figure 4.14 NSLR rates for $0.1LiI + 0.9[0.55Li_2S + 0.45(0.5B_2S_3+0.5GeS_2)]$

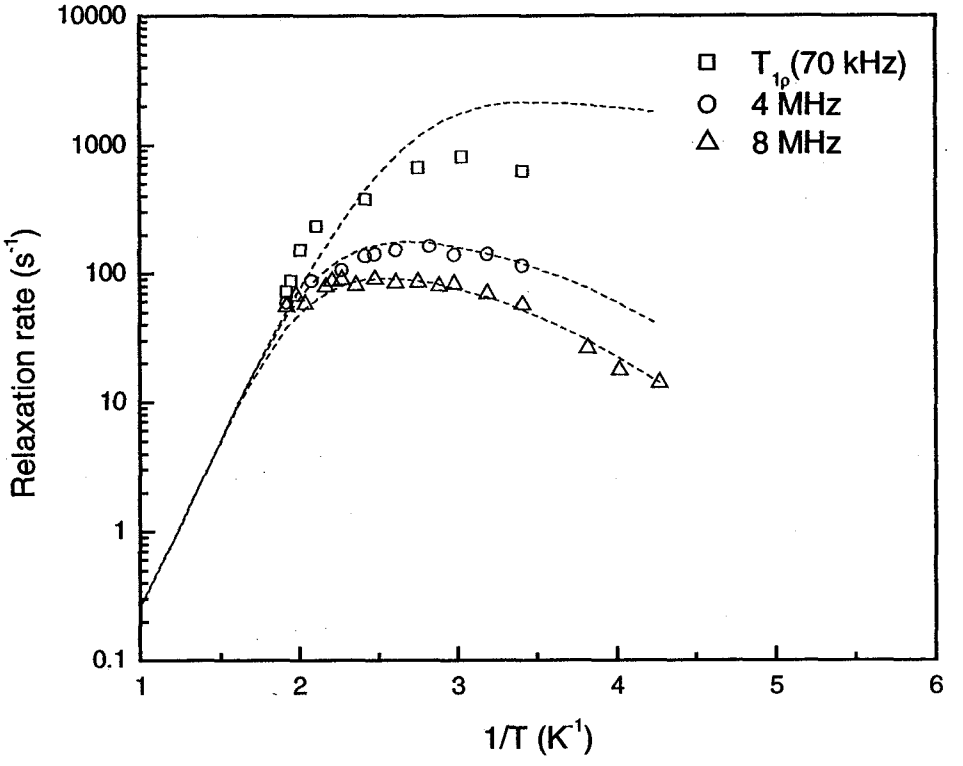

Figure 4.15 NSLR rates for 0.2LiI + 0.8[0.55Li_2S + 0.45(0.5B_2S_3+0.5GeS_2)]

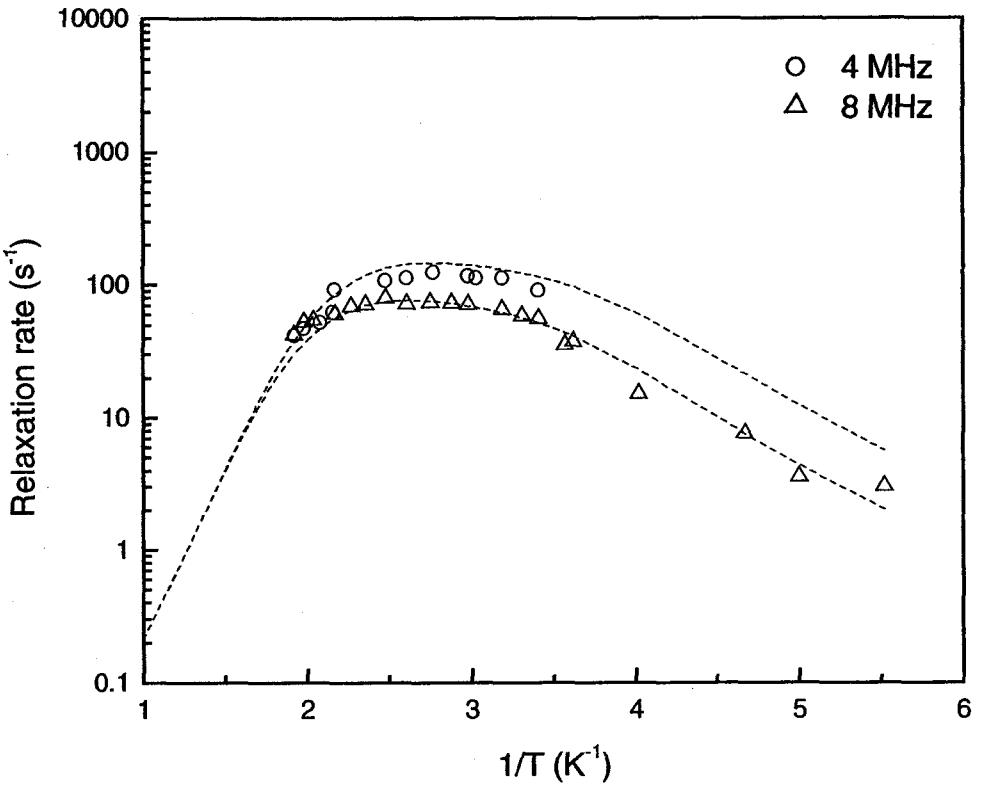

Figure 4.16 NSLR rates for 0.3LiI + 0.7[0.55Li_2S + 0.45(0.5B_2S_3+0.5GeS_2)]

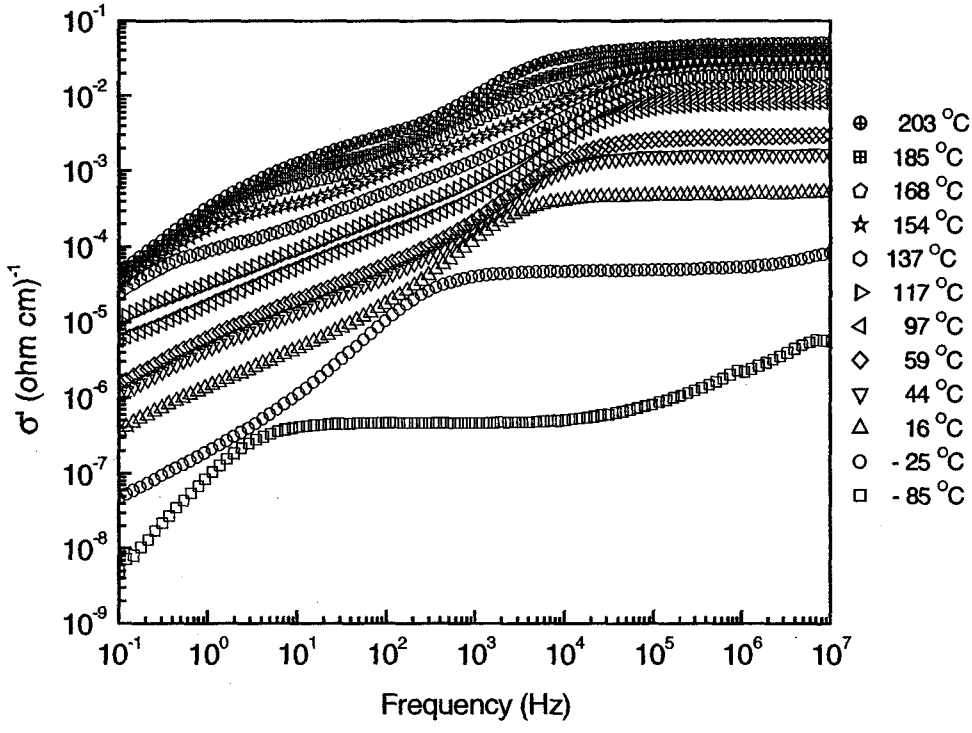

Figure 4.17 Real part of a.c. conductivity for $0.2LiI + 0.8[0.55Li_2S + 0.45(0.5B_2S_3+0.5GeS_2)]$

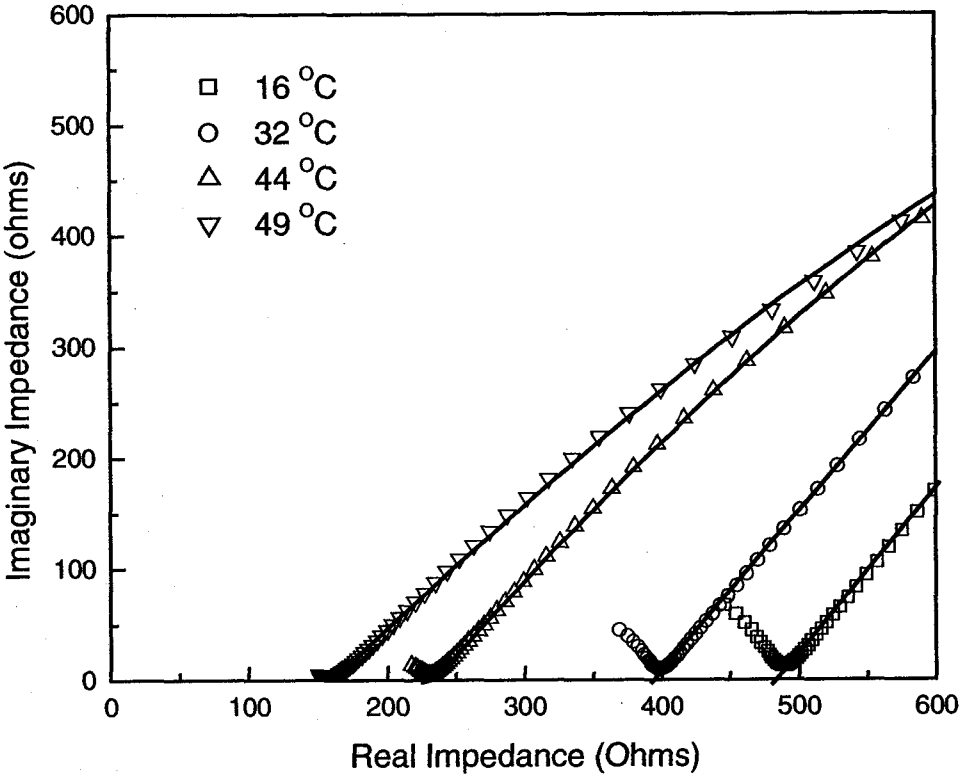

Figure 4.18 Nyquist plot for 0.2LiI + 0.8[0.55Li_2S + 0.45(0.5B_2S_3+0.5GeS_2)]

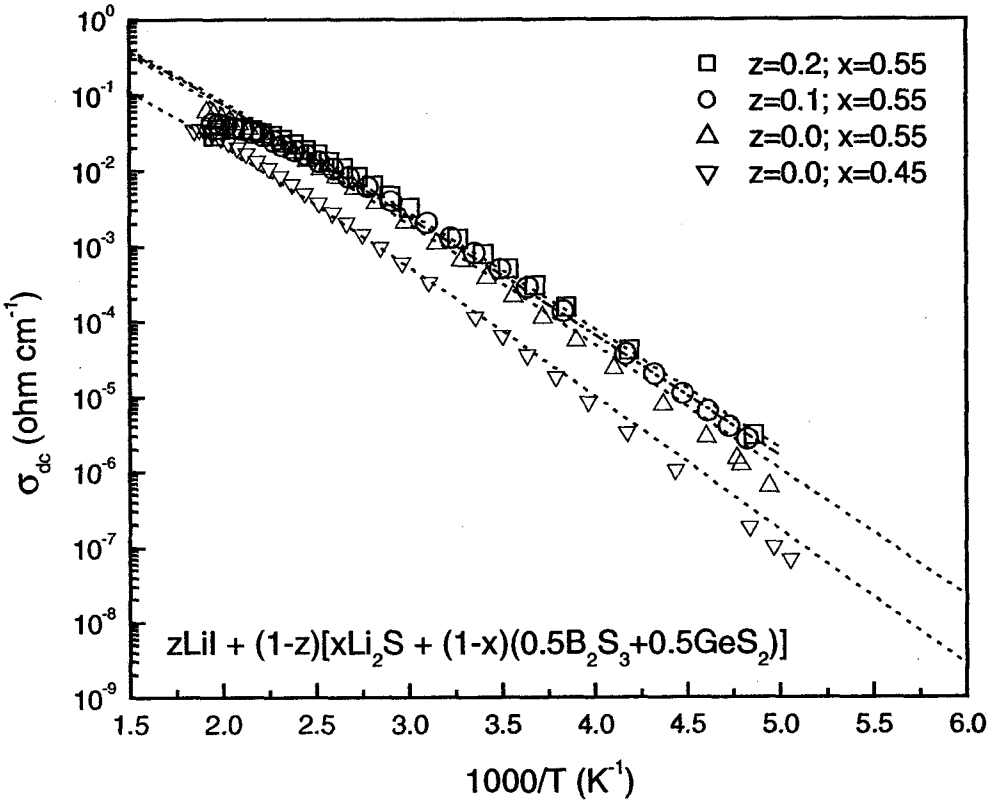

Figure 4.19 D.C. conductivities of ternary zLiI + (1-z)[xLi_2S + (1-x)(0.5 B_2S_3 + 0.5 GeS_2)] glass samples and fits determined by the DAE.

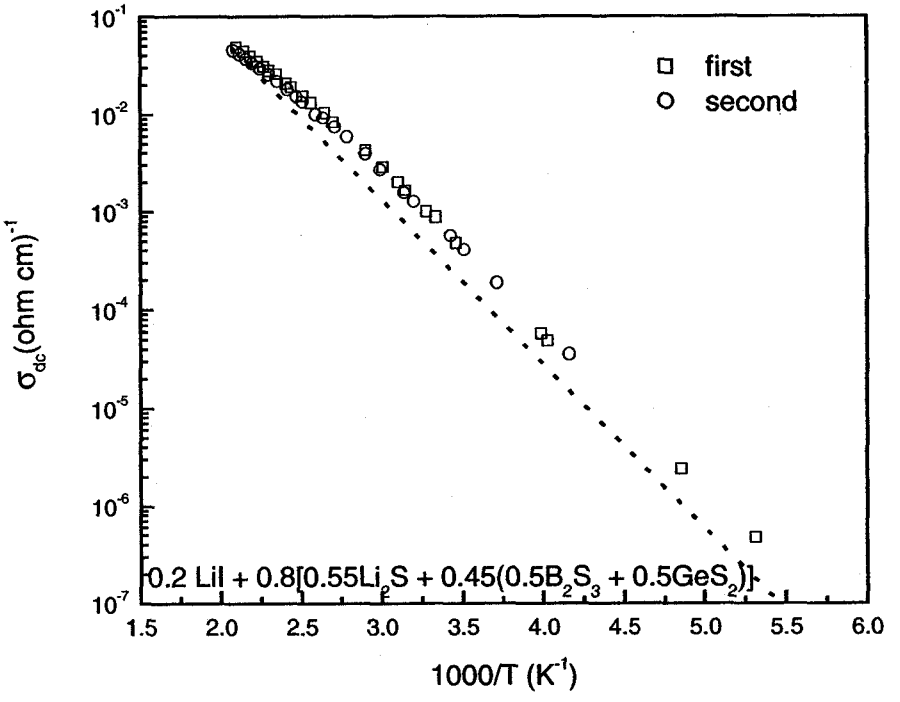

Figure 4.20 Arrhenius plot showing two consecutive temperature scans of the d.c. conductivity for the same sample.

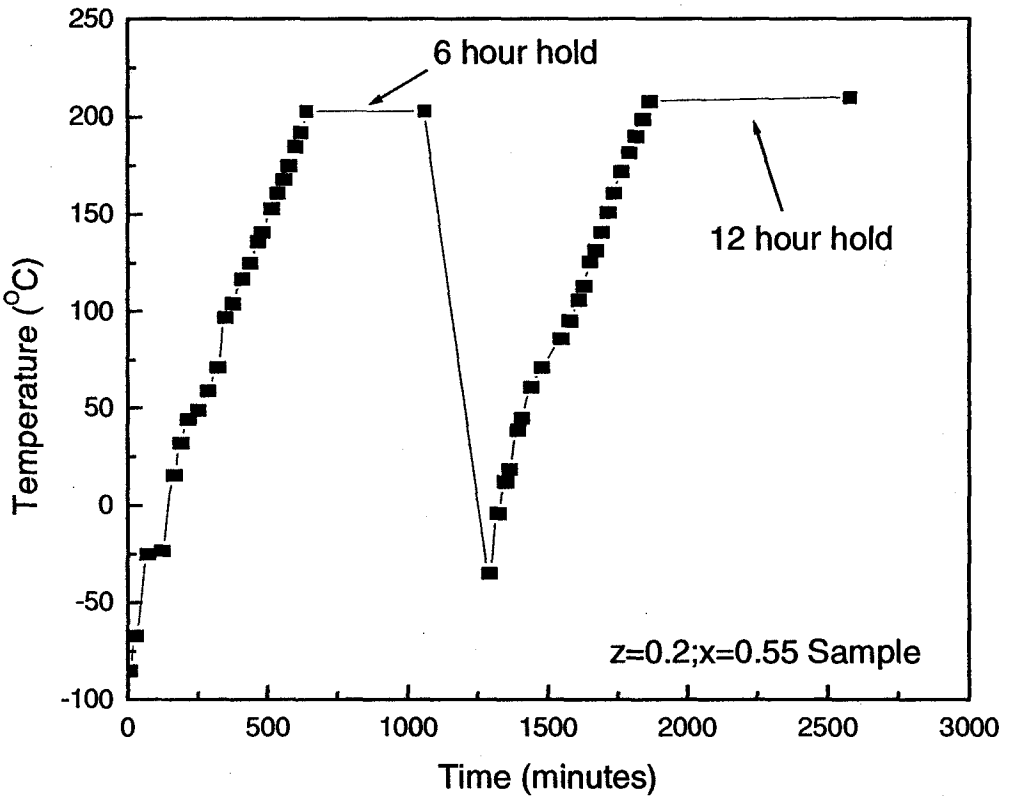

Figure 4.21 Temperature profile of the z=0.2;x=0.55 glass sample in which two consecutive d.c. conductivity measurements were performed.

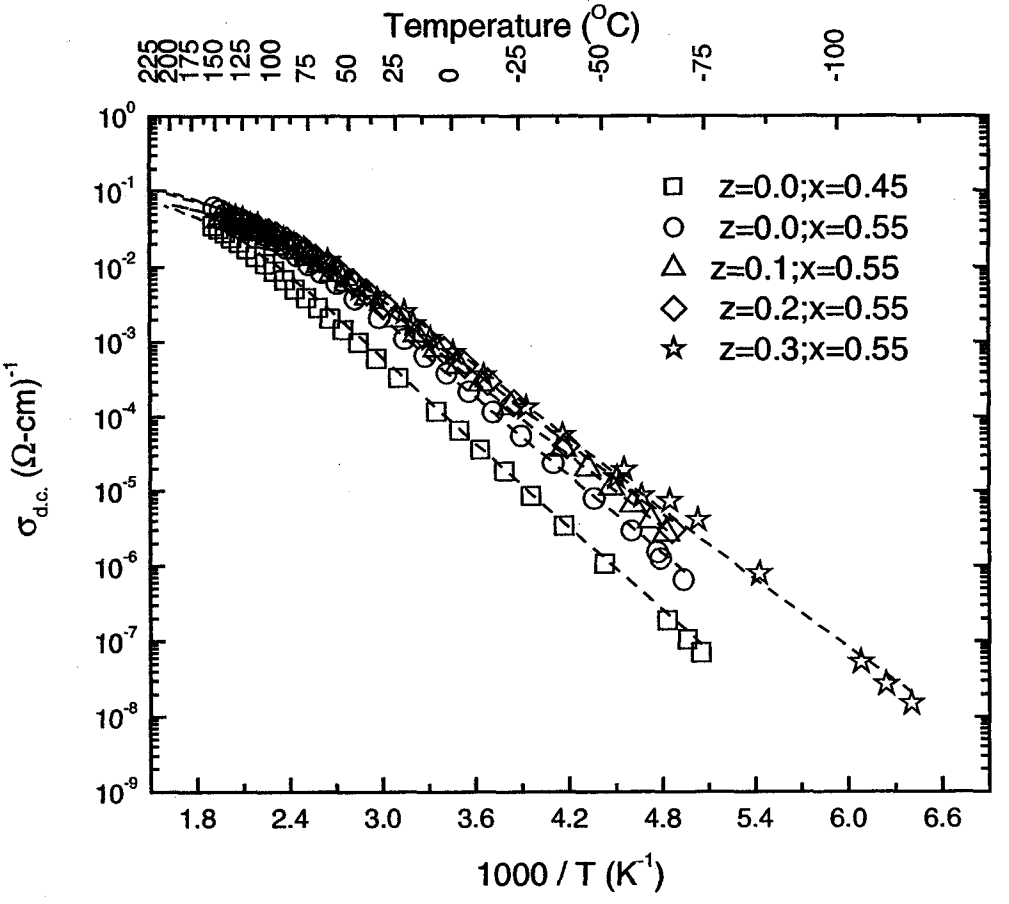

Figure 4.22 Arrhenius plot of the d.c. conductivities with dashed lines representing fits from the ITM in $zLiI + (1-z)[xLi_2S + (1-x)(0.5B_2S_3+0.5GeS_2)]$ glasses.

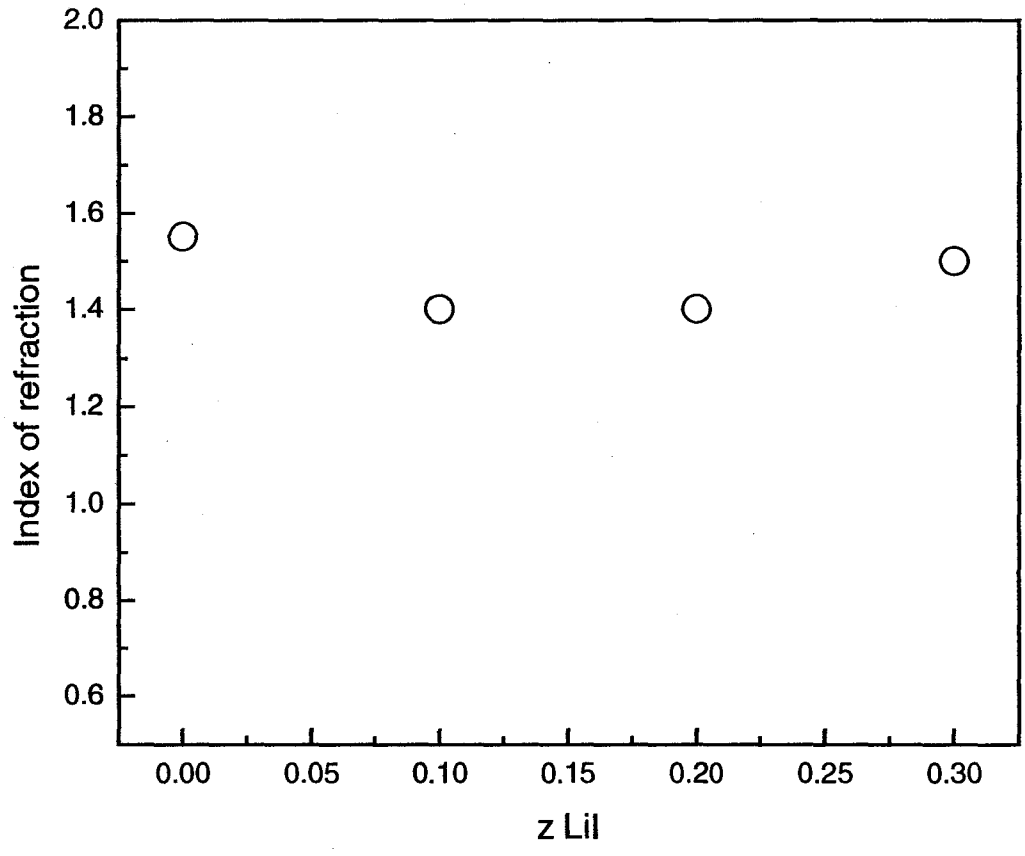

Figure 4.23 Index of refraction values used for fitting with ITM for zLiI + (1-z)[0.55 Li_2S + (0.45)(0.5B_2S_3+0.5GeS_2)] glasses.

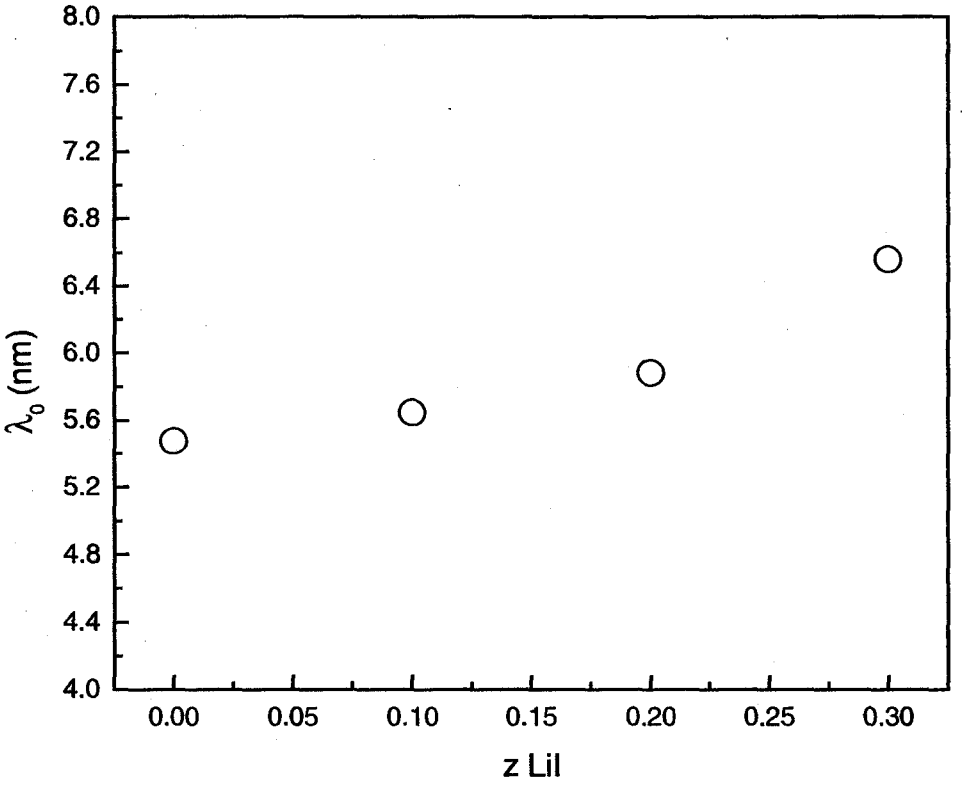

Figure 4.24 λ_0 values calculated at Tg for zLiI + (1-z)[0.55 Li_2S + (0.45)(0.5B_2S_3+0.5GeS_2)] glasses.

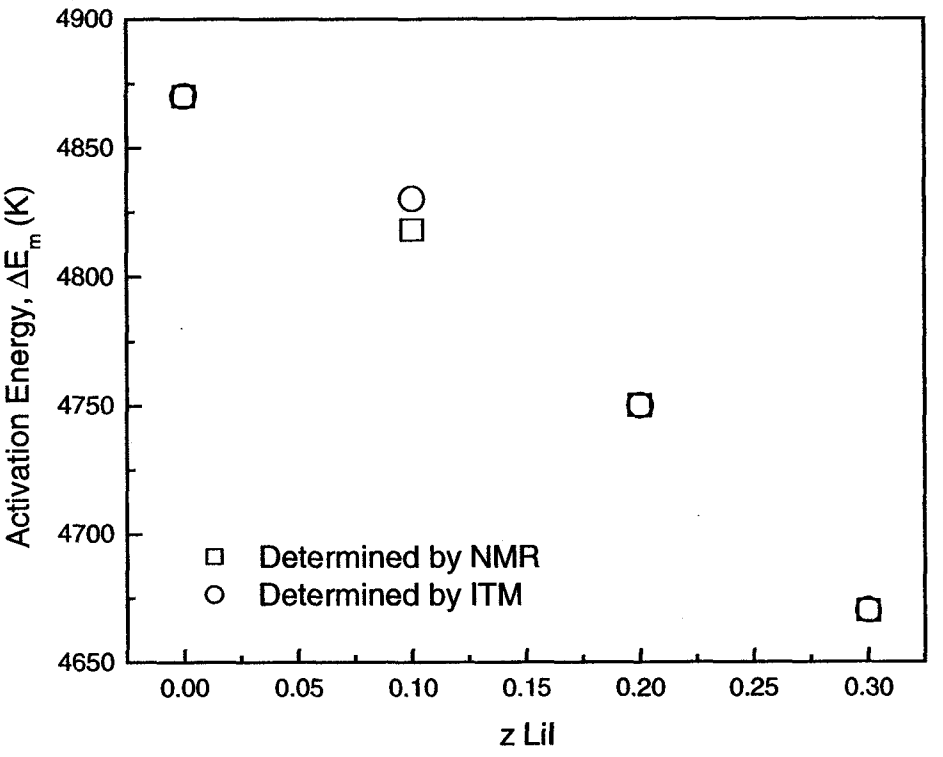

Figure 4.25 Plot showing excellent agreement between the activation energies used for the ITM and the NMR determined values in zLiI + (1-z)[0.55 Li_2S + (0.45)(0.5B_2S_3+0.5GeS_2)].

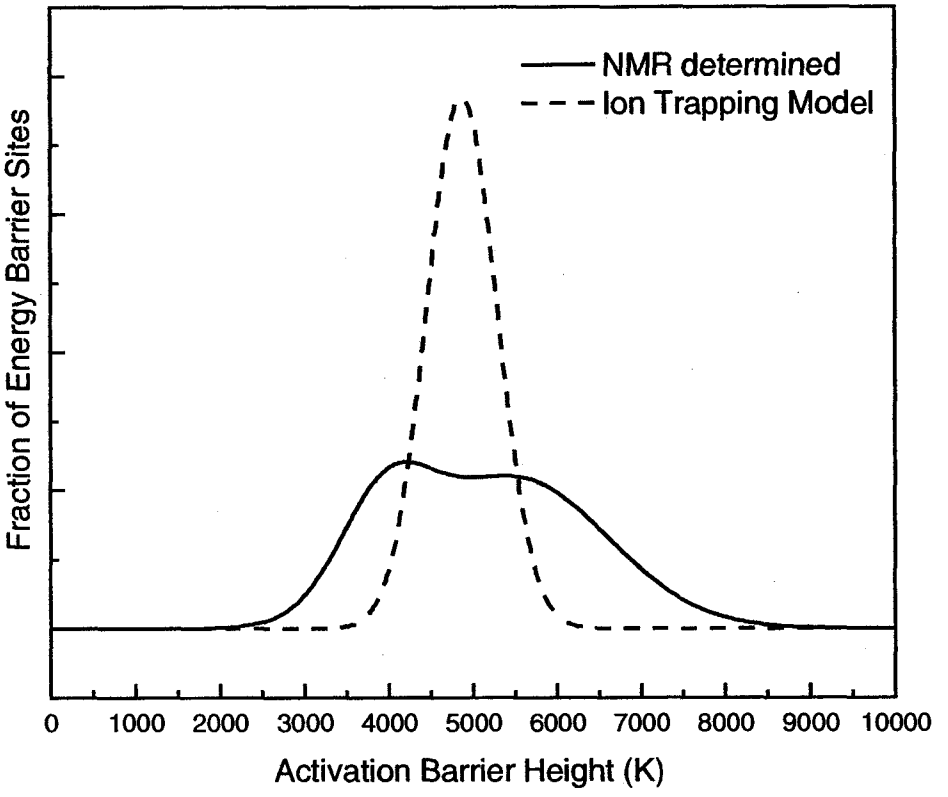

Figure 4.26 Comparison between the NMR determined DAE and the DAE needed for fitting with the ITM in 0.2LiI + (0.8)[0.55 Li_2S + (0.45)(0.5B_2S_3+0.5GeS_2)] glass.

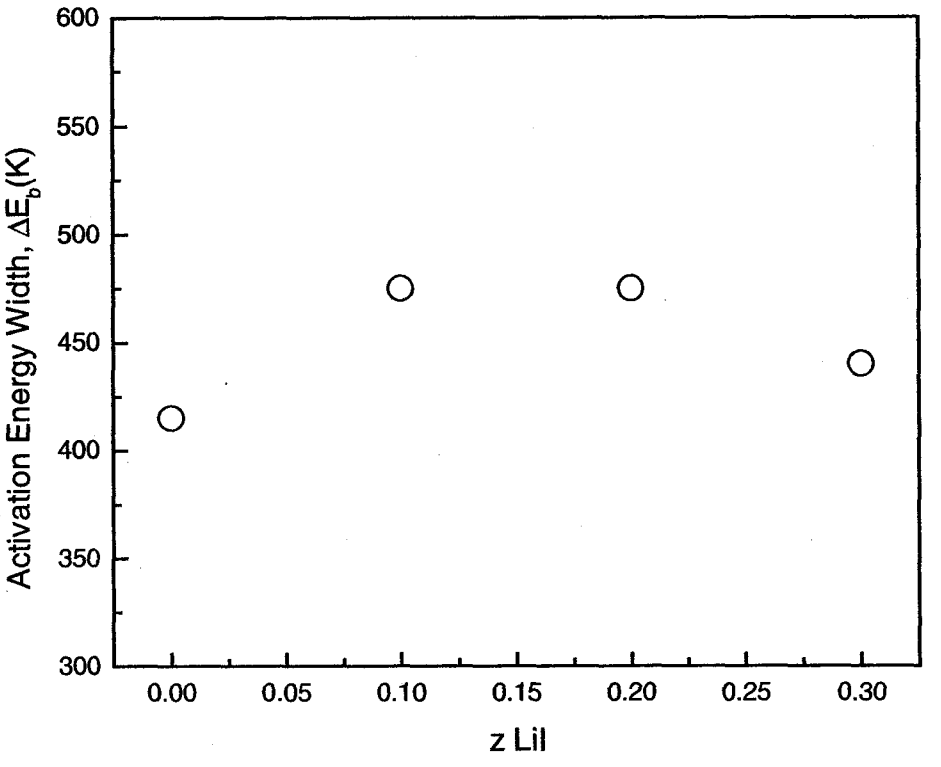

Figure 4.27 Values used for the width of the DAE used in the ITM in zLiI + (1-z)[0.55 Li_2S + (0.45)(0.5B_2S_3+0.5GeS_2)] glasses.

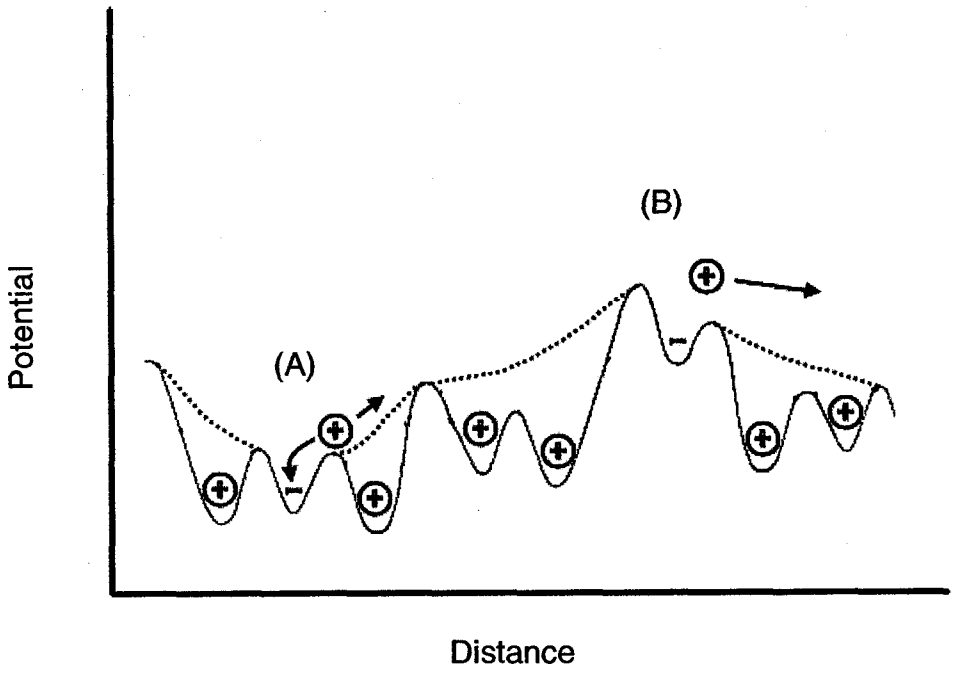

Figure 4.28 Possible energy landscape for highly modified FIC glasses.

4.7 References

[1] H.L. Tuller, M. Balkanski. Science and Technology of Fast Ion Conductors, NATO ASI Series B: Physics **199** (1989).
[2] Kincs, J., Martin, S. W., Phys. Rev. Let., **76**, 70-73 (1996)
[3] Svare, I. Solid State Ionics **125**(1-4), 47-53 (1999).
[4] C.A. Angel, Solid State Ionics **105**, 15 (1998).
[5] S.W. Martin, D.Martin, J. Schrooten, B. Meyer. Submitted to Journal of Physics: Condensed Matter.
[6] Martin, S. W., Bloyer, d., J. Am. Ceram. Soc., **74**, 1003 (1991).
[7] P. Tipler, Physics. Worth Publishers, Inc. New York, NY (1982), 378-381.
[8] J.Schrooten, Ph.D. Dissertation, Iowa State University, Ames, IA (2001).
[9] D.J. Adduci, B.C. Gerstein, Rev. Sci. Instrum. **50**, 1403 (1979).
[10] D.J. Adduci, P.A. Hornung, D.R. Torgeson, Rev. Sci. Instrum. **47**, 1503 (1976).
[11] C.P.Slichter. Principles of Magnetic Resonance. Springer-Verlag. New York (1980) 214-215.
[12] Kim, K. H.; Torgeson, D. R.; Borsa, F.; Cho, J. P.; Martin, S. W.; Svare, I.; Majer, G. Journal of Non-Crystalline Solids **211**(1,2), 112-125 (1997).
[13] K.L Ngai, Phys. Rev. B **48**, 13481 (1993).
[14] J. Macdonald, Journal of Applied Physics **84**, 812 (1998).
[15] K. H. Kim, D. R. Torgeson, F. Borsa, J. Cho, S. W. Martin, I. Savre. Solid State Ionics **91**, 7–19 (1996).
[16] I. Savre, F. Borsa, D.R. Torgeson and S.W. Martin. Phys. Rev. B **48**, 9336 (1993).
[17] R. Hogg, Probability and Statistical Inference. Prentice Hall, Englewood Cliffs, New Jersey (1988) 224.
[18] S.R. Elliot. *Physics of Amorphous Materials*. Longman. New York. 299 (1990).
[19] R. Alberty, R. Silbey, Physical Chemistry, John Wiley & Sons, Inc. New York, NY (1992) 595-616
[20] N.F. Mott, Journal of Non-Crystalline Solids. 1, 1-17 (1968).
[21] Eros et al. Electronic properties of doped semiconductors. Springer-Verlag, Berin (1984).
[22] K.H. Kim et al. Solid State Ionics **91**, 7-19 (1996) 7-19.
[23] I.Savre, F. borsa, D.R. Torgeson, and S.W. Martin, Phys Rev. B 48 (1993) 9336; J. Non-Cryst. Solids **172**, 1300 (1994).
[24] M. Tatsumisago, C.A. Angell and S.W. Martin, J. Chem. Phys. **97**, 6968 (1992).
[25] N. Bloembergen, E.M. Purcell and R.V. Pound, Phys. Rev. **73**, 679 (1948).
[26] Kim, K. H.; Torgeson, D. R.; Borsa, F.; Martin, S. W. Solid State Ionics **90**(1-4), 29-38 (1996).
[27] Meyer, B, Martin, S.W., To be published.
[28] Schrooten, J., Meyer, B., Martin, S.W., Submitted to Physical Review B: Condensed Matter Physics, Nov. 2001
[29] J. Schrooten, B. Meyer, S.W. Martin. Submitted to Journal of Non-Cryst. Solids
[30] H. Takahashi, K. shishitsuka, T.Sakuma, Y. Shimojo, Y. Ishii. Solid State Ionics **113-115**, 685-690 (1998)

[31] Bunde, Armin; Funke, Klaus; Ingram, Malcolm D. Solid State Ionics **86-88**(Pt. 2), 1311-1317 (1996).
[32] T. Akai, S.W. Martin, F. Borsa, Physical Review B **63**, 024303 (2000).
[33] A. Matic, J.Swenson, L. Borjesson, S. Longeville, R. Lechner, W. S. Howells, T. Akai, and S.W. Martin, Physica B **226**, 69 (1999).
[34] Q. Mei, Ph.D. Dissertation, Iowa State University, Ames, IA (2003)

CHAPTER 5 GENERAL CONCLUSIONS

5.1 Summary

In an effort to gain a better understanding of the origins of non-Arrhenius behavior seen in many fast ion conducting systems, many steps have been made to further the understanding of the phenomena. First, it has been shown that non-Arrhenius behavior also occurs in Lithium fast ion conducting systems. A repeatability test had been performed which shows that a bulk phenomenon does contribute significantly to the non-Arrhenius behavior observed in these systems. While oxidation and / electrode reaction can contribute, with great caution these effects can be avoided.

IR and Raman show qualitatively that a large number of lithium ions associate to germanium sites instead of tetrahedral boron sites. NSLR measurements have shown 70 to 80% of the ions reside with germanium sites. Using this information it has been possible to fit both the NMR and Arrhenius regions of the conductivity data very well using the distribution of activation energies model.

This study has also shown that no detectable deviation is seen in the NSLR data at temperatures where the non-Arrhenius behavior occurs in the conductivity measurements. The ion trapping model has been developed which very accurately fits both the Arrhenius and non-Arrhenius regions of the conductivity for all of the samples. This model provides insight into the origins of the non-Arrhenius behavior and some insight to possibly why no deviation is seen in the NSLR curves.

Even with the progressive steps made, there are still many aspects of the ion trapping model and this research that need to be addressed.

5.2 Future Investigations

Many questions remain unanswered about the nature of the non-Arrhenius behavior seen in the d.c. conductivity. One of the first fundamentals questions to be explored is measurements of both the index of refraction and the relative permittivity at infinite frequency. The index of refraction could be measured by using matching indexing oils. It was be best to measure the relative permittivity using a high frequency a.c. bridge that can measure above 10 MHz.

Another fundamental question to be answered is what fraction of thermally activated ions actually contribute to the conductivity. This will be an important factor in helping to determine the origin of λ_0.

Finally, one of the biggest questions that remains, is the exact role the sulfur play in these samples. It would be very beneficial to confirm that three coordinate sulfurs do exist in helping to form the large macro-anion molecules which give rise a very high fraction of tetrahedral boron.

Unraveling these questions undoubtedly will increase our understanding of the non-Arrhenius behavior we see in the d.c. conductivity at higher temperatures.

APPENDIX A REPEATABILITY OF CONDUCTIVITY DATA

A.1 Introduction

Upon subsequent measurements of the conductivity, it was found in samples that exhibit the non-Arrhenius behavior for this family of Lithium glasses, the values of conductivity measured in a second temperature scan were significantly lower than the first scan. In some cases, this drop can be the result of an apparent transition which happens during the first run lowering the conductivity as much as an half of an order of magnitude. In the third run, points above 333 K were not plotted because it had become practically impossible to accurately determine the d.c. resistance point from the Cole-Cole plot due to the changing shape of the curves. At higher temperatures, there is a transition that occurs and resembles what would look like a crystallization event. The following tests were performed to try to quantify the temperature dependence of the effect and see if it has the same origin has the non-Arrhenius behavior.

A.2 Experimental

The following tests consisted of taking one prepared sample disk and breaking it into three pieces after coating. The measurement then consisted of using these three different pieces to measure the conductivity as a function of time held at different temperatures. The temperatures measured were 23°C, 116°C, and 184°C. The target temperatures were reached by heating the sample as quickly as possible

and wait for the sample temperature to come into equilibrium. This would typically take approximately 45 to 60 minutes as opposed to a normal conductivity run were the effective heating rate was estimated to be about 0.3°C per minute.

At room temperature the A.C. conductivity was measured by repeating frequency scans every 9 minutes. Over the course of one hour no significant change was seen in the data. Figure... shows the Cole-Cole plot. The impedance can be measured to increase approximately 5 ohms over a one hour span. However, given a net impedance on the order of 775 Ohms for the sample, this is less than 1% change from the initial reading.

At 116°C it was found that the d.c. intercept shifted 8.5 Ohms to yield a 21% change from the initial reading over a period of 19 hours. The Cole-Cole plot shows that as a function of time the slope of the intercept decreases slightly. At 184°C the d.c. intercept shifted approximately 200 Ohms over the course of 19 hours. This results in a change of 400% from the initial measurement.

The next step performed was done by measuring the conductivity of the third final segment in a normal procedure. However, one exception was made by introducing a Drierite filter of which all of the helium gas must pass through before reaching the liquid nitrogen dewar and the sample.

A.3 Results

Figure shows the results of the normal run. As it can be seen, the d.c. conductivity data falls well above the first data points collected. At the highest

temperature, the sample was held at 203 °C for a period of six hours. During this time the real impedance of this sample increased from 13.6 Ohms to 15.0 Ohms. The sample was then immediately cooled to –34 °C to start a second temperature scan. With a very slight offset the first run and second run are practically identical.

A.4 Discussion

The repeatability between the two runs is very significant. This section will walk through why this measurement shows that the nature of this non-Arrhenius behavior is due to a bulk property of the sample and not due to oxidation, electrode reaction, or electrode diffusion.

The temperature hold at 203 °C for six hours showed that there was approximately a one ohm change in the real impedance of the sample. A second temperature hold for 12 hours after the second run showed that there was approximately a two ohm change. Assuming that the changes during the time dependent, temperature independent measurement are due to either oxidation or some sort of electrode reaction, it would be expected in the worst case scenario that the sample would not deteriorate to a larger extent in a temperature scan than seen over the course of time held at a high temperature. The point is that the non-Arrhenius behavior seen deviates to a much larger extent then the amount of change that would be due to oxidation or electrode reaction. To further illustrate this point it would be expected that the conductivity in the second temperature scan

would fail to recover to the last point measured at the end of the first temperature hold.

A.5 Conclusions

This section illustrates the importance of removing water vapor from the helium flow system. The presence of water vapor affects the conductivity dramatically resulting in orders of magnitude change in the conductivity. Using Drierite in line with the helium flow seems to work adequately for the removal of water. This allows for repeatability from one conductivity run to the next.

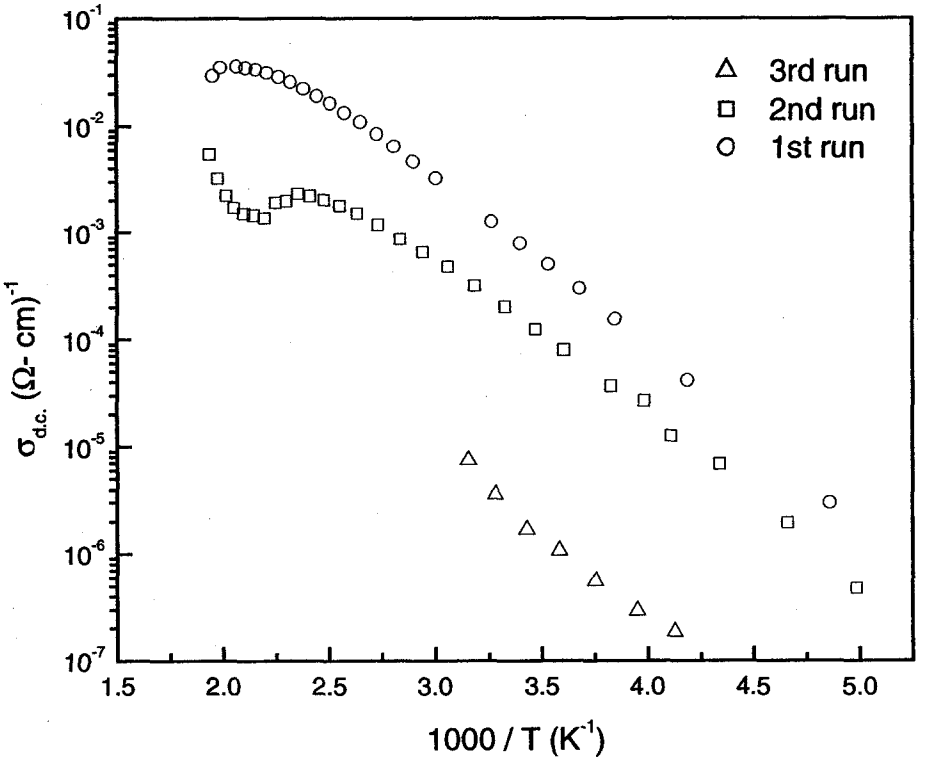

Figure A.1 Arrhenius plot showing repeatability trials without Drierite in the helium flow for the z=0.2; x=0.55 sample.

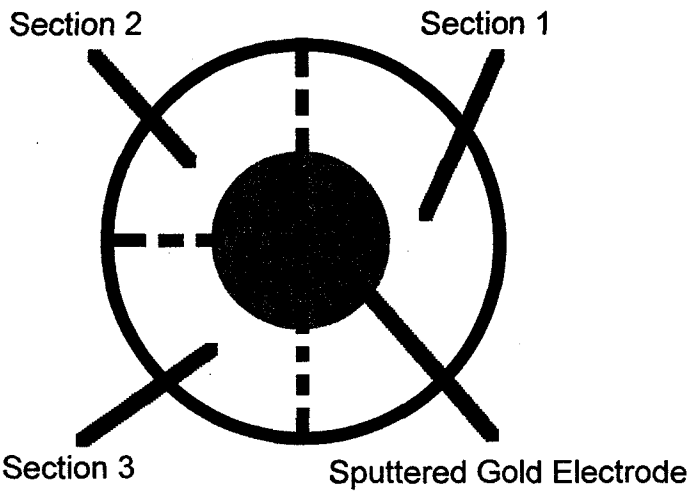

Figure A.2 Figure of bulk conductivity sample prepared. The sample was sputtered coated with gold electrodes and broken into three parts as shown.

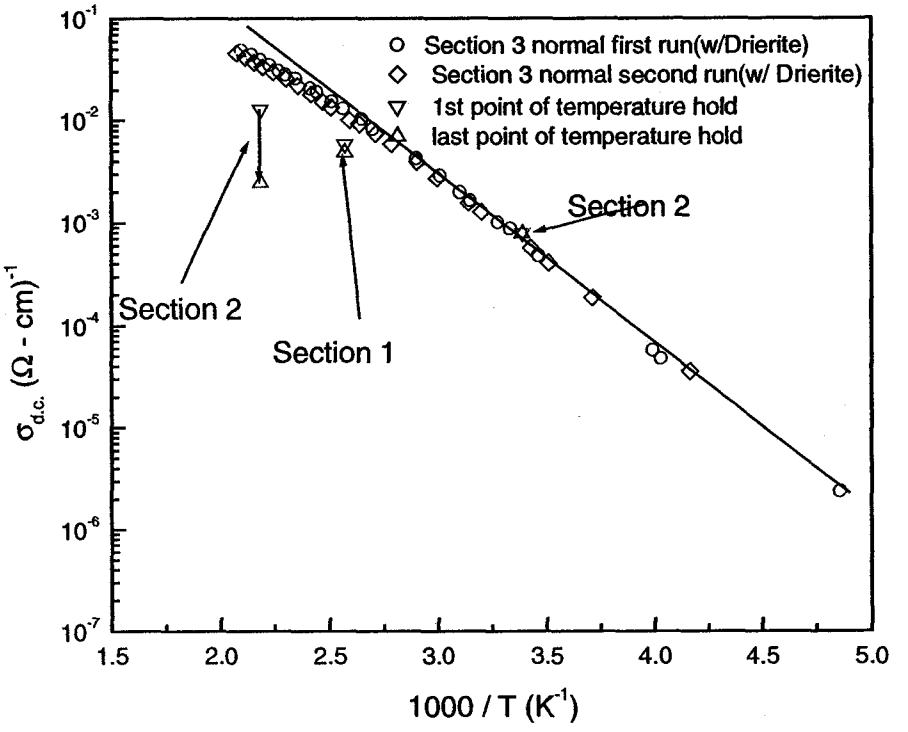

Figure A.3 Arrhenius plot showing the repeatability of non-Arrhenius curves with Drierite filter in line of helium flow. Three data points, for sections 1 and 2, are shown as a time dependent measurements held at different temperatures with no Drierite filter in line with the helium flow.

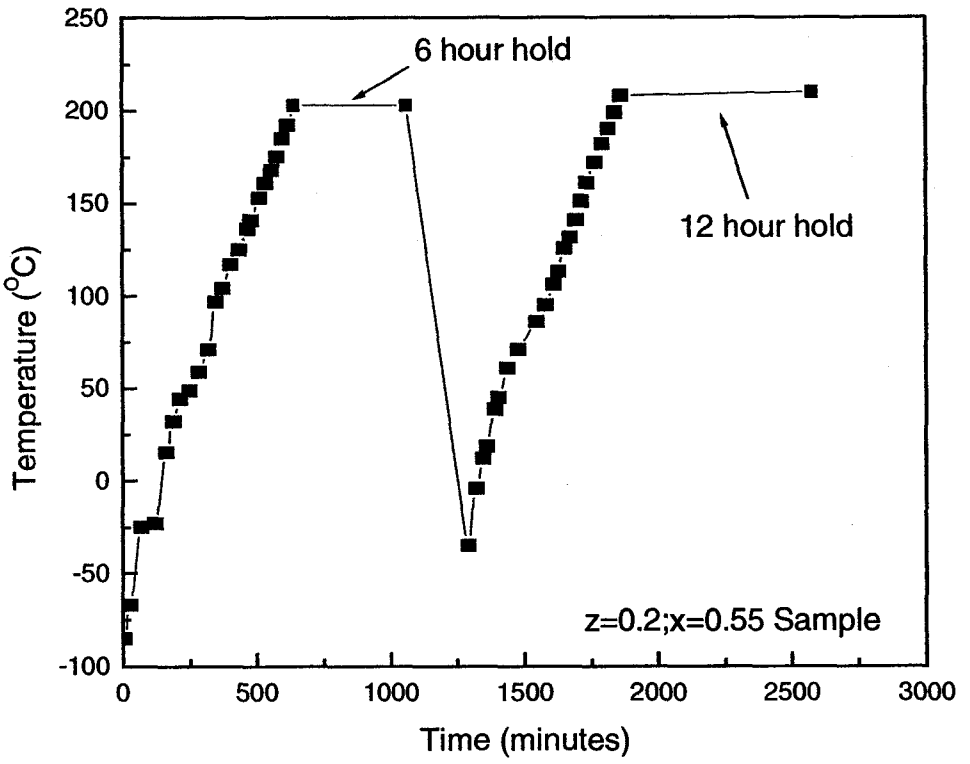

Figure A.4 Approximate temperature profile for the two repeated temperature scans with lengthy temperature holds at the end of each run.

APPENDIX B DAE MODEL PARAMETERS

This section will analyze the effects of middle activation energy and distribution width has on the NSLR and D.C. conductivity curves. The essence of the Distribution of Activation Energies model is using a Gaussian distribution to describe the number of sites at each energy barrier height. In this chapter a thorough analysis will be given on how the middle activation energy(Em), the width of distribution(Eb), and their relationship to the percolation fraction(P) will affect the NSLR and conductivity curves. The following three equations will be the main focus of the discussion in this paper.

$$Z_{NMR}(\Delta E_a) = \frac{1}{\sqrt{2\pi E_b}} \exp\left[-\frac{(\Delta E_m - \Delta E_a)^2}{2E_b}\right] \qquad \text{(B-1)}$$

$$R_1(\omega_L, T) = C\int_0^{\infty}\left[\frac{\tau_a}{1+\omega_L^2\tau_a^2} + 4\frac{\tau_a}{1+4\omega_L^2\tau_a^2}\right]Z_{NMR}\,dE_a \qquad \text{(B-2)}$$

$$\sigma_0(T) = \frac{NPe^{\,2}d^2}{6k_bT\tau_{av}(Z_{NMR})} \qquad \text{(B-3)}$$

Before deeply investigating whether or not the DAE accounts for the Non-Arrhenius behavior in the D.C. conductivity, it will be very beneficial to cover how the ΔE_m, E_b, and P affect the three equations above.

For the case of Equation (B-1), by definition of a Gaussian distribution, Em is the average activation energy and also where the highest population of a specific energy barrier height occurs. ΔE_b is the standard deviation of the distribution curve; which in this case means that it is the full width at half max (FWHM). The percolation fraction, P, has nothing to do with this equation directly. It is mainly a reference point telling where to stop the summation over the distribution for calculation of the conductivity in Equation (B-3).

Referring to Figure B.2, it can easily be seen that as the middle activation energy, ΔE_m, is increased, the NSLR curve maximum shifts to higher temperatures. Also the slope of the curve on the high temperature side becomes steeper. It has been shown that the slope of the curve on the high temperature side is equal to the measured activation energy in the conductivity experiments, which is ΔE_m. It also appears that the height of the maximum is increasing when ΔE_b is held constant while ΔE_m is increased. Actually, the height of this peak is dependent upon two factors, the coupling constant, and the ratio of ΔE_b to ΔE_m. Figure B.8 shows the situation where ΔE_m is increased, and ΔE_b is changed accordingly so that $\Delta E_b/\Delta E_m$ equals twenty percent. It is now seen that the peak maximum continues to shift to higher temperatures, but the peak height remains constant.

In the conductivity plot, it is seen that the slope of the curves is also affected. As the middle activation energy is decreased, the curve becomes steeper and is lower over the whole temperature range. This is to be expected, as the system with the lower activation energy will be thermally excited more easily. Notice how all the

curves seem to extrapolate to the same point at very high temperatures. In theory, if all the systems had the same number of ions total available for conduction regardless of the activation energy. When temperature is equal to infinity, the probability for conduction for every ion would be 100%. This means then that the conductivity for all the systems at an infinite temperature would have the same conductivity.

As the middle activation energy is held constant and the width of the distribution is increased, it is seen that the maximum in the NSLR curve appears to slightly shift to the higher temperature side. This is a result from the greater effect the width of the distribution has on the frequency dependent side as opposed to the independent frequency side. The curve is flattened on the top and the low temperature side becomes increasingly asymmetric.

The conductivity plot also shows an increase in conductivity with increased distribution width. Similar to decreasing the middle activation energy, increasing the width provides more sites at lower activation energies. Thus, this means that the ions in the systems with wider distributions are more quickly thermally activated.

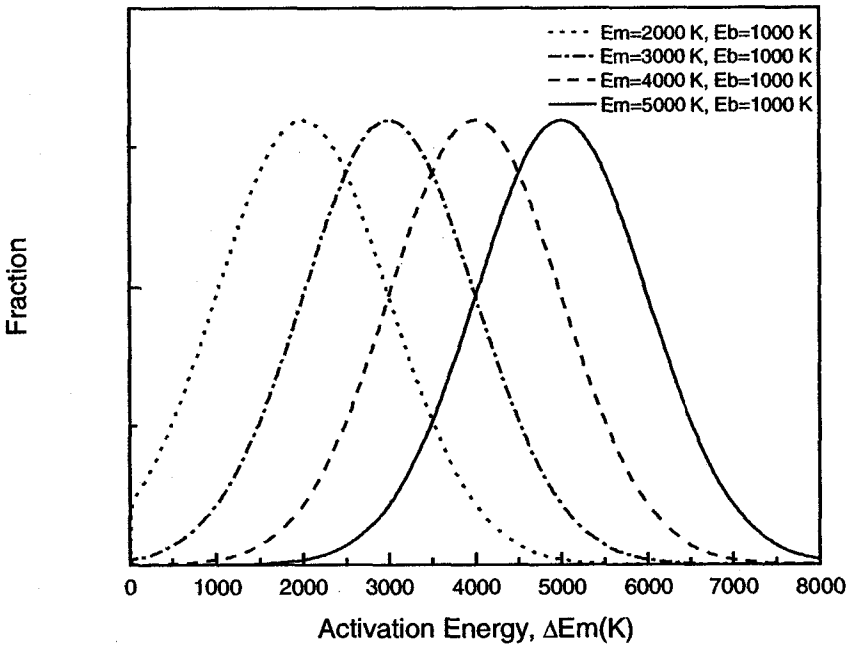

Figure B.1 DAE with varying ΔE_m

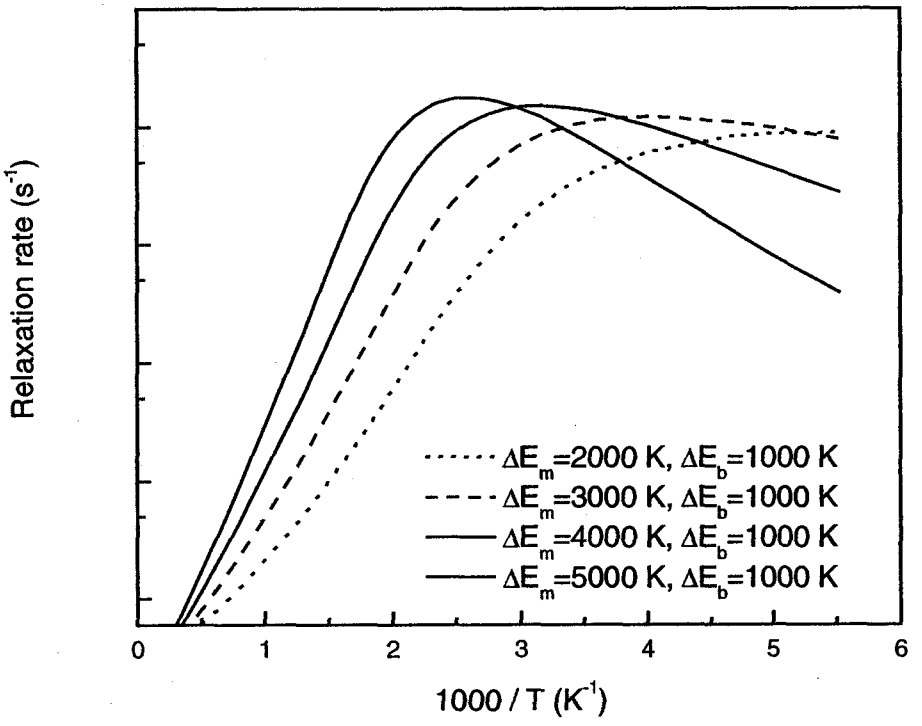

Figure B.2 NSLR cuvers with varying ΔE_m

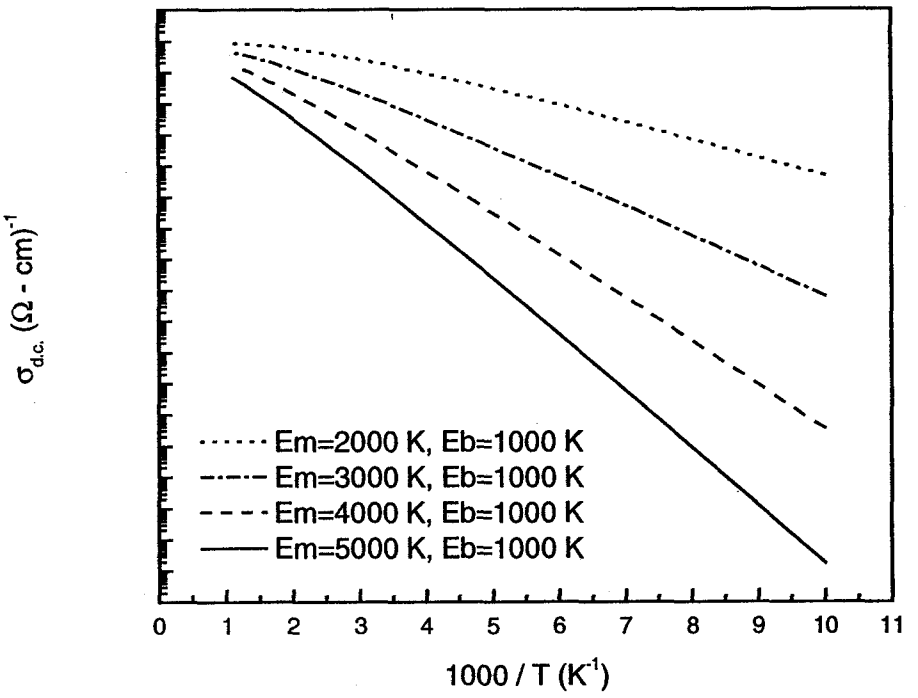

Figure B.3 D.C. conductivity plot with varying ΔE_m.

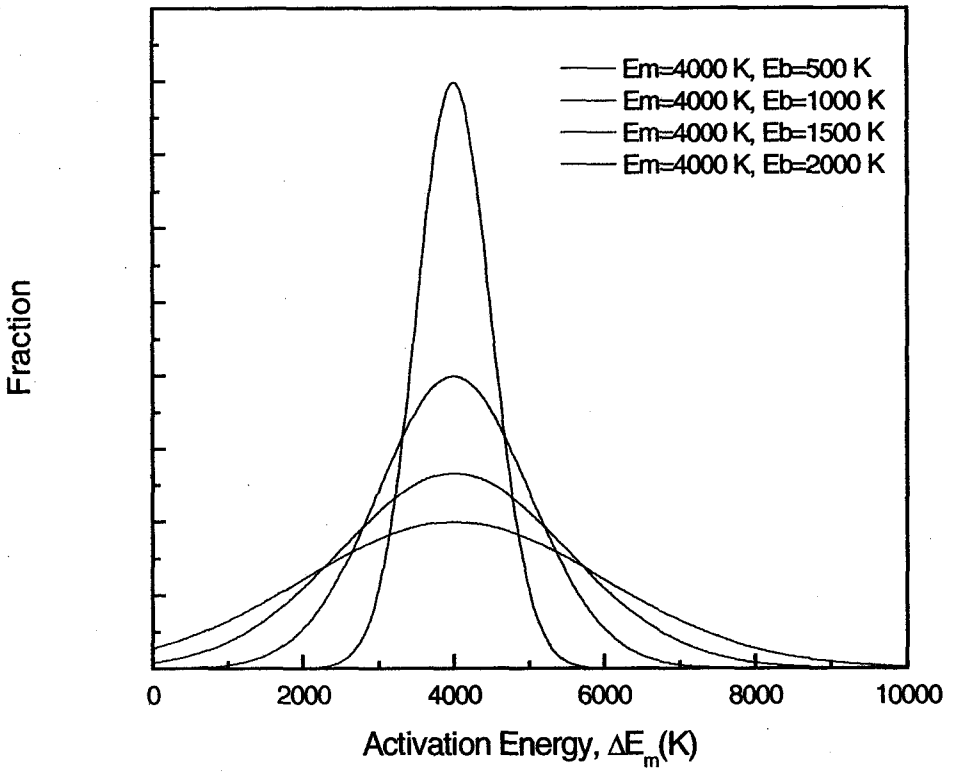

Figure B.4 DAE with varying width, ΔE_b.

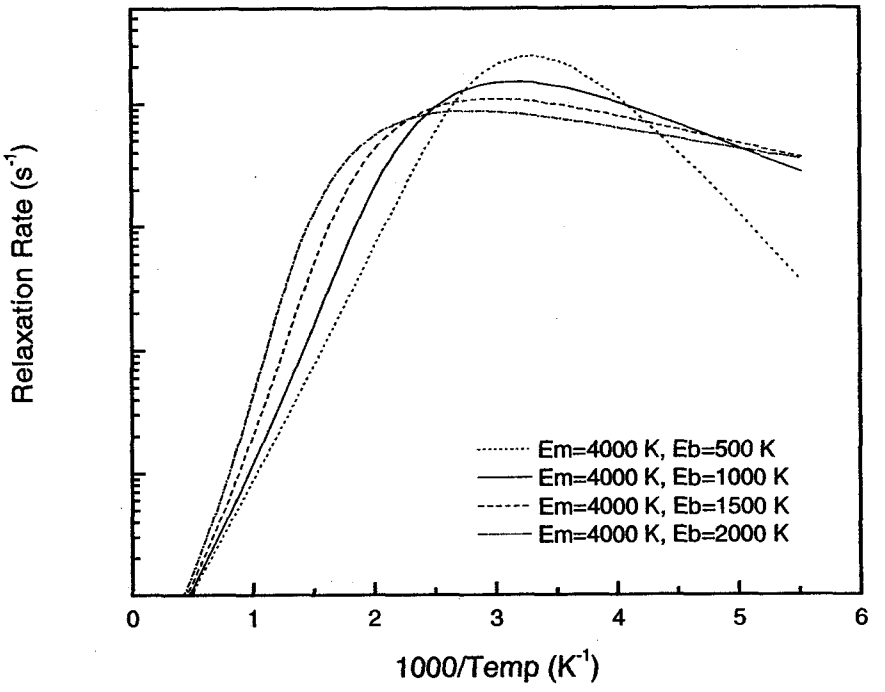

Figure B.5 NSLR curves with varying width, ΔE_b.

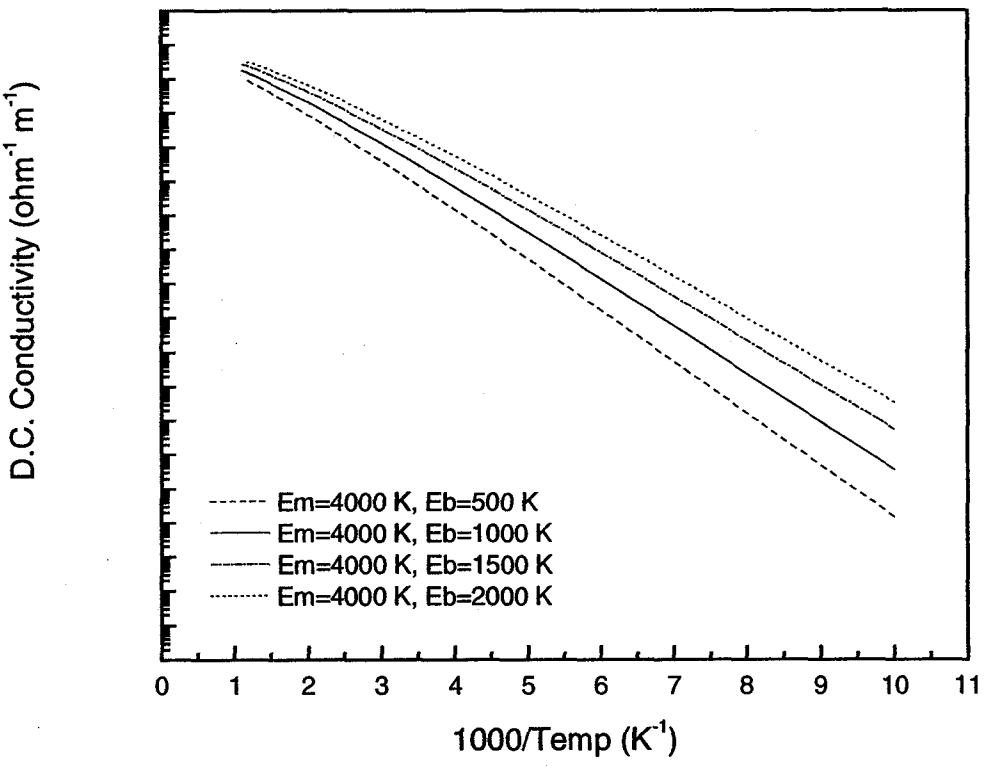

Figure B.6 D.C. conductivity with varying width, ΔE_b.

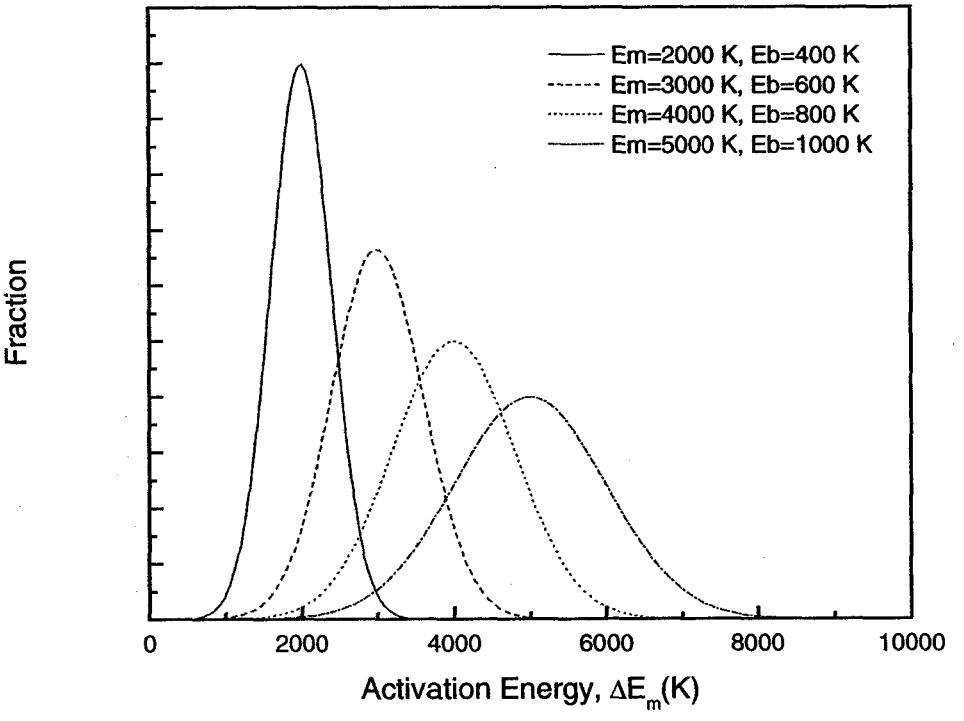

Figure B.7 DAE with $\Delta E_b/\Delta E_m = 0.20$

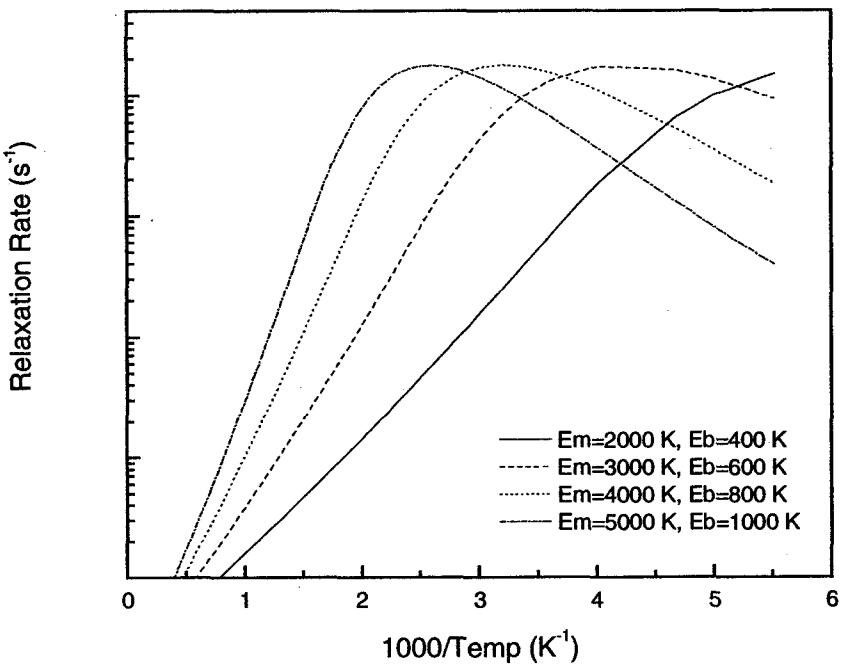

Figure B.8 NSLR curves with $\Delta E_b/\Delta E_m = 0.20$

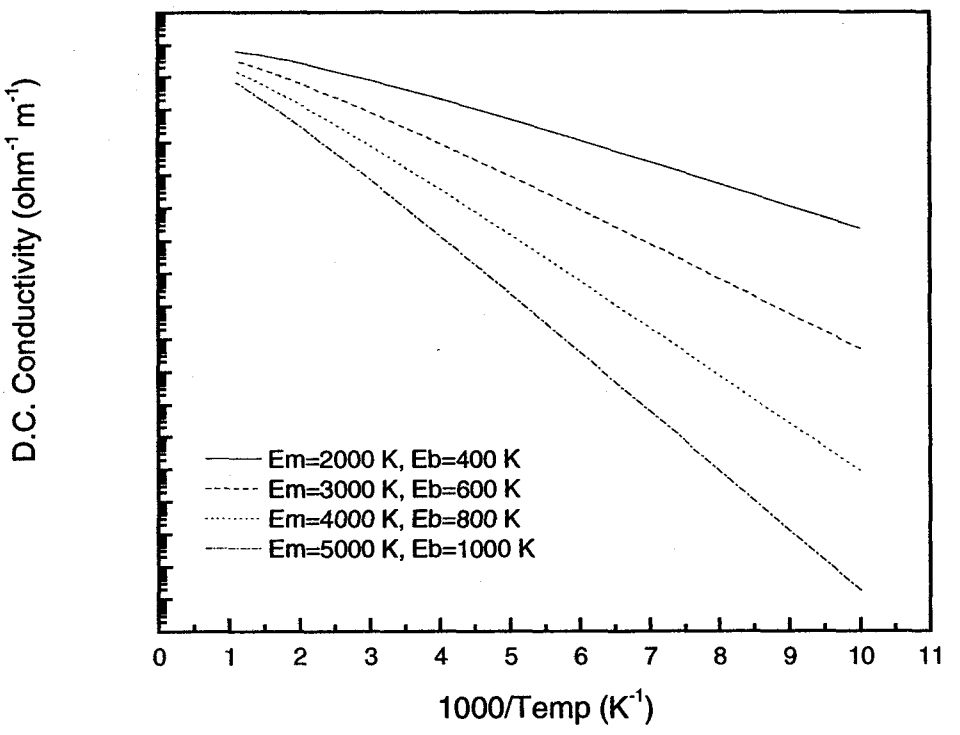

Figure B.9 D.C. conductivity with $\Delta E_b/\Delta E_m = 0.20$

ACKNOWLEDGMENTS

My sincerest thanks go to Dr. Steve W. Martin and Dr. Ferdinando Borsa for their support and encouragement. I have learned a great deal under their supervision and guidance. I would also like to thank Dr. David Martin, with whom I have enjoyed greatly discussing the intricacies of the science that takes place in these glasses.

Special thanks also go out to my fellow friends and group members for their help and support, especially Melissa Grimsley, Annamalai Karthikeyen, Chad Martindale, Qiang Mei, Steve Poling, Jason Saienga, Jeremy Schrooten, Jake Sutherland, and Brad Tischendorf. I appreciate the discussions that we have had through the years, and I will always remember the good times we also shared. Thank you to Andrea for her unconditional love, support, and sacrifices so that I can follow my dreams. Also, thanks goes to my family for their endless support and showing me that one can achieve great things with great effort.

This work was performed at Ames Laboratory under Contract No. W-7405 Eng-82 with the U.S. Department of Energy. The United States government has assigned the DOE Report number IS-T 1926 to this thesis. This work was also performed under the National Science Foundation, grant 9972466 . Special thanks also goes to Iowa State University for its resources and funding.